UNIVERSIDAD POLITÉCNICA DE MADRID
Escuela Técnica Superior de Ingeniería Aeronáutica y del Espacio



On the effect of the processing conditions in the manufacturing of NiTi-based shape memory alloys: microstructural evolution and functional properties

D O C T O R A L T H E S I S

Submitted for the degree of Doctor by:

Conrado Luis Garrido Fernández de Vera
Master of Science in Aeronautical Engineering

Madrid, 2025





UNIVERSIDAD POLITÉCNICA DE MADRID
Escuela Técnica Superior de Ingeniería Aeronáutica
y del Espacio

Doctoral Degree in Aerospace Engineering

On the effect of the processing conditions in the manufacturing of NiTi-based shape memory alloys: microstructural evolution and functional properties

D O C T O R A L T H E S I S

Submitted for the degree of Doctor by:

Conrado Luis Garrido Fernández de Vera
Master of Science in Aeronautical Engineering

Under the supervision of:
Dr. Daniel Barba Cancho

Madrid, 2025

Title: On the effect of the processing conditions in the manufacturing of NiTi-based shape memory alloys: microstructural evolution and functional properties

Author: Conrado Luis Garrido Fernández de Vera

Doctoral Programme: Aerospace Engineering

Thesis Supervision:

Dr. Daniel Barba Cancho, Lecturer, Department of Materials and Aerospace Production, ETSIAE UPM (Supervisor)

External Reviewers:

- Johan Moverare, Professor, Department of Management and Engineering, Linköping University (Sweden).
- Maria Teresa Pérez Prado, Research Professor Head of Sustainable Metallurgy, IMDEA Materials Institute (Spain)

Thesis Defense Committee:

Thesis Defense Date:

The research contained in this thesis has been supported by the following projects:

Comunidad de Madrid

This research Project has been funded by the Comunidad de Madrid through the call Research Grants for Young Investigators from Universidad Politécnica de Madrid. Research program V-PRICIT. Project "SMART-ALLOYS" (Ref. APOYO-JOVENES-21-T9S0YC-102-O4X5XS).

Acción financiada por la Comunidad de Madrid en el marco del Convenio Plurianual con la Universidad Politécnica de Madrid en la línea de actuación estímulo a la investigación de jóvenes doctores. Programa de investigación V-PRICIT. Proyecto "SMART-ALLOYS" (Ref. APOYO-JOVENES-21-T9S0YC-102-O4X5XS).



Grant EQC2019-006491-P funded by MICIU/AEI/10.13039/501100011033 and by ERDF A way of making Europe.

For everybody who was close to me during this journey, especially those who are not between us now.

Acknowledgements

First, I express my deepest gratitude to Prof. Barba, who has supported me throughout this entire process. His guidance and mentorship have not only shaped me into a better professional but also a better person. Without his invaluable advice, this work would not have been possible.

I sincerely thank my teammates over the years for sharing both challenges and triumphs with me. I have learned a lot from you. Special mention goes to Massimiliano, Andrea, Sergio, and Toby. I also appreciate everyone in the laboratory for being part of this journey. In particular, I want to express my gratitude to Arturo for always being available to assist me with all aspects of the experimental work.

I express my heartfelt gratitude to my parents for their important support in each stage of my educational journey. Your encouragement has consistently motivated me to improve my professional abilities.

And, of course, a very special mention goes to the person who stands by me every day, sharing in my highs and lows. Thank you, Lucia, for being one of the pillars of my life, for your endless support and for taking care of both Tarzan and me - and soon Emma as well.

Abstract

Shape memory alloys (SMAs) are a unique class of materials known for their ability to recover their original shape after deformation through thermal or mechanical stimuli. This interesting feature has made SMAs an important material for different applications, including aerospace components, biomedical devices, and other smart structures. Traditionally, SMAs have been produced through conventional methods, which require carefully controlled compositions to achieve the desired phase transformation and actuation behavior. However, recent advancements in additive manufacturing (AM), specifically in laser powder bed fusion (LPBF), have introduced new possibilities for tailoring the microstructure and, therefore, the phase transformation and the actuation properties of SMAs. The problem is that there is still not a complete systematic study exploring this path.

In this work, the impact of the LPBF process parameters (laser power, scanning speed, and hatch spacing) on the transformation and functional behavior of the equiatomic NiTi alloy is examined systematically. The interconnection between processing, and thermomechanical behavior is made through microstructural and material analysis. The findings demonstrate that important material properties such as porosity, nickel evaporation on Ti_2Ni precipitation are directly influenced by the volumetric energy density (VED). The thermomechanical and phase transformation properties of the material are significantly influenced by the Ti_2Ni precipitate population, which rises with higher VED levels. As higher is the population of Ti_2Ni precipitates lower are the actuation features. Low porosity levels are attained in all LPBF-manufactured samples, despite differences in processing conditions, demonstrating the feasibility of using this technique to produce high-quality samples.

Once the effect of processing parameters is established on homogeneous bulk material, the study is taken to the next level: graded bulk material. By selecting different processing parameters in various local regions of the material, this work further investigates the possibility of employing spatially heterogeneous LPBF conditions to design SMA heterogeneous metamaterials with digitally tailored thermomechanical properties in NiTi SMAs. Localized changes in the phase transformation behavior and the actuation response are made possible by selecting the appropriate local process parameters. The study shows how LPBF may be used to produce intricate three-dimensional patterns, which results in different actuation performances. Both the process parameters selected and the pattern geometry are shown to play an important role in the final thermomechanical properties. The pattern geometry produce an important implication in the phase transformation and actuation features reaching different behaviors

between patterned geometries using the same process parameters due to the interaction of the interfaces.

Finally, to further enhance the actuation performance of LPBF-processed SMAs, this research integrates geometric cellular designs with spatially controlled processing conditions. Specifically, body-centered cubic (BCC) lattice structures are fabricated using an ad-hoc LPBF processing strategy that embedded carefully designed processing parameter variations. The goal is to achieve a superelastic response in different regions of the lattice controlled by the LPBF conditions. The fabricated SMA lattices are subjected to cyclic loading under compression, and their superelastic properties are analyzed. The results reveal significant differences in recoverable strain depending on the programmed processing patterns, with values ranging from 6% to 10%. This level of actuation tunability is unprecedented in the field of SMA research and demonstrates the potential of LPBF to design a new generation of SMA components with tailorable thermomechanical responses.

The findings of this study have significant implications for the future of SMA-based actuators and smart materials, demonstrating the ability to program their actuation behavior through both geometrical design and spatially controlled processing. This opens new possibilities for developing multifunctional components with tailored responses, establishing a strong foundation for a new generation of SMA-based metamaterials, where material properties can be digitally designed and locally controlled to meet specific application requirements. Such advancements could lead to breakthroughs in aerospace structures with adaptive morphing capabilities, biomedical implants with regionally optimized stiffness and actuation properties, and robotics components with enhanced compliance and energy efficiency. Significant advancement in the design of intelligent materials has been made feasible by the ability to precisely control LPBF, allowing the engineering of NiTi components with unprecedented levels of microstructural and functional complexity.

Resumen

Las aleaciones con memoria de forma (SMAs, por sus siglas en inglés) son una clase única de materiales conocidos por su capacidad de recuperar su forma original tras la deformación mediante estímulos térmicos o mecánicos. Esta interesante característica ha convertido a las SMAs en materiales clave para diversas aplicaciones, incluyendo componentes aeroespaciales, dispositivos biomédicos y otras estructuras inteligentes. Tradicionalmente, las SMAs se han producido mediante métodos convencionales, los cuales requieren composiciones cuidadosamente controladas para lograr la transformación de fase y el comportamiento de actuación deseados. Sin embargo, los recientes avances en la manufactura aditiva (AM), específicamente en la fusión en lecho de polvo por láser (LPBF), han abierto nuevas posibilidades para ajustar la microestructura y, por ende, las propiedades de transformación de fase y actuación de las SMAs. El problema es que aún no existe un estudio sistemático completo que explore este camino.

En este trabajo, se examina de manera sistemática el impacto de los parámetros del proceso LPBF (potencia del láser, velocidad de escaneo y espaciamiento entre pasadas) sobre la transformación y el comportamiento funcional de la aleación equiatómica de NiTi. La interconexión entre el procesamiento y el comportamiento termomecánico se establece mediante análisis microestructural y de materiales. Los hallazgos demuestran que propiedades clave del material, como la porosidad, la evaporación del níquel y la precipitación de Ti2Ni, están directamente influenciadas por la densidad de energía volumétrica (VED). Las propiedades termomecánicas y de transformación de fase del material se ven significativamente afectadas por la población de precipitados de Ti2Ni, la cual aumenta con niveles más altos de VED. A mayor cantidad de precipitados de Ti_2Ni, menores son las características de actuación. Se alcanzan niveles bajos de porosidad en todas las muestras fabricadas con LPBF, a pesar de las diferencias en las condiciones de procesamiento, lo que demuestra la viabilidad de esta técnica para producir muestras de alta calidad.

Una vez establecido el efecto de los parámetros de procesamiento en un material homogéneo a granel, el estudio avanza al siguiente nivel: material a granel con gradientes. Mediante la selección de diferentes parámetros de procesamiento en diversas regiones locales del material, este trabajo investiga la posibilidad de emplear condiciones heterogéneas de LPBF para diseñar metamateriales heterogéneos de SMA con propiedades termomecánicas ajustadas digitalmente en aleaciones NiTi. La selección adecuada de los parámetros de proceso locales permite realizar cambios localizados en el comportamiento de transformación de fase y en la

respuesta de actuación. El estudio demuestra cómo el LPBF puede utilizarse para producir patrones tridimensionales complejos, lo que da lugar a diferentes niveles de actuación. Se muestra que tanto los parámetros de procesamiento seleccionados como la geometría del patrón juegan un papel crucial en las propiedades termomecánicas finales. La geometría del patrón tiene una implicación importante en la transformación de fase y en las características de actuación, alcanzando comportamientos distintos entre patrones geométricos, incluso utilizando los mismos parámetros de procesamiento, debido a la interacción de las interfaces.

Finalmente, para mejorar aún más el rendimiento de actuación de las SMAs procesadas mediante LPBF, esta investigación integra diseños celulares geométricos con condiciones de procesamiento espacialmente controladas. En particular, se fabrican estructuras de celosía de tipo cúbico centrado en el cuerpo (BCC) utilizando una estrategia de procesamiento LPBF ad-hoc que incorpora variaciones cuidadosamente diseñadas en los parámetros de procesamiento. El objetivo es lograr una respuesta superelástica en diferentes regiones de la celosía controlada por las condiciones LPBF. Las estructuras de SMA fabricadas se someten a cargas cíclicas bajo compresión, y se analizan sus propiedades superelásticas. Los resultados revelan diferencias significativas en la deformación recuperable dependiendo de los patrones de procesamiento programados, con valores que varían entre un 6 % y un 10 %. Este nivel de ajuste de actuación es sin precedentes en la investigación de SMAs y demuestra el potencial del LPBF para diseñar una nueva generación de componentes SMA con respuestas termomecánicas ajustables.

Los hallazgos de este estudio tienen importantes implicaciones para el futuro de los actuadores basados en SMAs y los materiales inteligentes, demostrando la capacidad de programar su comportamiento de actuación tanto a través del diseño geométrico como del procesamiento espacialmente controlado. Esto abre nuevas posibilidades para el desarrollo de componentes multifuncionales con respuestas ajustadas, estableciendo una base sólida para una nueva generación de metamateriales basados en SMAs, donde las propiedades del material pueden diseñarse digitalmente y controlarse localmente para satisfacer requisitos específicos de aplicación. Estos avances podrían conducir a innovaciones en estructuras aeroespaciales con capacidades de morfología adaptativa, implantes biomédicos con rigidez y propiedades de actuación optimizadas regionalmente, y componentes robóticos con mayor cumplimiento y eficiencia energética. La capacidad de controlar con precisión el LPBF ha permitido un avance significativo en el diseño de materiales inteligentes, posibilitando la ingeniería de componentes de NiTi con niveles sin precedentes de complejidad microestructural y funcional.

Table of Contents

Acknowledgement v
Abstract vi
Resumen viii
List of Figures xiv
List of Tables xxiii
Abbreviations and acronyms xxvii
Publications xxviii

1 Introduction **1**
1.1 Introduction 1
1.2 Historical background and overview 2
1.3 Statement of the problem 4
1.4 Objectives and thesis structure 5

2 State of the art **9**
2.1 Types of SMAs 9
2.1.1 NiTi-based alloys 9
2.1.2 NiTiCu alloys 10
2.1.3 NiTiZr alloys 10
2.1.4 NiTiPt alloys 11
2.1.5 NiTiPd alloys 11
2.1.6 NiTiHf alloys 11
2.1.7 Phase transformation and actuation properties of the differnet types of SMAs 12
2.2 Physical metallurgy of NiTi SMAs 12
2.2.1 Phases and crystal structures 12
2.2.2 Phase transformation phenomenology 13

2.2.3 Binary phase diagram and precipitates . . . 16
2.3 Thermomechanical properties of SMAs . . . 19
2.3.1 Shape memory effect (SME) . . . 19
2.3.2 Pseudoelasticity (PE) . . . 19
2.3.3 Cyclic behavior . . . 21
2.4 Additive manufacturing of NiTi alloys . . . 22
2.4.1 Introduction to additive manufacturing . . . 22
2.4.2 Additive manufacturing of NiTi SMAs . . . 23
2.4.3 Fundamentals of LPBF . . . 23
2.4.4 LPBF of NiTi SMAs . . . 26
Effect of the process parameters . . . 26
Graded NiTi SMA metamaterials . . . 27
NiTi SMA cellular structures . . . 28
2.5 Applications of NiTi alloys . . . 29
2.5.1 Aerospace applications . . . 29
2.5.2 Biomedical applications . . . 31
2.5.3 Other applications . . . 32

3 Process optimization on additively manufactured NiTi SMA 33
3.1 Introduction . . . 33
3.2 Methodology . . . 34
3.2.1 Design of experiments . . . 34
3.2.2 Material characterization . . . 38
Porosity analysis . . . 38
Phase transformation temperatures characterization . . . 38
Composition analysis . . . 39
3.3 Results . . . 39
3.3.1 Porosity analysis . . . 39
3.3.2 Phase transformation analysis . . . 42
3.4 Discussion . . . 44
3.4.1 Effect of the process parameters on the manufactured structure . . . 44
3.4.2 Effect on the process parameters on the phase transformation . . . 48
3.5 Conclusions . . . 50

4 Thermomechanical and phase transformation behavior of additively manufactured NiTi SMA 53
4.1 Introduction . . . 53

4.2 Methodology . . . 54
4.2.1 Design of experiments . . . 54
4.2.2 Material characterization . . . 55
Microstructure analysis and precipitates' quantification . . . 55
4.2.3 Mechanical testing . . . 55
4.3 Results . . . 57
4.3.1 Microstructure . . . 57
4.3.2 Thermomechanical performance . . . 59
4.4 Discussion . . . 64
4.4.1 Influence of processing parameters on the microstructure . . . 64
4.4.2 Influence of processing parameters on the transformation temperatures TTs . . . 69
4.4.3 Influence of processing parameters on the thermomechanical properties 69
4.4.4 Implications of the observed results in the LPBF of SMAs . . . 76
4.5 Conclusions . . . 78

5 Design of graded bulk NiTi SMA metamaterials by local change of processing conditions 81
5.1 Introduction . . . 81
5.2 Methodology . . . 82
5.2.1 Design of experiments . . . 82
5.2.2 Material characterization . . . 83
5.2.3 Thermomechanical testing . . . 84
5.2.4 Computational approaches . . . 84
LPBF thermal modeling . . . 84
Thermal finite element simulation . . . 86
5.3 Results . . . 89
5.4 Results and discussion . . . 89
5.4.1 Microstructural analysis . . . 89
Grain structure and porosity . . . 89
Sub-grain structure: precipitate distribution . . . 91
5.4.2 Homogenized macro-thermomechanical behavior . . . 92
Transformation temperatures . . . 93
Recoverable and plastic strain . . . 96
Hysteresis behavior . . . 99
5.4.3 Local micro-thermomechanical behavior . . . 100

Interlayer interfaces (Pattern 1) . . . 100
On layer interfaces (Pattern 2 and Pattern 3) . . . 105
5.5 Conclusions . . . 111

6 Additive manufacturing of graded NiTi SMA cellular structures 113
6.1 Introduction . . . 113
6.2 Methodology . . . 116
6.2.1 Design of experiments . . . 116
6.2.2 Material characterization . . . 117
Measurement of the solid fraction . . . 117
Analysis of the strut diameter distribution and cell pore size . . . 117
Microstructural characterization . . . 118
6.2.3 Mechanical testing . . . 118
6.2.4 Computational approaches . . . 118
6.3 Results and Discussion . . . 119
6.3.1 Manufacturability analysis . . . 120
Solid fraction . . . 120
Surface analysis . . . 120
Strut diameter and cell pore size . . . 121
6.3.2 Microstructural analysis . . . 123
6.3.3 Thermomechanical behaviour . . . 124
6.3.4 Phase transformation . . . 127
6.3.5 Recoverable strain . . . 130
6.3.6 Plastic strain . . . 136
6.3.7 Design space for SMA lattice-based smart materials . . . 137
6.4 Conclusions . . . 139

7 General Discussion 143

8 Conlusions and future work 149
8.1 Conclusions . . . 149
8.2 Future Work . . . 150

References 163

List of Figures

1.1 Thesis structure showing the key research carried out. 8

2.1 (a) Austenite start temperature (A_s) and (b) recovery strain of NiTi, NiTiCu, NiTiZr, NiTiPt, NiTiPd and NiTiHf alloys extracted from the literature. See Tables 1 and 2 in the Annex for more details. 13

2.2 Crystallographic phases observed in near equiatomic NiTi: (a) B2 austenite, (b) B19´ martensite and (c) R-phase. 14

2.3 Typical stress-temperature transformation map of NiTi SMAs. 14

2.4 (a) austenite-martensite interfaces during the transformation. (b) Simplified model of the shear mechanism during the transformation. 15

2.5 Typical observed phase transformation paths in NiTi SMAs. A_s, A_f, M_s and M_f TTs are not the same temperatures in loaded and unloaded conditions (see Figure 2.3). 17

2.6 Binary phase diagram of NiTi alloys [110]. 18

2.7 Stress-strain-temperature diagram showing the shape memory effect of SMAs. 20

2.8 (a) Stress-temperature and (b) stress-strain diagrams showing a pseudoelastic path of SMA. 20

2.9 Different training paths: (a) constant stress during thermal cycles, and (b) constant temperature during PE cycles. 21

2.10 (a) Schematic of a LPBF machine. (b) Schematic of the main processing parameters of the LPBF process. 25

3.1 Combinations of process parameters selected in the broad approach to perform the porosity analysis for (a) 70 J/mm^3, (b) 80 J/mm^3 and (c) 90 J/mm^3. More information about the process parameters can be found in the Annex. 36

3.2 Combinations of process parameters selected in the systematic approach to perform the porosity and phase transformation analysis. The anchor point is represented in black. P (in blue) refers to the samples fabricated with different laser powers, V (in green) to the ones manufactured with variations in scanning speed, and H (in red) to the ones with variations in hatch spacing. More information about the process parameters can be found in the Annex. 37

3.3 Geometries of the samples manufactured to perform the porosity and phase transformation analysis. 38

3.4 Example of how TTs variables are extracted from Differential Scanning Calorimetry (DSC). 39

3.5 Porosity maps of the LPBF NiTi cubes for VEDs of (a) 70 J/mm^3, (b) 80 J/mm^3 and (c) 90 J/mm^3 used in the broad approach. 40

3.6 LPBF samples with porosity levels below 0.2 % in the broad approach. . . . 41

3.7 DSC curves of the defect-free LPBF NiTi samples for VEDs of (a) 70 J/mm^3, (b) 80 J/mm^3 and (c) 90 J/mm^3 used in the broad approach. 43

3.8 (a,c,e) Differential Scanning Calorimetry (DSC) results, and (b,d,f) variation of the martensite transformation start temperature (M_s), the martensite transformation finish temperature (M_f), the peak of the martensite transformation (M_p), the austenite start transformation temperature (A_s), the austenite finish transformation temperature (A_f) and the peak of the austenite transformation (A_p), for (a-b) samples P1-P4, (c-d) samples V1-V5 and (e-f) samples H1-H5. More information about the calculated TTs can be found in the Annex. . . . 45

3.9 Porosity levels of the samples used in the broad approach and their LED for samples manufactured using VEDs of (a) 70 J/mm^3, (b) 80 J/mm^3 and (c) 90 J/mm^3. 46

3.10 Porosity levels of the samples manufactured in the systematic approach as function of (a) LED and (b) VED. The anchor point is represented in black. P (in blue) refers to the samples fabricated with different laser powers, V (in green) to the ones manufactured with variations in scanning speed, and H (in red) to the ones with variations in hatch spacing. 47

3.11 Average TTs and their respective error bars obtained from the analysis of the DSC curves in Figure 3.7 showing the martensite transformation start temperature (M_s), the martensite transformation finish temperature (M_f), the peak of the martensite transformation (M_p), the austenite start transformation temperature (A_s), the austenite finish transformation temperature (A_f) and the peak of the austenite transformation (A_p). More information about the calculated TTs can be found in the Annex. 48

3.12 (a) Equilibrium vapor pressures of Ni (red) and Ti (blue) calculated according to the equations presented in [199]. (b) Atomic nickel (Ni) content (%) present in the LPBF manufactured samples as a function of the VED. The anchor point is represented in black. P (in blue) refers to the samples fabricated with different laser powers, V (in green) to the ones manufactured with variations in scanning speed, and H (in red) to the ones with variations in hatch spacing. In general, the Ni content reduces with increased VED due to higher Ni evaporation. . 49

3.13 Austenite (A_p) and martensite (M_p) peak temperatures as a function of the VED. VED is changed through the three LPBF process parameters under study: laser power (blue), scanning speed (green) and hatch spacing (red). The anchor point is highlighted in black. 50

4.1 Example of how the thermomechanical variables are extracted from: (a) Tensile tests, (b) actuation and training tests. 56

4.2 Force and temperature variations during: (a) actuation test, (b) training and TWSME tests. 57

4.3 SEM images of the LPBF NiTi samples obtained by changing the process parameters: laser power (samples P1-P4), scanning speed (samples V1-V5) and hatch spacing (samples H1-H5). The results for the sample fabricated with the anchor parameter sets is also represented. Yellow arrows indicate the presence of Ti_2Ni precipitates. 58

4.4 Actuation test: strain-temperature response under constant stresses of 50, 100, 150 and 200 MPa, of the NiTi tensile samples additively manufactured by changing the process parameters: laser power (samples P1 and P4), scanning speed (samples V1 and V5) and hatch spacing (samples H1 and H5). The results for the sample fabricated with the anchor parameter sets are represented in black. 60

4.5 Actuation test: (a,c,e) Recoverable strain (squares) and plastic strain (circles) are shown as a function of the stress level. (b,d,f) The TTs are displayed as a function of the stress level. (a-b) correspond to variations in laser power (samples P1 and P4), (c-d) depict changes in scanning speed (samples V1 and V5), and (e-f) represent the changes in hatch spacing (samples H1 and H5). In all diagrams, the anchor point is highlighted in black. Results are obtained from the analysis of the curves in Figure 4.4. 62

4.6 Training and TWSME tests: (a-b) Five training cycles under a constant stress of 200 MPa and (c) TWSME cycle after the 5 training cycles, of the tensile samples fabricated by changing: laser power (blue), scanning speed (green) and hatch spacing (red). 63

4.7 Training test: recoverable strain and plastic strain plotted along the number of cycles for the training tests for: (a) variations in laser power (samples P1 and P4), (b) changes in scanning speed (samples V1 and V5) and (c) changes in hatch space (samples H1 and H5). In all diagrams the anchor point is highlighted in black. 65

4.8 TWSME test: Recoverable strain extracted from the TWSME tests shown in Figure 4.6c modifying the laser power (blue), scanning speed (green) and hatch spacing (red). The anchor point is highlighted in black. 66

4.9 (a) Percentage of precipitates present in all LPBF fabricated samples; (b) Correlation between the percentage of precipitates and the nickel content in all LPBF fabricated samples. In all diagrams the anchor point is represented in black, while samples manufactured with variations in: laser power (P) are denoted in blue, scanning speed (V) in green, and hatch spacing (H) in red. 67

4.10 Schematic of the physical processes occurring at the melt pool during the LPBF manufacturing of NiTi alloys. At higher VED, higher amounts of nickel evaporate. BD stands for build direction (of the LPBF process). 68

4.11 Results of the transformation temperatures at different stress levels extracted from the actuation test (Figure 4.4): (a) 50 MPa, (b) 100 MPa, (c) 150 MPa and (d) 200 MPa, where the color code correspond to changes in laser power (blue), scanning speed (green) and hatch spacing (red). The anchor point is highlighted in black. Samples corresponding to the lowest VEDs (P1, V5, and H5) are located in the lower TTs region and samples corresponding to the highest VEDs (P4, V1, and H1) are positioned on the higher TTs region. . . 70

4.12 Austenite start temperature (A_s) along the training cycles for the different samples. The color code correspond to changes in laser power (blue), scanning speed (green) and hatch spacing (red). The anchor point is highlighted in black. 71
4.13 Austenite start temperature (A_s) in the different samples along the VED in the training test. The color code correspond to changes in laser power (blue), scanning speed (green) and hatch spacing (red). The anchor point is highlighted in black. 72
4.14 Elastic modulus of austenite (top) and martensite (bottom) phases of all the samples along VED. The color code correspond to changes in laser power (blue), scanning speed (green) and hatch spacing (red). The anchor point is highlighted in black. 73
4.15 Recoverable strain as a function of the VED extracted from the actuation tests shown in Figure 4.4 for each stress level: (a) 50 MPa, (b) 100 MPa, (c) 150 MPa and (d) 200 MPa. Changes in the VED were produced by modifying the laser power (blue), scanning speed (green) or the hatch space (red). The anchor point is highlighted in black. 74
4.16 Recoverable strain as a function of the VED extracted from the TWSME tests shown in Figure 4.6c. Changes in the VED were produced by modifying the laser power (blue), scanning speed (green) or the hatch space (red). The anchor point is highlighted in black. The slopes of the lines ($\frac{\Delta\varepsilon_{Rec}}{\Delta \text{VED}}10^{-5}$) are also depicted. 75
4.17 Recovery rate of all samples along cycles in the training test. The color code correspond to changes in laser power (blue), scanning speed (green) and hatch spacing (red). The anchor point is highlighted in black. 76
4.18 Recoverable strain in the different samples along the VED in the training test. The color code correspond to changes in laser power (blue), scanning speed (green) and hatch spacing (red). The anchor point is highlighted in black. . . 77

5.1 (a) Pattern geometries proposed in this study to the manufacture heterogeneous NiTi samples. (b) Scanning strategy employed during the manufacturing of the patterned geometries. 83
5.2 Temperature dependent material properties of solid and powder NiTi. (a) Density [242], (b) thermal conductivity [243], (c) specific heat [243] and (d) solidus and liquidus temperatures [244], latent heat of fusion [245], emissivity [246], absorption efficiency [247], beam diameter, penetration depth and laser power 87

5.3 (a) Thermal modeling configuration of the SLM process with boundary conditions. (b) Overview of the FE simulated cases studied on this work. 88

5.4 Microstructure of the patterned samples and monoparameter samples manufactured. White dotted line represents the interface between the different processing parameter used. 90

5.5 Microstructures of the different regions in the patterned samples. 91

5.6 Strain-temperature curves of the LPBF NiTi samples with patterns extracted from training (continuous lines) and TWSME (dotted lines) tests. First, second and third rows correspond to samples fabricated using Patterns 1, 2 and 3 respectively. First, second and third columns correspond to the combinations A-B, A-C and A-D of process parameters used to manufacture each pattern respectively. 94

5.7 (a),(c),(e) represent the TTs of each thermomechanical cycle showing the martensite transformation finish temperature (M_f) and the austenite start transformation temperature (A_s). (b),(d),(f) predsent the M_f and A_s temperatures in the TWSME test. (a)-(b), (c)-(d) and (e)-(f) display the results of the LPBF samples manufactured with combinations of parameters A-B, A-C and A-D respectively. Dotted black and gray lines represent the results of the homogeneous samples of each combination of process parameter used to manufacture the patterned samples. The results for monoparameter homogeneous samples of the same alloy are presented for comparison. 95

5.8 (a),(c),(e) show recoverable and plastic strains along the thermomechanical cycles of the training. (b),(d),(f) represent the recovery strain obtained from the TWSME test of each patterned geometry. (a)-(b), (c)-(d) and (e)-(f) display the results of the LPBF samples manufactured with combinations of parameters A-B, A-C and A-D respectively. Dotted black and gray lines represent the results of the homogeneous samples of each combination of process parameter used to manufacture the patterned samples. The results for monoparameter homogeneous samples of the same alloy are presented for comparison. 97

5.9 Area inside the TWSME cycles for each patterned sample. The results of the monoparameter samples have been extracted from the previous work (see Chapter 4) 101

5.10 Schematic of the development of high texture during LPBF process. (a) Schematics of the austenite grain growth process during the LPBF of NiTi. Texture is create on austenite microstructure by the subsequent laser tracks, which re-melt the [010] grains creating a directional thermal gradient and favoring the epitaxial growth. (b) Schematic representation of the microstructure formed at the horizontal interfaces resulting during the AM process in Pattern 1. 102

5.11 Recoverable and plastic strain results of Pattern 1 compared to the monoparameter samples (continuous lines) and the local regions (dotted lines) manufactured using each process parameter in the patterned samples during the training test. 104

5.12 Results of the laser track simulations. Cases L and H are presented as dotted lines indicating the maximum values achieved. 106

5.13 Results of the laser track simulations: temperature of points of the interface (Point A) with a depth of: 0, 15, 30, 45 and 60μm from the surface. 108

5.14 Von Mises stress results of the elasto-plastic simulations for (a) Pattern 1, (b) Pattern 2 and (c) Pattern 3. 110

6.1 Types of cellular materials depending on their internal structure. 114

6.2 Overview of the combined geometrical (A) and processing (B) design framework (A+B) leading to cellular structures with tailored thermomechanical behaviour. 115

6.3 (a) BCC unit cell indicating the specific features selected for this work. (b) Measurements of the lattice structure designed for this work. (c) Lattice structures printed in this study. Blue and green indicate A and B set of process parameter employed respectively. 116

6.4 (a) Detail of the temperature and force evolution during the actuation tests in this study. (b) Exemplary diagram of the variables extracted from the temperature - strain data measured during the actuation tests. 119

6.5 Experimentally mesaured solid fraction results of lattice structures fabricated using processing parameters A, B and graded A-B. Ideally designed solid fractions are also presented as black dotted line for comparison. 120

6.6 SEM micrographs of the different lattice structures. Powder particles and layer corrugations are marked in the magnified micrographs with pink and yellow arrows respectively. 122

6.7 (a) Diameter and (b) pore size distributions of the printed lattice structures. The target design is pointed out as a black dotted line. 123

6.8 Microstructural analysis of the lattice structures of this work. 124

6.9 Actuation behavior under compression at a force of: (a) 250 N, (b) 500 N, (c) 750 N, (d) 1000 N and (e) 1250 N. Blue, green and red represent the lattice structures fabricated with each processing configuration A, B and A-B, respectively. 126

6.10 Average Von Mises stress of each lattice structure experienced in the FEA simulations under a constant load of 250, 500, 750, 1000 and 1250 N. 127

6.11 (a) Martensite start temperature (M_s) for each lattice structure and the average Von Mises stress from FEA for each lattice structure. The results of the tensile samples manufactured using process parameters A and B are also displayed (see Chapter 4); (b) Difference between the maximum and the minimum M_s values obtained for each stress level for lattices and bulk material. 128

6.12 Deformation color map of the lattices A,B and A-B in the thermomechanical cycle subjected to a compressive load of 1250 N. The frames shown correspond to 0, 25, 50, 75 and 100% of the forward transformation. 131

6.13 Von Mises stress and martensite start temperature (M_s) after applied a compressive force of 1250 N in each lattice structure. 132

6.14 Recoverable strain for each lattice structure under the average Von Mises stress of the lattice structure. The results of the bulk material using process parameters A and B are also displayed (see Chapter 4). 133

6.15 Multiplicative effect in transferring microstrains to macrostrains in cellular materials and its effect in the actuation behavior. 134

6.16 Recovery rate of the different lattice structures. The results of the tensile samples manufactured using process parameters A and B are also displayed (see Chapter 4). 136

6.17 Plastic strain for each lattice structure as a function of the average Von Mises stress of the lattice structure. The results of the tensile samples manufactured using process parameters A and B are also displayed (see Chapter 4). 137

6.18 Effectiveness of the latticing and processing modulation in the design of the thermomechanical behavior of SMA cellular structures: (a) Recovery strain and (b) M_s transformation temperature. 138

6.19 Maximum recovery strain-solid fraction diagrams comparing the lattice structures studied with the ones of other works: [294, 149, 29, 295, 296, 297, 25, 298, 299, 300, 148] 140

8.1 Results of the laser track simulations: (a)-(b) display the solid material width and (c)-(d) presents the solid material depth. Cases L and H are presented as dotted lines indicating the maximum values achieved. 162

List of Tables

3.1 Chemical composition of the NiTi powder used in this work. 35

3.2 Average porosity (in percentage) for LPBF NiTi samples from the systematic approach and the values of LED and VED for each set of process parameters according to equations 2.1 and 2.2 respectively. 42

4.1 Elastic modulus of the austenite and martensite phases in each sample. . . . 59

5.1 LPBF processing parameters used in the manufacturing of NiTi samples. . . 83

6.1 LPBF processing parameters used in the manufacturing of NiTi lattice structures samples. VED was calculated as VED = $\mathrm{P}/(\mathrm{v} \cdot \mathrm{h} \cdot \mathrm{t})$ where P is the laser power, v is the scanning speed, h is the hatch spacing and t is the layer thickness. LED was calculated as LED = P/v. 117

1 Composition, austenite start temperature (A_s) and recoverable strain of NiTi alloys from the literature. 154

2 Composition, austenite start temperature (A_s) and recoverable strain of NiTiCu, NiTiHf, NiTiPt, NiTiPd and NiTiZr alloys from the literature. 155

3 Process parameter combinations employed to fabricate samples for porosity analysis, resulting in a total VED of 70 J/mm^3 for the broad approach. . . . 156

4 Process parameter combinations employed to fabricate samples for porosity analysis, resulting in a total VED of 80 J/mm^3 for the broad approach. . . . 157

5 Process parameter combinations employed to fabricate samples for porosity analysis, resulting in a total VED of 90 J/mm^3 for the broad approach. . . . 158

6 LPBF processing parameters used in the manufacturing of NiTi samples for the systematic approach. 159

7 Transformation temperatures calculated from DSC curves in the broad approach. 160

8 TTs obtained from the analysis of the DSC curves in Figure 3.8 showing the martensite transformation start temperature (M_s), the martensite transformation finish temperature (M_f), the peak of the martensite transformation (M_p), the austenite start transformation temperature (A_s), the austenite finish transformation temperature (A_f) and the peak of the austenite transformation (A_p) in the systematic approach. 161

Abbreviations and acronyms

UPM	Universidad Politécnica de Madrid
SMA	Shape memory alloy
AM	Additive manufacturing
LPBF	Laser powder bed fusion
EBM	Electron beam melting
TTs	Transformation temperatures
VED	Volumetric energy density
LED	Linear energy density
PE	Pseudoelasticity
SME	Shape memory effect
TWSME	Two way shape memory effect
HTSMAs	High temperature shape memory alloys
DSC	Differential scanning calorimetry
SEM	Scanning electron microscope
EBSD	Electron backscatter diffraction

Publications

The following publications are associated with the work carried out in this thesis:

- C. Garrido, S. Perosanz, A. Elliot, D. Barba. "On the effect of the processing parameters in microstructure and thermomechanical properties of LPBF NiTi shape memory alloys." Journal of Materials Research and Technology 33 (2024): 2414-2429.
- C. Garrido, A. Elliot, D. Barba. "Shape memory alloy metamaterials designed by LPBF with tailored thermomechanical properties." In the process of submission to Acta Materialia.
- C. Garrido, A. Elliot, D. Barba. "Geometry-microstructure coupled design of shape memory metamaterials with programmable actuation behavior through local modulation of LPBF conditions." In the process of submission to Additive Manufacturing.

Chapter 1

Introduction

1.1 Introduction

Shape memory alloys (SMAs) are a class of metallic materials capable of undergoing recoverable shape changes due to diffusionless reversible martensitic phase transformations. These transformations can be induced by changes in temperature or stress. At high temperatures, SMAs exist in the austenite phase. Cooling below the phase transformation temperature, the austenite phase transitions to the martensite phase. The martensite deforms through a twinning mechanism, which transforms different variants into the one that best accommodates the required deformation in the direction of the applied force [1].

Nickel-titanium (NiTi) SMAs are widely used in different systems across various industrial sectors, such as aerospace [2, 3], automotive [4, 5], biomedical [6, 7] and also in industrial applications [8, 9], due to their excellent corrosion resistance and durability [10]. Their functional properties, such as the shape memory effect (SME), pseudoelasticity (PE) and two-way shape memory effect (TWSME), provide them with exceptional features [11, 12, 13]. However, the machinability of NiTi alloys is limited, which presents difficulties in creating complex structures with tailored functional properties using conventional processing techniques [14]. Consequently, NiTi alloy components have been historically fabricated in basic shapes such as plates and rods, limiting their full potential utilization [15]. Therefore, the development of effective joining techniques is essential for the manufacturing of complex geometries and the fully exploit of the SMAs potential.

The appearance of metal Additive Manufacturing (AM) in recent years set a new path for the processing of SMAs [16]. AM increases the design freedom, and therefore the ability to

create complex geometries which are not possible to achieve with conventional methods [17]. These techniques, such as Laser Powder Bed Fusion (LPBF) and Electron Beam Melting (EBM), extend the design space in SMA materials [18, 19]. In addition, as reported in the literature, the thermomechanical properties of the LPBF NiTi samples can be modified depending on the processing parameters used during the manufacturing process. For example, transformation temperatures (TTs) are highly influenced by the Ni/Ti ratio, which is affected by the LPBF process parameters [20]. Other works have observed how mechanical behavior is also influenced by processing conditions [21, 22]. However, there are still challenges in the AM of SMAs that must be addressed to fully achieve their potential. Some of them are associated with the optimization of AM process [23, 24]. Others are associated with the intercorrelation between the process parameters used during manufacturing and the final thermomechanical properties obtained which is not well understood [25, 26]. A systematic study of the process parameters and how they affect the final thermomechanical properties can open the door to the possibility of designing SMA metamaterials with tailorable thermomechanical properties. Some studies have reported interesting results on the manufacturing of LPBF SMAs by applying different sets of process parameters to distinct regions of the sample, successfully achieving different functional behaviors [27, 28]. However, there is limited understanding of the non-linear intercorrelations induced by the LPBF process during this complex manufacturing that affect the actuation behavior [27, 28]. Finally, the combined ability of LPBF to create complex structures and the tuneable capacity of NiTi SMAs observed in previous works in the literature, make LPBF NiTi SMAs promising candidates for the fabrication of complex structures, as cellular structures, with desirable thermomechanical behavior which can be used in a wide range of applications that need weight reduction combined with an actuation regime [29].

1.2 Historical background and overview

In 1932, Arne Ölander, a Swedish physicist, discovered the phase transformation in SMAs. He observed that gold-cadmium (Au–Cd) alloys could undergo plastic deformation upon cooling and revert to their original shape upon heating [30]. In 1938, Greninger and Mooradian were the first to document the SME in copper alloys [31]. The phenomenon of the shape memory effect, governed by the thermoelastic behavior of the martensite phase, was described a decade later by Kurdjumov and Khandros in 1949 [32] and subsequently by Chang and Read in 1951 [33]. During the 1950s, similar effects were also observed in other alloys, including indium-thallium (In–Tl) and copper-aluminum-nickel (Cu–Al–Ni).

Although the first NiTi alloy was discovered by William Buehler in 1959, the commercial potential of SMA applications became feasible only after Buehler and Frederick Wang demonstrated the SME in NiTi alloys in 1962 [34]. The first significant commercial success of an SMA application occurred with Raychem Corporation's CryoFit "shrink-to-fit" pipe coupler, which was used in the F-14 jet fighter developed by Grumman Aerospace Corporation. Later, in 1937, George B. Andreasen introduced orthodontic bridge SMA wires [34]. In the 1990s, the design and application of SMAs advanced, leading to their commercial use in various industries, including the automotive, aerospace, robotics, and biomedical sectors [35]. This shift was driven by the increasing demand for lighter and more compact actuators, particularly in the biomedical and aerospace sectors.

Despite the remarkable properties of NiTi SMAs for various industrial applications, their manufacturing process is challenging due to their poor workability arising from their low ductility, strong reactivity, and significant rebound effect, which cause the accelerated degradation of the work tool during conventional machining [36]. As a result, the production of 3D complex structures using conventional manufacturing methods remains a great challenge [37]. Consequently, only simple geometries, such as tubes, rods, wires, and sheets, are usually produced [38].

AM technology has emerged as a possible solution to solve the limitations of NiTi alloys using traditional manufacturing methods [39]. Unlike traditional subtractive manufacturing, which removes material to create shapes, AM allows topology optimization and the production of complex shapes in a continuous process. This reduces many of the assembly steps required in conventional methods, making it possible to reduce the process time [40].

AM has been shown to have many advantages over traditional manufacturing methods, such as the ability to create lightweight and custom structures, reduce waste, and minimize or eliminate assembly steps [41]. Due to these characteristics, AM has gained the attention of researchers and there is a lot of ongoing investigations into the manufacturing of NiTi alloys using AM methods [39, 23]. Among AM techniques, LPBF has become the preferred method for fabricating NiTi SMAs, as it provides high-quality surfaces and precise geometric dimensions [42]. Moreover, LPBF enables precise microstructural control over the sample, allowing for customized actuation properties and removing conventional manufacturing problems [28]. These advantages make LPBF particularly suitable for applications where accuracy and functional performance are critical.

As AM technologies continue to develop, it is anticipated that the NiTi industry will see further growth, leading to the creation of more sophisticated products. The worldwide market

for SMAs was worth USD 11 billion in 2021, with forecasts indicating an increase to USD 18 billion by 2026 and USD 44 billion by 2030, at an annual growth rate of 14% [43].

1.3 Statement of the problem

LPBF of NiTi alloys is challenging compared to other conventional alloys such as Ti-6Al-4V or steels. This is due to the spring-back nature, burr formation, and adhesion problems associated with NiTi alloys [44]. In order to ensure a good thermomechanical performance, SME and PE effects, and suitable phase transformation, the NiTi-made components must exhibit a high density and a correct microstructure. Therefore, a precise control of the energy input is needed to achieve these properties [45]. In addition, slight deviations in composition can alter the desired properties, while impurity levels exceeding the threshold can make the alloy unsuitable for most industrial applications [23, 46]. For example, the maximum impurity level for biomedical applications is 500 ppm [47]. Achieving the optimal combination of process parameters to produce NiTi alloys with high density, accurate chemical composition, low impurity levels, and desirable shape memory properties remains a significant challenge.

Currently, no clear guidelines have been discovered to obtain NiTi components with high density levels, low impurity levels, controllable phase transformation temperatures, and good thermomechanical properties. This can be caused by different reasons; for example, the LPBF process can be slightly different between machines [48] or the powder requirements can be different depending on the composition [49]. So, the optimum set of process parameters could vary between powders and machines, making difficult to predict the functional and mechanical properties of the final NiTi components.

In addition, the resultant effect of the process parameters on the functional and mechanical properties of the alloy is not yet systematically understood. This lack of understanding presents challenges in the optimization of the performance in NiTi for specific applications, particularly in industries where reliability and precision are critical (e.g., the aerospace sector) [50]. Great research efforts have been conducted to understand the effect of the LPBF process parameters on the alloy. These efforts aim to elucidate how variations in parameters such as laser power, scanning speed, hatch spacing and layer thickness influence key factors of LPBF NiTi SMAs such as phase composition, microstructural evolution, and defect formation [50, 51, 52, 53, 54, 55, 56]. Despite these studies, there is not an holistic understanding of the connection between the LPBF processing of NiTi SMAs and their thermomechanical features. So, a comprehensive investigation of the alterations observed in

the microstructure, transformation behavior and thermomechanical properties across a range of processing parameters is necessary.

Another challenge (and opportunity) is the design of graded materials with tailorable thermomechanical properties by local changes in the process parameters employed during the LPBF process. Some authors have achieved different thermomechanical behavior in the same solid structure by applying this strategy [27, 57, 28]. However, the resultant thermomechanical behaviour is not simply a direct arithmetic mean of the individual thermomechanical behaviour corresponding to each process parameter used; rather, a complex interplay of multiple factors is present, e.g., the thermal gradients appearing during the LPBF process, the residual stresses or the different chemical compositions between the processed areas. The challenge lies in the limited understanding of the non-linear intercorrelations induced by the LPBF process, which significantly influence the overall thermomechanical behavior of the material.

Finally, continuous advancements in understanding the production of NiTi alloys via LPBF are expected to significantly enhance the quality and consistency of manufacturing NiTi 3D structures such as lattice geometries [58, 59, 29]. With the previously cited opportunity of 4D printing technologies and the capabilities of LPBF in fabricating new tailored cellular structures ad-hoc, it can be expected that novel NiTi components with tailorable, advanced properties would emerge.

1.4 Objectives and thesis structure

Based on these unsolved challenges in regard to LPBF NiTi alloys, this work aims to achieve the following objectives:

1. **To investigate the effect of LPBF process parameters on the thermomechanical features:** This is done by studying the influence of laser power, scanning speed, and hatch spacing on the microstructure, transformation behavior, and thermomechanical properties on an equiatomic NiTi SMA. The study should establish direct correlations between the LPBF process parameters and key properties, such as phase transformation temperatures, strain recovery and mechanical behavior under different thermomechanical test conditions. Examine the role of LPBF-induced microstructural features, including precipitates and defects on determining the functional behavior of NiTi SMAs. Finally, investigate the influence of VED on phase transformation temperatures, microstructural, and thermomechanical behavior.

2. **Study the possibilities to develop spatially tailored NiTi SMA metamaterials:** The goal is to design and manufacture NiTi metamaterials with heterogeneously programmed LPBF conditions, allowing spatial control over phase transformation behavior and thermomechanical response. This involves investigating how different spatial 3D patterns in LPBF influence the transformation behavior and overall thermomechanical performance of SMA samples. In addition, the study explores the fabrication process of various patterned geometries and examines how each geometry affects the microstructure, and therefore the final thermomechanical response.

3. **Design and fabrication of ultraelastic NiTi SMA cellular structures:** The objective is to design and manufacture NiTi ultraelastic cellular structures using LPBF while studying how LPBF parameters influence the microstructural features and functional properties of NiTi lattice structures. This includes examining how variations in geometry and processing conditions impact the thermomechanical performance and structural manufacturability of NiTi lattice structures compared to bulk material. Furthermore, the research aims to demonstrate the feasibility of programming localized properties within a single lattice structure by spatially adjusting process parameters, enabling the creation of heterogeneous designs with optimized performance.

To address the proposed objectives, the thesis is organized as shown in Figure 1.1. Chapter 2 presents a complete review of the topic. The chapter begins with an examination of the physical properties of SMAs and their types, followed by a depth analysis of the NiTi alloys. Furthermore, the current state of AM techniques applied to SMAs and their applications are reviewed.

Chapter 3 explores an initial process optimization analysis of the LPBF process parameters. The interrelationship between the process parameters of the manufacturing process, the quality of the resulting sample, and the phase transformation behavior is analyzed and correlated.

Chapter 4 investigates the thermomechanical behavior of the LPBF NiTi samples. To achieve this, various sets of process parameters carefully selected from the previous chapter are used to fabricate tensile NiTi specimens. These samples are tested under different conditions to perform a complete analysis of their thermomechanical properties. Correlations between the applied process parameters and the resulting thermomechanical properties are identified and analyzed.

Chapter 5 focuses on the design of heterogeneous graded metamaterials through localized variations in processing conditions. Tensile samples with different pattern geometries are fabricated using combinations of the parameter sets examined in the previous chapter. The

thermomechanical behavior of the patterned samples is analyzed and compared to that of monoparameter samples, which are fabricated without pattern geometries. Thermal simulations of the laser track are used to rationalize the complex phenomena occurring during the manufacturing of the patterned geometries.

Chapter 6 focuses on the design, manufacturing and testing of cellular NiTi structures. Both the manufacturability of these structures and their thermomechanical behavior are investigated. The differences in the thermomechanical features between the bulk material and the lattice structures are discussed. The results of the lattice geometries are compared with those of other studies. Structural simulations are used to assess the effect of the geometry on the phase transformation and the actuation behavior.

Finally, Chapter 7 presents a general discussion of the findings of the previous chapters, and Chapter 8 summarizes the key conclusions and contributions to the field, while also identifying directions for future research.

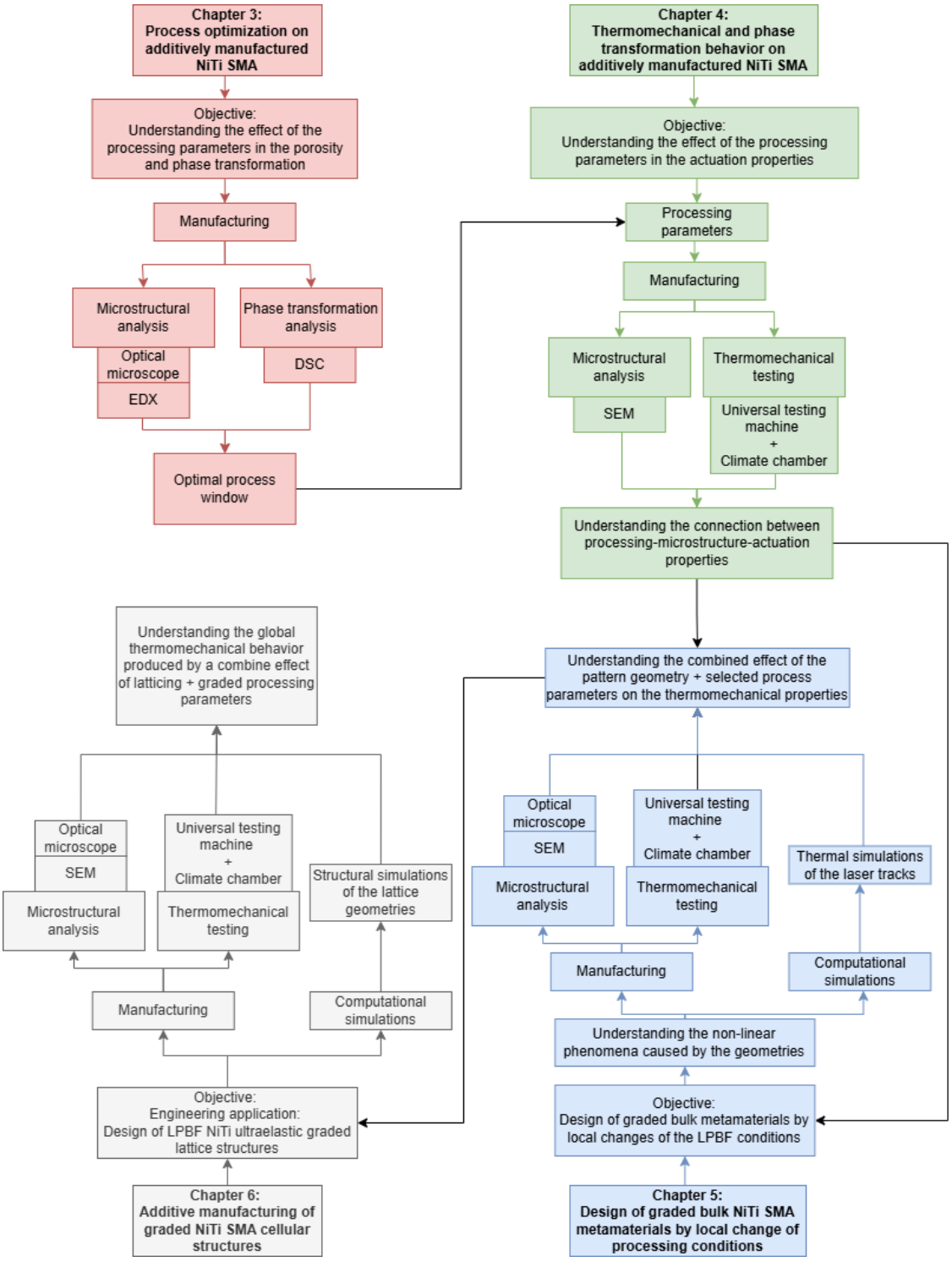


Figure 1.1: Thesis structure showing the key research carried out.

Chapter 2

State of the art

2.1 Types of SMAs

SMAs can be classified based on their chemical composition, TTs range, and functional features. The most widely studied SMAs are NiTi based alloys as a result of its characteristics as discussed in the previous chapter. However, for applications with other requirements, other types of SMAs, such as NiTi-based high-temperature SMAs (HTSMAs), have been developed adding elements like Hf, Zr, Pt, Pd. In addition, copper-based SMAs offer cost-effective alternatives, although they often exhibit lower mechanical performance compared to NiTi-based alloys. This section provides an overview of the most important types of SMAs based on their composition.

2.1.1 NiTi-based alloys

NiTi alloys exhibit SME, TWSME, and PE behavior under the right conditions. This makes them ideal for various applications. For example, in the aerospace sector, NiTi tendons are used to control jet engine nozzles [60]. Other examples in the biomedical sector are NiTi orthodontic arches that use the PE effect to exhibit minimal stress variations over a significant strain range [61]. In addition, these alloys demonstrate excellent corrosion resistance and biocompatibility, making them suitable for biomedical applications [6]. The equiatomic NiTi composition exhibits the highest austenite finish temperature (A_f) of all the NiTi compositions studied (400 K) [62]. However, as the Ni content increases beyond 50 at.%, the TTs decrease, resulting in a reduction in A_f to 233 K at 51 at.% of Ni content [63]. These compositional variations can influence the properties of the material, changing its behavior at

room temperature from SME to PE [62].

Other studies have also investigated the properties of NiTi alloys with a composition of 55 at.% Ni [64]. This composition shows a range of TTs between 260 to 330 K. Due to its chemically multiphase nature, the alloy shows low transformation strains. However, this composition has been shown to have superior corrosion resistance compared to stainless steel in aggressive environments such as saltwater baths or salt fog conditions [65]. Furthermore, this alloy exhibits excellent thermomechanical stability, which allows for precise control of TTs through heat treatments, and can be hot-formed into various geometries [66].

2.1.2 NiTiCu alloys

The addition of Cu to the NiTi system preferentially replaces Ni, leading to the formation of NiTiCu alloys. Cu is known to have a beneficial effect on the physical properties of NiTi alloys [67, 68]. Specifically, the substitution of Ni by Cu improves the SME by reducing the transformation hysteresis, decreasing the sensitivity of TTs to chemical composition, and improving the fatigue life [69, 70]. Nam *et al.* reported that increasing the Cu content in NiTiCu alloys reduces temperature hysteresis and alters the phase transformation behavior from a single step transition to a two-step thermoelastic transformation involving cubic to orthorhombic to monoclinic phases [71]. However, this modification also results in a reduction of the transformation strain. For example, in NiTi alloys containing 10 at.% Cu, the transformation strain is significantly lower than that of the binary NiTi alloy, with an overall strain reduction of approximately 4% [71]. Furthermore, Mercier *et al.* [72] demonstrated that the substitution of Ni for Cu induces notable changes in TTs.

2.1.3 NiTiZr alloys

Zr is an ideal ternary element to add to NiTi alloys to increase TTs [73]. The addition of Zr leads to the formation of precipitate phases that significantly contribute to the improvement of the thermomechanical properties [74]. For example, NiTiZr alloys promote the precipitation of an orthorhombic phase known as the H-phase [75]. Preliminary studies suggest that NiTiZr alloys with H-phase precipitation exhibit better PE properties and improved SME behavior [76]. Furthermore, the use of Zr over Hf presents several advantages, including a 20% weight reduction when comparing NiTi-20Hf and NiTi-20Zr alloys, as well as an important cost reduction [74].

2.1.4 NiTiPt alloys

TTs decrease with the addition of Pt in the range of 0 to 10 at.%, and above 10 at.%, these temperatures increase linearly with the Pt content [77]. The slight decrease in TTs with the introduction of Pt is an advantage in maintaining PE behavior at room temperature. Furthermore, NiTiPt alloys exhibit good deformation recovery when they are deformed below the martensite finish temperature (M_f) and subsequently heated to room temperature, with minimal dependence on the percentage of the alloying element [78]. NiTiPt alloys show thermomechanical recovery behavior nearly identical to that of Ni-rich NiTi SMAs. Moreover, NiTiPt alloys show significantly smaller stress hysteresis and reduced temperature dependence of transformation stress compared to NiTi alloys [77].

2.1.5 NiTiPd alloys

NiTiPd alloys are one of the most promising systems, offering a similar processability as binary NiTi alloys and also providing good work output at elevated temperatures. Some studies have shown that residual strain accumulation can be produced during the thermomechanical cycling of NiTiPd alloys, particularly it happens in those containing between 20 and 30 at.% of Pd content [79]. Despite the development and study of various NiTiPd alloys over the years, their use in engineering applications has been limited due to the high cost of Pd. However, they have been considered for specific aerospace components [80]. Furthermore, the commercial success of this system has been hindered by unresolved challenges related to dimensional and thermal stability [80].

2.1.6 NiTiHf alloys

The addition of Hf, Zr, Pd, and Pt to NiTi has been shown to produce an increase in TTs [81]. However, the high cost of Pd and Pt prevents their use in critical applications. On the other hand, Zr exhibits a strong affinity for O, which can affect the processing of the alloy and the performance [82]. Among the available HTSMAs, NiTiHf is a promising candidate due to its relatively low cost, moderate ductility, and high work output. These attributes make NiTiHf suitable for applications operating in a temperature range of 300–400 K [83].

The TTs of NiTiHf alloys exhibit a short increase until the Hf content reaches 10 at.%. However, beyond this threshold, these temperatures increase linearly, reaching approximately 800 K at 30 at.% Hf content when Hf is substituted for Ti [84]. TTs remain unaffected by

variations in Ni content as long as the alloy remains Ni-lean, but they decrease drastically when Ni concentration exceeds the equiatomic composition (50 at.%), which is consistent with the behavior of NiTi alloys [84]. Despite their potential advantages, Ni-lean NiTiHf alloys have several disadvantages, including large hysteresis (>50 K), poor room-temperature ductility, limited cyclic stability due to the high stress required for martensite reorientation and detwinning, low slip strength, and poor formability [85].

2.1.7 Phase transformation and actuation properties of the differnet types of SMAs

Figure 2.1 presents the A_s temperature and recoverable strain for SMAs that use different alloying elements. As can be observed in Figure 2.1a, the A_s temperature follows two different trends. On the one hand, as explained previously, different alloying elements increase TTs with NiTiPd, NiTiPt, and NiTiHf being the ones with higher A_s temperature. On the other hand, a clear trend is observed with at.% Ni content regardless of the alloying elements: as the Ni concentration increases, the A_s temperature decreases. This behavior is consistent with findings reported in the literature [86]. In the case of recoverable strain (see Figure 2.1b), no clear trend is observed with Ni content or alloying elements. It can also be observed how for the same group of SMAs, a wide range of A_s and recoverable strains is achieved, which means that not only the composition plays a critical role in the final phase transformation and thermomechanical properties. Post-processing treatments can alter the actuation features of the SMA [87, 88].

2.2 Physical metallurgy of NiTi SMAs

2.2.1 Phases and crystal structures

Near-equiatomic NiTi SMA is most frequently found in the following phases: body centered cubic (B2) austenite, the high temperature phase [11]. The monoclinic structure martensite phase (B19´) occurs at lower temperatures [11]. Furthermore, B2 can occasionally change into the rhombohedral structure R-phase. The extended characteristics of the crystallographic phases are described as follows:

- **Austenite or B2 phase:** Is a cubic ordered structure with a lattice constant a_0=0.3015 nm (see Figure 2.2a). This crystallographic phase is usually considered the parent phase

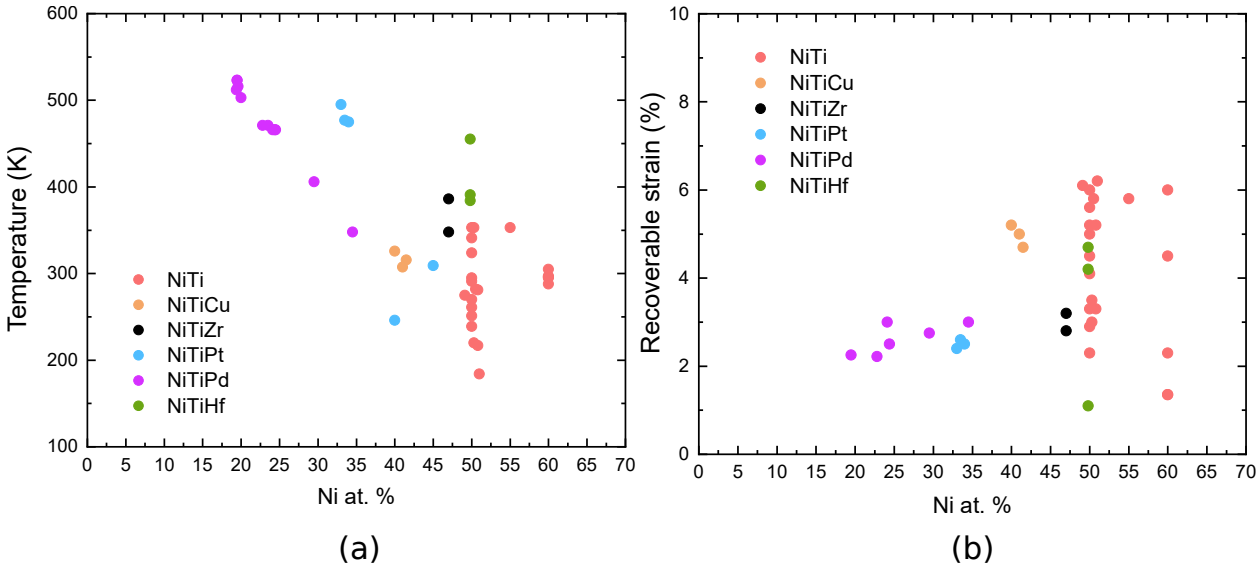


Figure 2.1: (a) Austenite start temperature (A_s) and (b) recovery strain of NiTi, NiTiCu, NiTiZr, NiTiPt, NiTiPd and NiTiHf alloys extracted from the literature. See Tables 1 and 2 in the Annex for more details.

when the phase transformation process is described in NiTi.

- **Martensite or B19´:** This phase is composed of a monoclinic structure (see Figure 2.2b) and does not have standard lattice parameters, which depend on the composition of the alloy and the temperature. The lattice parameters reported by Hane *et al.* [89] in 49.75 at.% Ni are: a=0.2889 nm, b=0.4120 nm, c=0.4662 nm and β=96.88°.
- **R-phase:** Is an eloganted version of B2 phase in <111> direction (see Figure 2.2c). According to Sitnner *et al.* [90], the lattice parameters of R-phase are: a=0.73535 nm, c=0.52582-0.52759 nm for α=89.57-89.32°.

2.2.2 Phase transformation phenomenology

As previously reported, NiTi SMAs have mainly two phases, austenite at high temperatures and martensite at low temperatures. The phase change depends on the applied temperature and stress. As shown in Figure 2.3 there are four characteristics transformation temperatures. Two indicates the start and the end of the austenite→martensite transformation (M_s and M_f, respectively). The other two TTs indicate the start and the end of the martensite→austenite transformation (A_s and A_f, respectively). As can be observed, the TTs increase with stress level. The shape of this diagram is strongly influenced by the Ni/Ti ratio, thermal history (heat treatments), the cold working and the presence of other alloy elements [86, 91, 92, 93].

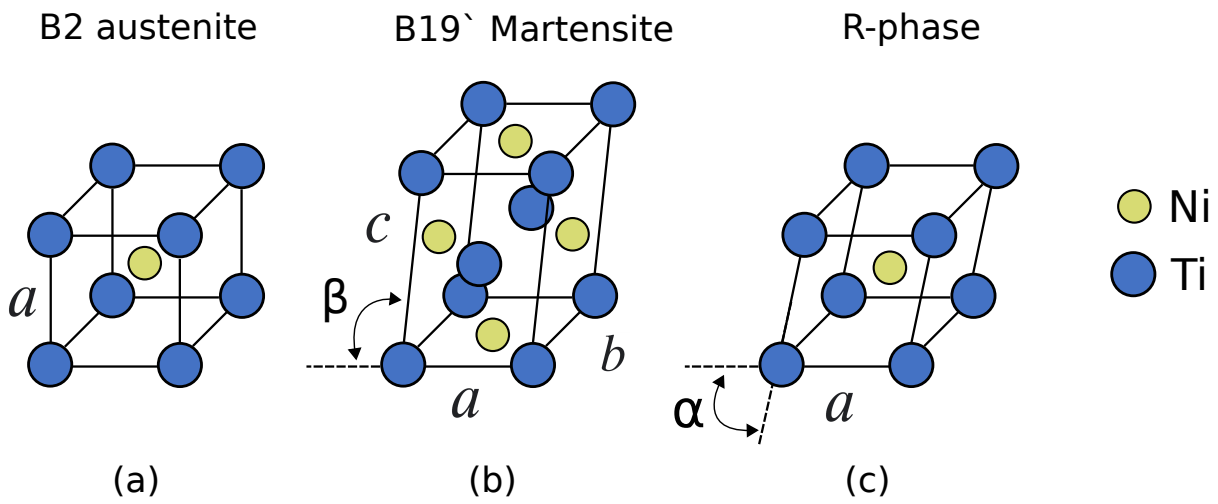


Figure 2.2: Crystallographic phases observed in near equiatomic NiTi: (a) B2 austenite, (b) B19´ martensite and (c) R-phase.

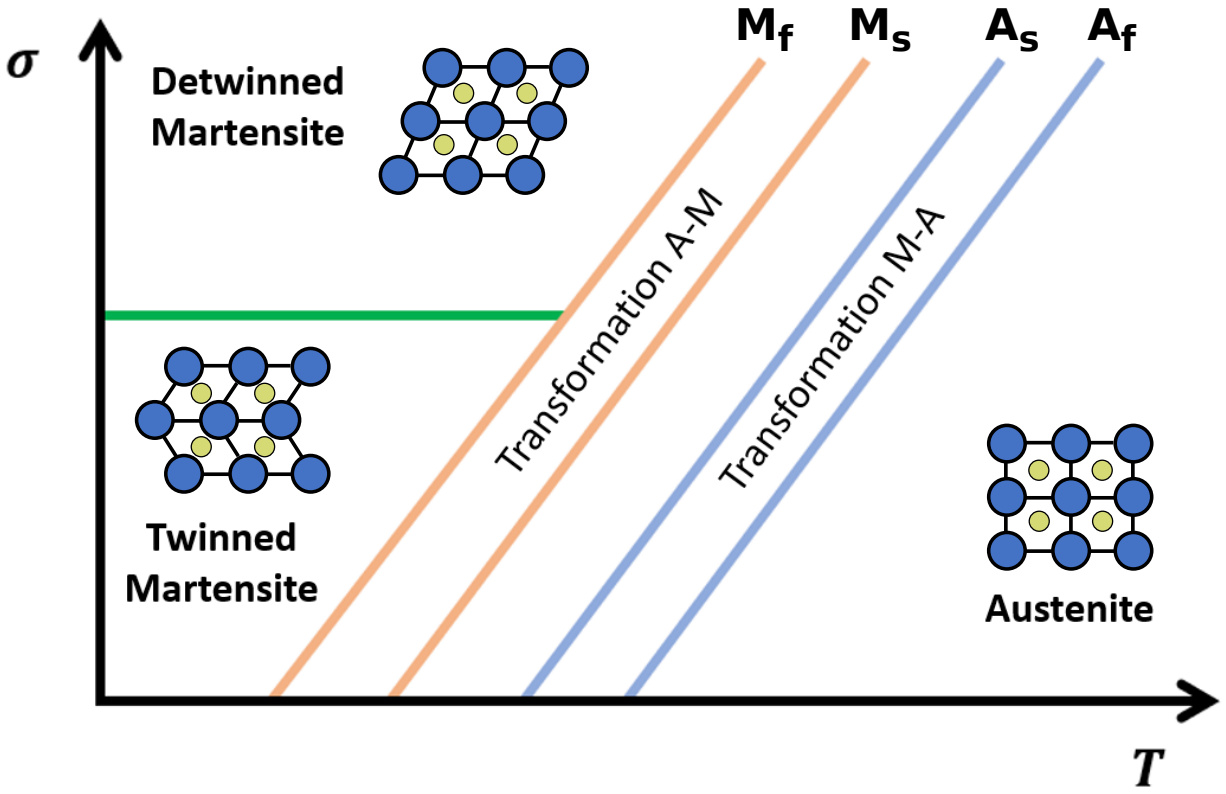


Figure 2.3: Typical stress-temperature transformation map of NiTi SMAs.

The transformation from B2 austenite to B19´ martensite (forward transformation) follows a diffussionless process [94] where sometimes the crystal structure sometimes goes through the intermediate phase (R-phase). The transformation begins along the habit plane or invariant plane, which delimits the parent phase from the transformation region and occurs by shear distortion of the lattice structure [95]. This plane does not rotate or deform (see Figure 2.4) [95]. Each martensite unit cell formed can have different crystallographic orientations with respect to the parent phase, which is called variant. The number of variants that can be formed depends on the crystal structure of the martensite and its lattice correspondence with the parent phase unit cell [96]. A twin plane is a crystallographic plane that separates two variants that are mirror images of each other. In the transformation process, there are different families of twin planes in which twinning can occur along certain associated directions [97]. Specifically, in NiTi systems, in the cubic lattice of the parent austenitic phase, the twinning can occur along the {011} planes. There are six {011} planes and two directions for the twinning to occur along each plane, there exist 12 equivalent martensite variants. So, there are 12 equivalent martensitic twins. Each twin is composed of two different martensite variants, so there are a total of 24 martensitic habit planes in most NiTi systems [98].

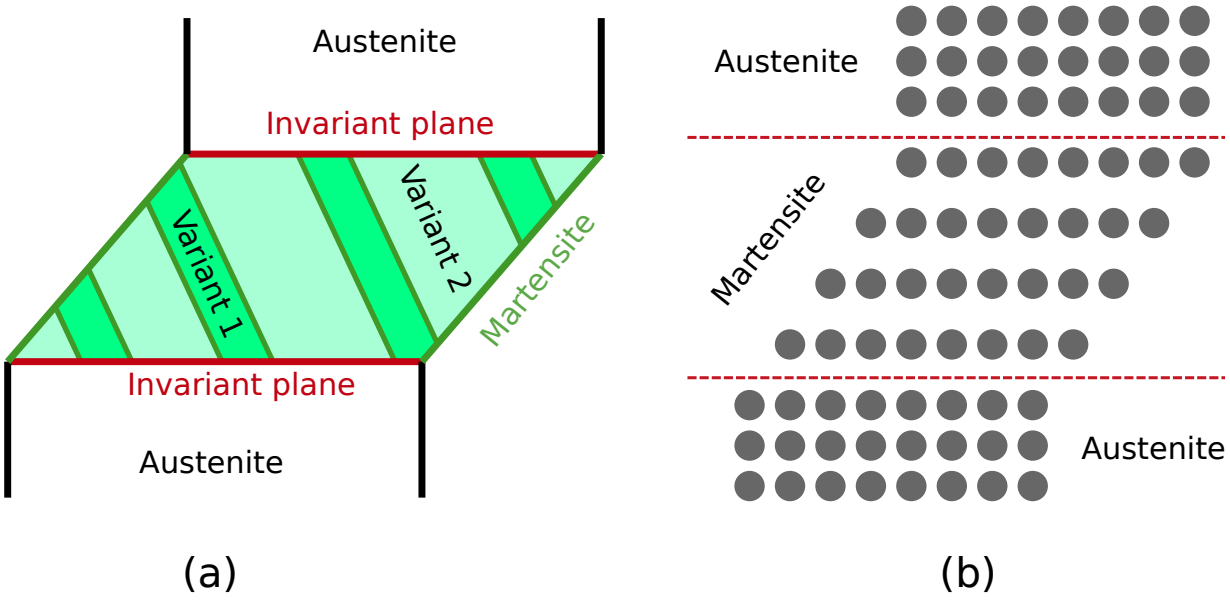


Figure 2.4: (a) austenite-martensite interfaces during the transformation. (b) Simplified model of the shear mechanism during the transformation.

Once the martensite phase has been reached, its crystal structure can exist in two different forms: twinned, in which the variant is "self-accomodated" or detwinned. Twinned martensite results in the formation of commonly called multi-variant [94]. The macroscopic change between austenite and twinned martensite is negligible as a result of the absence of a

predominant transformation direction. The other form of martensite is detwinned martensite in which the martensite is reoriented in a specific or dominant direction caused by an external force. When the material is heated, the martensite becomes unstable and the reverse transformation occurs. Martensite reverts to the parent phase in the original orientation [99].

Beginning at an unloaded condition, in the martensite phase, it is possible detwinning the martensite by applying a certain stress (see Figure 2.5). This detwinning starts at detwinning start stress σ_s, and ends at the detwinning finish stress σ_f. Detwinned martensite became the minimum energy phase, so, when the load ceases, the martensite will continue detwinned except for a slight elastic recovery, with a macroscopic permanent deformation or strain. To recover SMA original shape (austenite) it is necessary to heat again above A_f. Regardless of whether it is twinned or detwinned, the crystal structure transforms again to the original parent austenite phase (reverse transformation).

2.2.3 Binary phase diagram and precipitates

The binary phase diagram of NiTi alloys, shown in Figure 2.6, is very important in the production of NiTi alloys due to the fact that composition plays a determinant role in the TTs and the functional properties of the alloy (see Figure 2.1) [100]. NiTi SMAs are intermetallic compounds situated in the core region of the phase diagram. Their composition lays between ∼49-57% [86]. The graph indicates that the melting temperature (before the liquid phase) for the intermetallic NiTi phase is 1583 K. For NiTi alloys there are two well-defined frontiers. On the left, in the Ti-rich side, the boundary of NiTi is practically vertical. Consequently, the NiTi phase is stable in Ti-rich composition even at low temperatures. On the right, the Ni content is limited to a maximum of 57% at 1391 K. Below this temperature, the solubility of Ni decreases. At temperatures below 930 K, the NiTi regions become narrow.

Extreme compositions rich in Ni or Ti often exhibit some precipitation reactions [101, 102]. The evolution of metastable and stable phases of NiTi using Ni-rich compositions at different temperatures was studied by Nishida *et al.* [103], founding three possible scenarios:

For NiTi aged at temperatures below 950 K:

$$\mathrm{TiNi} \rightarrow \mathrm{TiNi} + \mathrm{Ti_3Ni_4} \rightarrow \mathrm{TiNi} + \mathrm{Ti_2Ni_3} \rightarrow \mathrm{TiNi} + \mathrm{TiNi_3}$$

For NiTi aged at temperatures between 950 K and 1023 K:

$$\mathrm{TiNi} \rightarrow \mathrm{TiNi} + \mathrm{Ti_2Ni_3} \rightarrow \mathrm{TiNi} + \mathrm{TiNi_3}$$

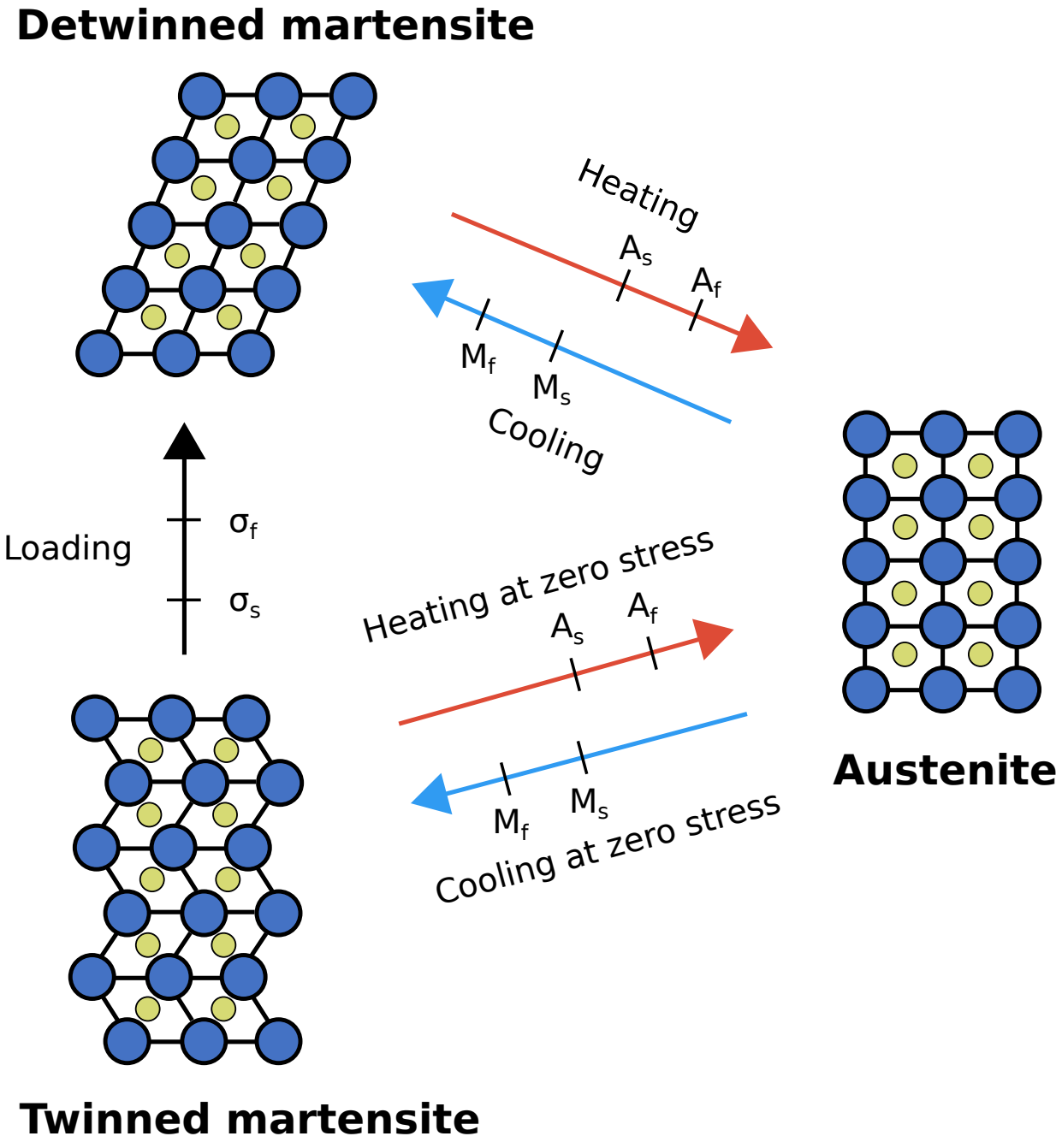


Figure 2.5: Typical observed phase transformation paths in NiTi SMAs. A_s, A_f, M_s and M_f TTs are not the same temperatures in loaded and unloaded conditions (see Figure 2.3).

For NiTi aged at temperatures between 1023 K and 1073 K:

$$\mathrm{TiNi} \rightarrow \mathrm{TiNi} + \mathrm{TiNi_3}$$

So, Ni-rich precipitations and the phase state of NiTi are highly dependent on the temperature and aging time [104]. Ti_3Ni_4 precipitates have been widely studied. The martensitic transformations in Ni-rich TiNi alloys are strongly influenced by the presence of Ti_3Ni_4 precipitates [105]. Furthermore, these precipitates resulted in high strength properties of the austenite phase and a wide PE temperature range [106, 107].

Conversely, Ti_2Ni is formed in Ti-rich alloys at temperatures below 1257 K [102]. Previous research has shown that the development of Ti_2Ni precipitates in NiTi SMAs significantly affects their thermomechanical properties [12]. These precipitates modify the martensitic transition temperature by absorving Ti atoms from the matrix [108]. Furthermore, they may lead to premature fracture during plastic deformation, significantly reducing ductility [109].

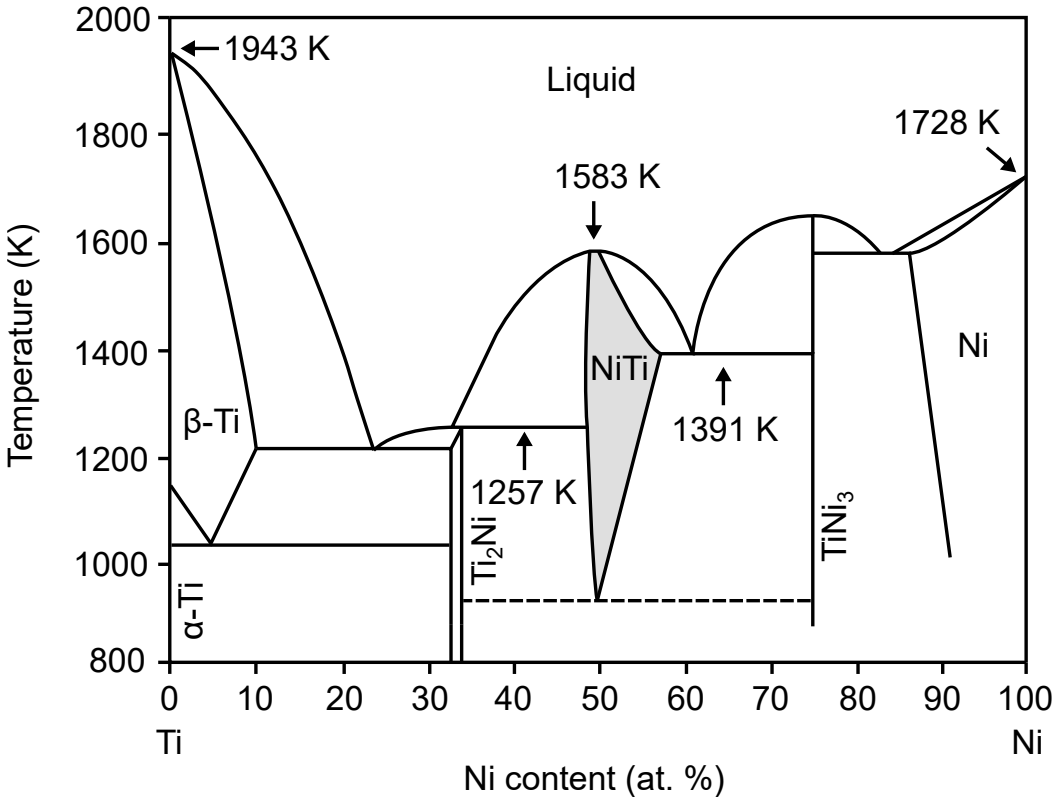


Figure 2.6: Binary phase diagram of NiTi alloys [110].

2.3 Thermomechanical properties of SMAs

2.3.1 Shape memory effect (SME)

SME occurs when an SMA in the twinned martensite phase is mechanically deformed (see Figure 2.7). Upon applying a stress to the twinned martensite that surpasses the initial detwinning stress level σ_s, the reorientation step is initiated, leading to the growth of the favorably oriented martensitic variants at the expense of less favorable ones. The process of detwinning is completed at a stress level σ_f, marked by the termination of the plateau in the stress-strain curve. Consequently, the transition from the twinned to the detwinned martensite phase occurs (points A-B). Following this, the material is unloaded elastically (points B-C), with the SMA remaining in the detwinned martensite state. It is crucial to highlight that the entire deformation sequence (points A-C) takes place below A_s. Subsequently, the material is heated without stress application. Upon reaching the A_s, the reverse transformation from martensite to austenite begins and finalizes at A_f. Due to the absence of permanent plastic deformation from detwinning, the SMA returns to its original shape (points C-D). Re-cooling to the martensite phase results in self-accommodated twinned martensitic variants forming without any shape change, enabling the SME cycle to be repeated (points D-A).

2.3.2 Pseudoelasticity (PE)

This behavior is the result of a stress-induced transformation, which generates strain during loading and allows for strain recovery upon unloading (see Figure 2.8). A pseudoelastic path initiates at temperatures where the austenite phase is stable (above A_f). When mechanical load is applied, the austenite phase exhibits elastic deformation (points A-B). At a specific stress level, the transformation to martensite begins. The austenite-to-martensite transformation progresses until reaching M_f, marking the transformation's completion (points B-C). This completion is reflected by a change in slope in the stress-strain diagram. Once the transformation is complete, further stress increase results only in elastic deformation of the detwinned martensite (points C-D). Gradual stress release during unloading allows the martensite to elastically unload along the path (points D-E). At a certain stress level, the A_s temperature is reached and the transformation from martensite to austenite starts. From this point onward, strain recovery due to phase transformation occurs upon unloading completion (points E-F). After the reverse transformation concludes at A_f, the material elastically returns to its initial state (points F-A).

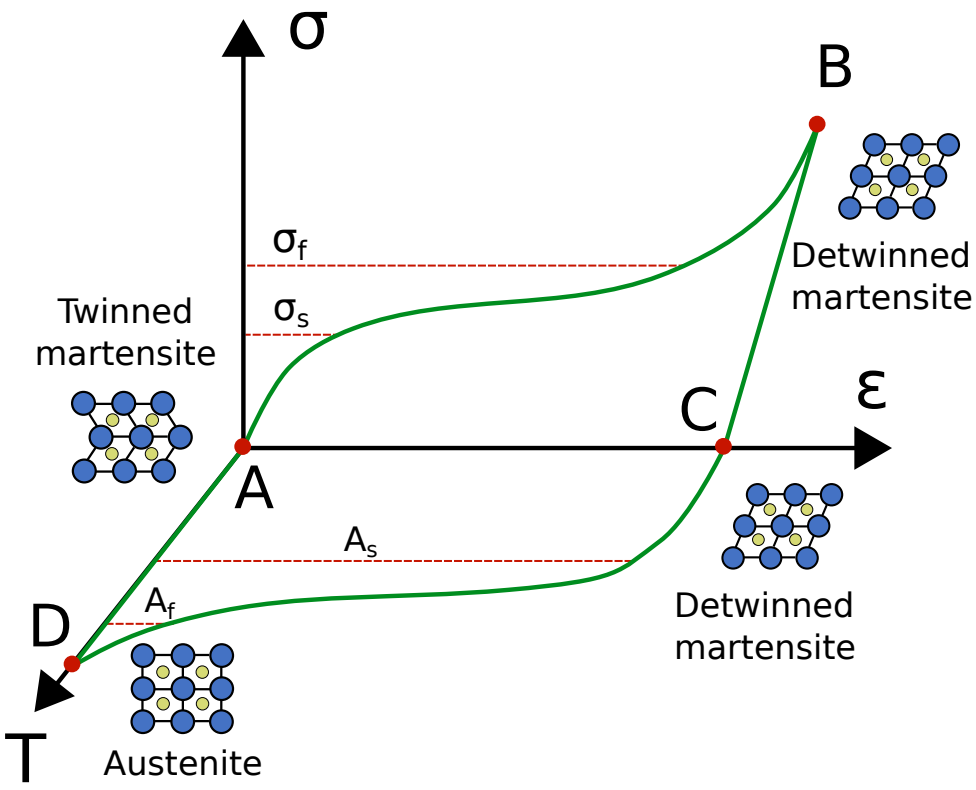


Figure 2.7: Stress-strain-temperature diagram showing the shape memory effect of SMAs.

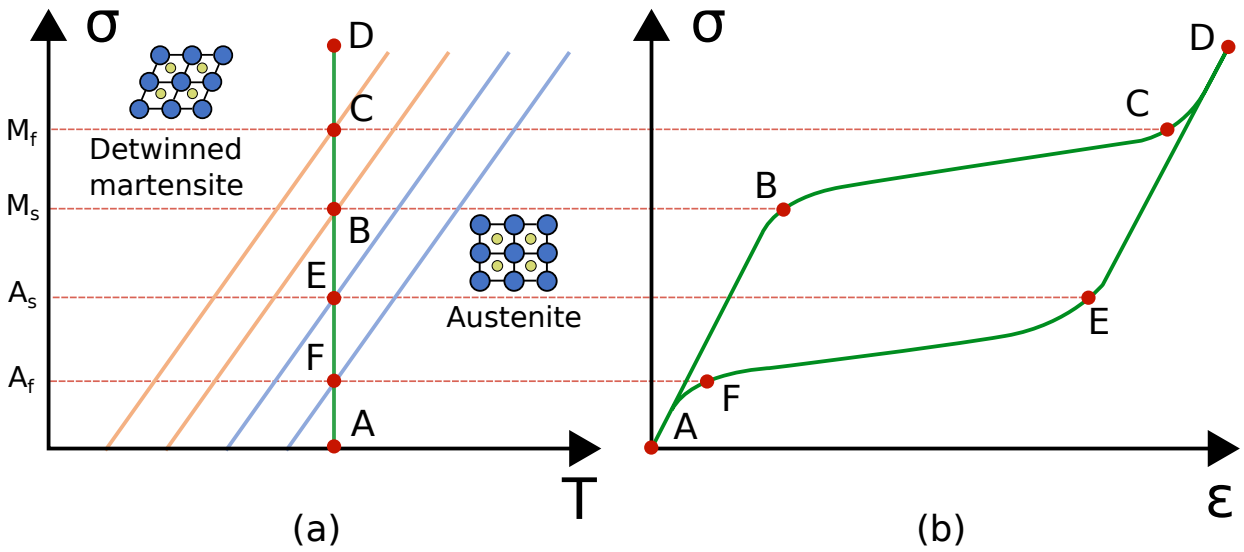


Figure 2.8: (a) Stress-temperature and (b) stress-strain diagrams showing a pseudoelastic path of SMA.

2.3.3 Cyclic behavior

An SMA can undergo repeated shape transformations without mechanical load when exposed to cyclic thermal loading, a phenomenon termed the two-way shape memory effect (TWSME). This effect is observable in an SMA that has been subjected to multiple thermomechanical cycles along a particular loading path until its hysteretic response stabilizes and the inelastic strain reaches saturation. This process, referred to as training, can be carried out either by maintaining a constant stress level during thermal cycling or by engaging in repeated pseudoelastic cycles at a temperature above A_f (see Figures 2.9). Regardless of the path chosen, training involves continual phase transformations between austenite and martensite during the cycles. The initial cycle induces some permanent strain, which is irreversible or plastic. As cycling continues, the amount of new permanent strain introduced by each cycle diminishes gradually until it nearly ceases. The TWSME results from defects introduced during training, which create a state of residual internal stress. This evolves into the preferential formation of specific martensitic variants when the SMA is subsequently cooled without external forces.

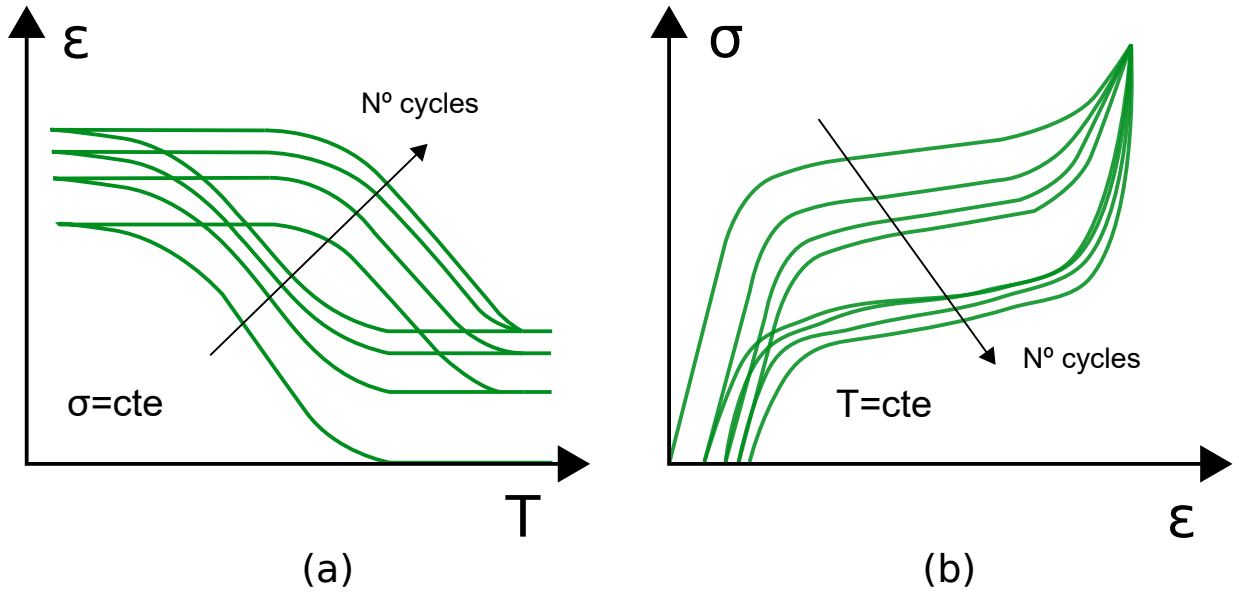


Figure 2.9: Different training paths: (a) constant stress during thermal cycles, and (b) constant temperature during PE cycles.

2.4 Additive manufacturing of NiTi alloys

2.4.1 Introduction to additive manufacturing

Additive manufacturing (AM) is characterized as a technique for assembling materials to create objects from three-dimensional model data, typically by building them layer by layer, in contrast to subtractive production methods [111]. This definition is widely relevant across various material categories, such as metals, polymers, ceramics, composites, and biological systems. AM has arguably been used for material processing for more than twenty years. However, it has only recently begun to become a significant technology in the realm of commercial manufacturing [112].

AM systems can be classified into three categories: powder bed systems, powder feed systems, and wire feed systems [113]. In powder bed systems, a layer of powder is formed by spreading it over the work area using a raking tool. The energy source, whether an electron beam or a laser beam, is configured to impart energy to the bed's surface by melting or sintering the powder into the intended form. Successive layers of powder are distributed over the workspace, and the process is reiterated to fabricate a solid three-dimensional component. The benefits of this technique include its capability to achieve high-resolution features and preserve dimensional accuracy. Typically, the build volumes are smaller compared to other additive manufacturing methods. [114].

In systems utilizing powder feeding, powders are directed via a nozzle onto the build surface. A laser then melts one or more layers of the powder to form the intended shape. This procedure is executed iteratively to fabricate a solid three-dimensional object. There are two primary system configurations available commercially: one where the workpiece is fixed while the deposition head moves, and another where the deposition head is fixed and the workpiece is mobile. The advantages of such systems include a larger build volume capability and the ability to refurbish worn or damaged components. [115].

In wire feed systems, the feedstock utilized is wire, and the energy sources for these units may involve an electron beam, a laser beam, or a plasma arc. A material bead is initially deposited, followed by subsequent layers to build a three-dimensional structure. Typically, wire-feed systems are well-suited for high-deposition rate processes and accommodate large build volumes. However, the resulting product generally demands more extensive machining compared to powder-bed or powder-fed systems. [116].

Powder bed systems are better for applications that require precision, complexity, and surface

quality, making them ideal for high value industries. However, for large scale production or repair work, powder feed systems and wire feed systems might be more efficient.

2.4.2 Additive manufacturing of NiTi SMAs

NiTi is used in powder bed fusion (PBF) systems to create complex, high performance parts that require unique material properties. Laser Powder Bed Fusion (LPBF) and Electron Beam Melting (EBM) are PBF methods for processing NiTi alloys because both are capable of fully melting the metal powders needed to produce dense parts. LPBF technology might be preferred to EBM due to its superior manufacturing capabilities [39]. Few studies on EBM NiTi are available [117, 118]. The high vacuum conditions of EBM are suitable for reactive materials such as NiTi [119]. However, poor surface roughness adversely affects the fatigue performance of the EBM components [26]. Moreover, one might think that in EBM the simultaneous preheating of both substrate and powder bed should promote microstructural homogenization. However, as highlighted in previous studies, the grain size progressively increases from the upper to the bottom regions, both in the longitudinal and transverse directions. This variation arises due to the distinct thermal histories experienced by different regions of the sample during processing [120]. Furthermore, EBM technology is limited in producing 3D structures with precise geometry due to its large beam size [121], which leads to the formation of a large molten pool [122]. The EBM process also necessitates significant machining allowances to facilitate comprehensive post-processing operations, aiming to achieve the geometry specified by the CAD design and desired surface quality. These operations increase production costs, extend manufacturing time, and result in material waste [121]. Currently, there is a market demand for manufacturing 3D NiTi structures with complex geometric configurations, since the finished NiTi AM components are utilized in high-value industrial applications that require high-quality surface finishes and precise geometric dimensions [42]. Consequently, NiTi alloys for AM are predominantly used in LPBF. According to Wang *et al.* [123] and Xiong *et al.* [124], LPBF yields high-resolution structures and improved build accuracy compared to other AM processes, with a dimensional error of less than 100 μm and samples exhibiting surface roughness of <2 μm.

2.4.3 Fundamentals of LPBF

LPBF represents an AM process that has transformed the manufacturing sector by facilitating the creation of intricate structures in a cost-effective and time-efficient way. This technique

also allows the construction of complex geometries without the need for traditional tools, casting, or other manufacturing approaches [125]. A typical LPBF system consists of a laser source, a building platform, an automated powder delivery system, a control system, and auxiliary components such as rollers and scrapers. The high-intensity laser beam's movement and focus is managed by a beam deflection system composed of galvanometer mirrors and a flat-field focusing lens [126].

Figure 2.10a displays the schematic of a typical LPBF machine. First, the 3D part to be produced is sliced into a 3D software which defines the number of layers with a specific lawyer thickness. For fabrication, a build plate is fixed to the build platform. This is the base level upon which the powder layers are deposited. Subsequently, the build chamber is transferred to an inert atmosphere, such as argon, nitrogen, or even a vacuum, which is essential during the LPBF process to reduce oxidation and impurity absorption (such as O_2 or C). This helps improve surface quality, density, and conformity [127]. As noted in ASTM F2063-05, the impurity levels in the components produced should be less than 500 ppm [128]. Then the manufacturing process begins, the powder supply platform rises its level, and the roller spreads the powder on the build platform. After the layer is deposited, the laser scans along the predetermined path across the powder bed to construct the layer according to the instructions specified by the CAD software and the designed model. Finally, the building platform is lowered one layer and the last two steps of spreading the powder bed and scanning it multiple times are repeated until the finished part is produced.

Different physical phenomena occur during LPBF, including reflection, absorption, heat transfer, solidification and chemical reactions [129]. The formation of the melt pool occurs when the laser's energy is transformed into thermal energy. The influence of the surface tension often lead the melt pool to assume a circular or segmented cylindrical shape [130]. Due to the very brief interaction period between the laser and the powder bed, temperature fields can reach values up to 1300 K. This brief interaction during the LPBF process also leads to rapid cooling, which could alter the microstructure. [131].

The LPBF process is controlled by processing parameters (see Figure 2.10b), including:

- **Laser power (P):** Determines the energy input for the melting powder.
- **Scan speed (v):** Is the speed at which the laser moves across the powder bed.
- **Hatch spacing (h):** Is the distance between adjacent laser tracks.
- **Layer thickness (t):** Is the perpendicular distance of each deposited powder layer.

They play a crucial role in ensuring complete melting of the powder and effective fusion with

the preceding layer. If these parameters are not adequately selected, defects such as thermal cracks, balling, and porosity can occur [132]. In addition, it is essential that the components are produced with high density; otherwise, their mechanical features might degrade. The achievement of such a density depends primarily on the processing parameters employed in the LPBF process [133].

Using these fundamental processing parameters, additional energy-related parameters can be calculated to further characterize the LPBF process. The energy density plays a critical role in the regulation of the melting behavior, microstructural evolution, and mechanical performance of the fabricated components [134, 135, 136, 137]. Two key parameters of energy density commonly used in LPBF analysis are the Linear Energy Density (LED) (2.1) and the Volumetric Energy Density (VED) (2.2).

$$\mathrm{LED} = \frac{\mathrm{P}}{\mathrm{v}} \tag{2.1}$$

$$\mathrm{VED} = \frac{\mathrm{P}}{\mathrm{v} \cdot \mathrm{h} \cdot \mathrm{t}} \tag{2.2}$$

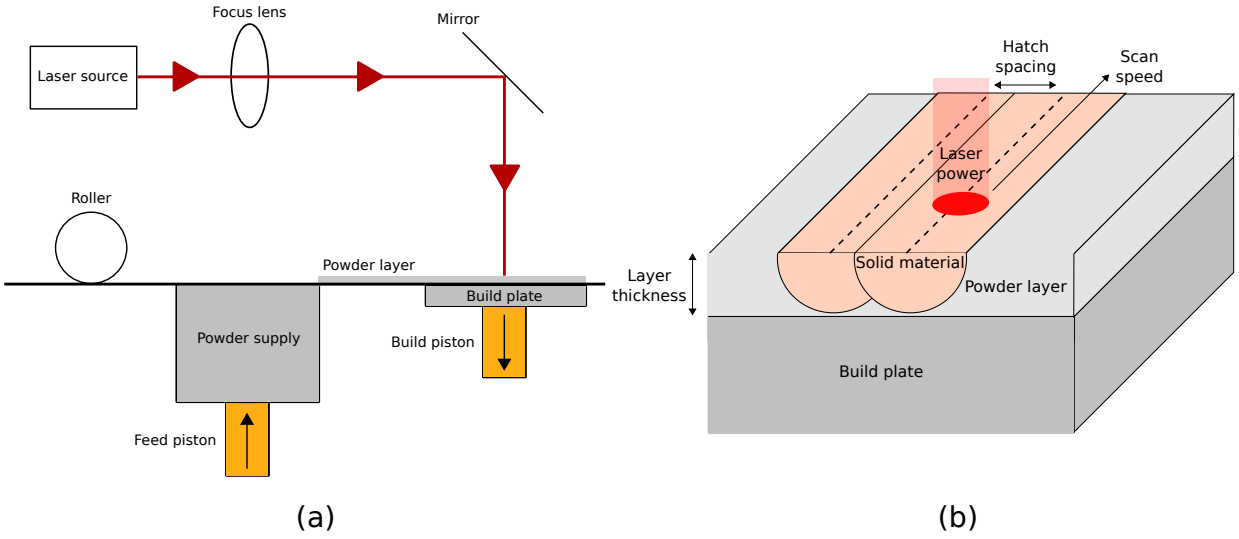


Figure 2.10: (a) Schematic of a LPBF machine. (b) Schematic of the main processing parameters of the LPBF process.

2.4.4 LPBF of NiTi SMAs

Effect of the process parameters

The effect of the different process parameters on the SMA powder has been widely studied in the literature. There are studies focusing on the monotonous change of one of the process parameters. For example, Sequeda *et al.* [138] investigated the effect of laser power on Ni content and microstructure. They found that the higher the laser power, the higher was the Ni evaporation on the NiTi samples. Yang *et al.* [139] studied the evolution of functional properties by changing the scanning speed. They showed that TTs decreased as the scanning speed increased. In addition, they noted an increase in the stress required to induce the martensite transformation when the scanning speed was increased. Shayesteh *et al.* [140] explored the effect of hatch spacing in the microstructure, phase transformation and thermomechanical properties. They found that this parameter significantly impacts the melt pool geometry and consequently the grain size, as it determines the overlap of adjacent melt pools. Furthermore, as the hatch spacing increased, the TTs decreased. Finally, they found an improved PE effect in samples manufactured using the lowest hatch spacing due to the strong texture generated along the build direction. Following the same path, Cao *et al.* [141] observed the effect of hatch spacing on the microstructure and the actuation properties. The researchers found that reducing hatch spacings leads to an increase in TTs. Furthermore, they noted that hatch spacing significantly affects the texture of the samples.

Other studies focused on the monotonic variation of different process parameters. One of the main studies was performed by Ehsan *et al.* [142]. They studied the effect of the laser power and hatch spacing on the microstructure, texture and thermomechanical properties. Their investigation revealed that TTs decrease as the hatch spacing increases. Furthermore, with a specific hatch spacing, higher laser power resulted in higher TTs. The study also indicated that LED significantly influenced the features of the melt pool. They found that higher strain recovery and a more stable PE effect were obtained for lower hatch spacing, regardless of the laser power used. Gan *et al.* [143] explored the effect of the VED on the relative density and actuation properties by changing the laser power and the scan speed. A correlation was identified indicating that an increase in VED was associated with higher TTs. Moreover, they observed a correlation indicating that the stress required to trigger martensite transformation diminishes as the VED increases. Saedi *et al.* [25] observed the effects of the process parameters on the microstructure and the thermomechanical response changing the laser power and scanning speed. They found that higher VEDs increase the TT independently of the process parameter used. In addition, they found that the samples

manufactured with the same VEDs did not result in a similar PE effect. On the other hand, Xue *et al.* [144] focused on the effect of laser power, scan speed and hatch spacing in two different NiTi powders. They observed a trend in the change of the TTs. The higher the VED, the higher the TTs. No trend was found in the different tensile behaviors experienced between the samples. Finally Wang *et al.* [145] studied separately the effect of laser power, scan speed and hatch distance on the phase transformation and tensile properties. They discovered a monotonous change in the martensite transformation with the individual change of each process parameter. In addition, they pointed out that the scan speed was the dominant process parameter in the influence of the Ni/Ti ratio.

All the previous studies of the processing parameters have something in common. They have noted that the TTs are greatly affected by the VED regardless of the process parameter used to change it. This phenomenon is attributed to fluctuations in the Ni/Ti ratio, as Ni has a lower boiling point compared to Ti [146]. As is well known and similar to conventional NiTi alloys, the lower the Ni content, the higher the TTs [86]. Although this trend was observed, no correlations were identified with respect to changes in the thermomechanical properties of the NiTi SMA samples. Some studies have noted variations in the stress required to trigger martensite transformation, while others have examined alterations in the PE effect influenced by process parameters. In addition, no other correlations related to the alterations in the microstructure were found to explain the changes in thermomechanical behavior.

Graded NiTi SMA metamaterials

Regarding the graded NiTi SMA metamaterials, several researchers have successfully manufactured LPBF NiTi heterogeneous samples by using different set of processing parameters for each region of the NiTi samples. One of the most important studies was performed by Nematollahi *et al.* [28]. They manufactured an LPBF NiTi material using two different sets of process parameters. Two VEDs, changing the laser power and the scan speed at the same time, were applied in each half of the sample to achieve different Ni evaporation. Thereby one half of the sample experienced SME behavior and the other half PE behavior at room temperature. In addition, different microstructures were achieved in each half. Other key work on this topic was done by Ma *et al.* [27]. They used LPBF to fabricate a U-shaped sample with different structural responses between sides, altering the hatch spacing and remaining constant the laser power and the scan speed. Due to the different VED used in each side, each half experienced different SME behaviors. In addition, computational simulations were performed to discuss the effect of each set of process parameters on the thermomechanical behavior of

each half of the sample. Wang *et al.* [147] utilized two sets of process parameters to fabricate a functionally graded layered NiTi material with alternating martensitic and austenite phases at room temperature. The NiTi sample exhibited a martensitic transformation temperature range of approximately 130 K and showed excellent damping characteristics. The DSC analysis of the graded NiTi sample revealed TTs that result from the combined influence of each part's manufacturing along with its specific processing parameters. Furthermore, EBSD analysis revealed a distinct microstructure, showing two clearly different regions that are repeated throughout the sample. Finally, Yu *et al.* [57] manufactured functionally graded austenite-martensite-austenite layered NiTi using the principle of rigid-flexible coupling. This method resulted in improved compressive fracture strength and ductility compared to martensitic and austenitic NiTi samples.

The aforementioned studies demonstrate that the thermomechanical features of NiTi alloys can be altered through the chemical composition and microstructural variations induced by LPBF, offering an advantageous method for producing customized metamaterials. However, the effects on the global thermomechanical behavior produced by the fabrication of these complex structures induced by the LPBF process are not yet understood.

NiTi SMA cellular structures

Other key research of NiTi SMAs is done in the area of cellular structures. Yang *et al.* [148] investigated the effect of the metal volume fraction on the compressive behavior of the NiTi giroid structures. The study explored how the volume fraction and unit cell size affected the manufacturing fidelity, discovering that lower volume fractions and smaller unit cells led to more powder adhesion. Mechanical properties were correlated with the volume fraction and unit cell size. These structures exhibited high recoverable strain after deformation. Andani *et al.* [29] designed and fabricated porous lattice structures using Sc, BCC and BCC-Z unit cells. They found that the porosity levels significantly influenced the elasticity and mechanical strength of the structures; increasing porosity resulted in a decrease in stiffness and strength, while maintaining the features of the SME for all lattice structures. All porous samples exhibited an excellent SME, with recoverable strains reaching 5%. Biffi *et al.* [149] studied the microstructural and mechanical properties of a diamond lattice structure. Localized martensite was observed within the node areas of NiTi lattice structures. Furthermore, compression tests indicated that, due to its PE features, the structure was able to recover strains up to 4.5% following a 10% deformation. Residual deformation could be reversed through heating, highlighting the SME. Finally, DSC showed that the lattice samples had

higher martensitic TTs compared to the bulk samples manufactured using the same process parameters. Finally, Khademzadeh *et al.* [150] design and manufactured lattice structures imitating trabecular bone were designed with pore sizes of 380 µm and 580 µm using two different sets of processing parameters. The analysis of images after manufacturing identified variations from the intended pore dimensions, highlighting the necessity for precise production. It was discovered that the discrepancies between the as-built components and their nominal design were predominantly positive. This indicates that the constructed holes are smaller than the specified measurements. Post-process heat treatments, such as solution annealing and aging, enhanced the microstructure and optimized phase transformation behavior. This enhancement increased the potential for PE.

The combination of SMA capabilities and the design freedom of lattice structures paves the way for a new era of SMA-based devices. However, as observed in previous studies, only a limited number of fundamental investigations have been conducted on NiTi SMA cellular structures. To fully exploit the potential of this combination, significant advancements remain necessary.

2.5 Applications of NiTi alloys

The interesting features of SMAs such as PE, SME, or their TWSME make them ideal for a wide range of applications. NiTi devices are used in biomedical and engineering applications, such as aerospace [151], electromechanical systems [152] or actuators [86]. More details are found in the following sections:

2.5.1 Aerospace applications

The incorporation of SMA technology within the aerospace sector included applications in fixed-wing aircraft, rotorcraft, and spacecraft. Notable fixed-wing initiatives include the Smart Wing program and the Smart Aircraft and Marine Propulsion System Demonstration (SAMPSON) [151]. The Smart Wing effort tried to utilize active materials like SMAs to enhance the performance of lifting bodies [153]. SMAs were employed as wire tendons to actuate hingeless ailerons and fashioned into torque tubes that enabled spanwise wing twisting on a scale model of the F-18 aircraft. Although SMAs provided sufficient actuation capabilities, the torque tube was found to be inadequate to actuate in a full-scale wing.

The SMA tendons developed in the project are similarly applied to control jet engine nozzles

during take-off and landing. The high exhaust temperatures during these phases promote the austenite phase in the SMA tendons, inducing a recovery strain that opens the nozzles. Conversely, at high altitudes, lower temperatures trigger a martensitic phase transition, leading to nozzle closure and enhancing flight propulsion [60]. The same mechanisms for nozzle movement are utilized to minimize noise during take-off and landing. This is done by leveraging the actuation capabilities of SMAs, such as NiTi, to move chevrons in and out to control noise levels during these phases [154]. Additionally, SMAs are applied to adjust the wing structures of aircraft [155]. SMAs like NiTi are integrated into aircraft wings to alter the airfoil shape from symmetric to optimize performance at specific altitudes [156].

Several other efforts have been made to integrate SMA elements into aerospace systems. One of these studies focused on the development of an airfoil variable geometry which effectively changed its configuration from symmetric to chambered through the SMA actuation response [157]. Other studies have focused on smaller elements. For example, examining the feasibility of utilizing SMAs alongside Micro-Electromechanical Systems (MEMS) to mitigate the turbulent drag on aerodynamic surfaces [158]. When activated, the MEMS skin could generate a traveling wave that energizes the boundary layer, thereby reducing the turbulent drag. Research has also focused on optimizing the dynamic properties of aircraft structural panels through SMA elements, facilitating variable elastic stiffness via martensitic transformation. Pre-straining or increasing the SMA fiber volume fraction was found to reduce thermally induced post-buckling deflection in structures [159].

The application of SMAs in rotorcraft has predominantly focused on the main rotor [160]. Blade-twist actuation represents a key area of ongoing research [161]. The substantial actuation energy provided by SMAs is particularly beneficial due to the significant forces necessary within the confined space of the rotor blade. Additionally, SMAs find use in rotorcraft for collective control via SMA wire components [162] and for introducing anhedral to the rotor blade tips. This design adjustment helps reduce noise from blade vortex interactions by redirecting the blade tip vortex away from the rotor plane [163].

In terms of spacecraft applications, SMAs serve to actuate various components, such as using torsion to move solar panels [160]. SMAs also find use as vibration isolators and dampers [164]. Their transition from the initial elastic phase to the transformation phase effectively isolates vibrations. Furthermore, the hysteresis characteristic of the pseudoelastic (PE) behavior reflects the mechanical energy that an SMA can dissipate. Additionally, the gradual heating-induced slow actuation makes SMAs ideal for low-impact release mechanisms in space contexts. The adaptability of SMA actuator designs also facilitates the creation of smaller release devices for satellites that require compact mechanisms [165].

2.5.2 Biomedical applications

The interesting features of the SMAs coupled with the biocompatibility of NiTi make them ideal candidates for biomedical applications. Studies on the biocompatibility and biofunctionality of NiTi alloys have demonstrated promising results, indicating their correct behavior for use in the human body [166, 167].

Orthodontic NiTinol arches have been used since the 1970s [61]. The main advantage of NiTi over stainless steel lies in the PE behavior of NiTi arch wires. These wires can operate within the PE plateau, where the material exhibits minimal stress variation over a significant strain range. In contrast, stainless steel archwires experience a substantial increase in stress in the same range.

The initial vascular application of shape memory alloys SMA was the venous "Simon filter," designed to prevent embolism in patients who cannot take anticoagulants. The device functions as a filter by capturing blood clots within the flow. Its insertion is enabled by the SME [168]. This device is manufactured in an open state using a NiTi alloy with an A_f temperature matching that of the human body, ensuring a martensitic phase at ambient temperature. Consequently, when the device is crimped inside the catheter, there is residual deformation due to the martensitic transformation from multivariant to single-variant state, facilitating the closure and insertion into the catheter. A saline solution circulates through the catheter to maintain a low temperature during insertion into the body. Once correctly positioned, the filter is deployed, the flow of saline is stopped, and body heat triggers the martensite-to-austenite transformation, allowing the device to return to its original configuration.

NiTi alloys are also employed in various applications of self-expanding vascular stents. These stents consist of metallic mesh that can open a narrowed vessel, thereby restoring blood flow to the peripheral tissues [169]. Self-expanding stents are used to treat atherosclerotic lesions in the coronary, carotid, and peripheral arteries, including the iliac and femoral arteries [170].

Devices developed for orthopedic purposes are implemented to stabilize injured or fractured bones. NiTi rods are additionally employed in devices to rectify scoliosis [171], utilizing constrained recovery to adjust vertebral positions. In orthopedic therapies, the characteristics of SMAs are used during physiotherapy for partially atrophied muscles [172]. Moreover, the PE effect is incorporated in the manufacturing of NiTi intramedullary nails [173]. As outlined in a patent [174], the TWSME is leveraged for both inserting and extracting the intramedullary nail from lengthwise fractured bones.

The field of medicine continues to improve the application of minimally invasive surgery

(MIS). Technologies that facilitate MIS include tools designed to be inserted through small openings, subsequently expanding to an appropriate size for specific functions. PE guide wires are extensively utilized in surgical procedures for their resistance to twisting and exceptional flexibility [175].

2.5.3 Other applications

PE hysteresis serves as a potent mechanism for vibration and impact energy dissipation. This attribute has been implemented in military armored vehicles [176] as well as in commercial devices [177]. Additionally, an SMA actuation system forms part of the Shinkansen bullet train's gearbox, in which the gearbox temperature is monitored, and an SMA spring activates a valve to modulate the oil level [178]. The SME is similarly employed in shower faucet configurations where an SMA spring adjusts the hot and cold water flow automatically to sustain a predetermined temperature [179].

Chapter 3

Process optimization on additively manufactured NiTi SMA

3.1 Introduction

In recent years, LPBF of NiTi alloys has become more popular, being one of the most interesting techniques due to the better dimensional accuracy [180] and surface finish that provides [181]. Numerous studies have been dedicated to explore the possibilities of NiTi additive manufacturing [51, 52, 56, 182, 54, 183, 128, 184, 185, 186, 53]. Most studies have focused on achieving high relative densities in printed NiTi parts by optimizing AM processing parameters [51, 52, 56, 182, 54]. Several studies have noted that the TTs are greatly affected by the input energy density [56, 187]. Further research shows that this phenomenon is attributed to fluctuations in the Ni/Ti ratio, as Ni has a lower boiling point compared to Ti [146]. Other studies have linked the variation in TTs to the presence of dislocations, precipitates, or internal stresses [27, 188, 189, 190]. Concurrently, other studies have investigated the impact of post-processing heat treatments such as solution treatment, annealing, or aging [183, 128, 184], as well as the influence of various scanning strategies on the resultant material properties [185, 186, 53]. Moreover, other works have focused on the effect of process and orientation conditions on thermomechanical and transformation behavior [191, 192, 193].

Despite these efforts, one of the biggest remaining challenges in LPBF of NiTi alloys is establishing the correlations between the main processing parameters (i.e., laser power, scanning speed, and hatch spacing), the microstructure, the phase transformation behavior, and the thermomechanical properties.

The first step in trying to establish these correlations is to define a process parameter window. Similar to additive manufacturing conventional alloys, NiTi parts produced using AM are prone to produce microdefects such as balling, keyholing, and lack of fusion, as well as macroscopic defects such as delamination, cracks, and warping [132]. Consequently, a careful selection of processing parameters is therefore required to be able to circumvent these defects and fabricate quality parts while at the same time meeting the application requirements in terms of thermomechanical properties.

The present chapter describes the experimental procedures that were carried out to establish a processing parameter window and a phase transformation analysis for the LPBF NiTi samples. The development of this process window is a critical step, as it defines the combination of laser power, scan speed, hatch spacing, and layer thickness required to produce high-quality parts with minimal defects. Two different approaches are used. A conventional approach based on a broad study of defect quantification and an alternative systematic approach. The first one uses a more traditional methodology in which samples are printed to study the porosity using different combinations of process parameters. The samples with the lowest porosity results were then subjected to a phase transformation analysis. The systematic approach is based on the change of each process parameter independently while the others remain constant. In this approach, phase transformation analysis was performed on all samples. This chapter is part of our published work [194].

3.2 Methodology

3.2.1 Design of experiments

In this study, NiTi powder (Ni 55.86 wt.%), which was produced by an electrode induction-melting gas atomization (EIGA) process by Carpenter Additive was used. The particle size of the powder ranges from 18 to 52.7 µm (d_{50} = 32.9 µm). The chemical composition of the powder provided by Carpenter Additive is shown in Table 3.1. The NiTi powder's TTs supplied by the provider were an austenite transformation initiation temperature (A_s) of 332 K and an austenite transformation finishing temperature (A_f) of 348 K.

NiTi samples were fabricated using LPBF in an Aconity Mini (Aconity GmbG, Germany) equipped with a 400 W infrared laser. The LPBF process was performed under a protective argon atmosphere. To do this, the build chamber was flooded with argon gas with an in flow rate of 3 L/min achieving an average oxygen concentration below 150 ppm. A stripe

Element	wt.%
Titanium	Balance
Nickel	55.86
Iron	0.0067
Carbon	0.0026
Oxygen	0.043
Nitrogen	$\leq$ 0.0005
Chromium	0.0026
Cobalt	0.0008
Copper	0.0015
Hydrogen	0.0005

Table 3.1: Chemical composition of the NiTi powder used in this work.

hatch-contour scan strategy was used for each layer, with a 67° rotation between layers. All the samples in the study were printed perpendicular to the baseplate. All the prints were fabricated on a titanium build plate, by using a Gaussian laser beam with a spot size of 80 µm and a constant layer thickness of 30 µm.

To study the effect of the processing parameters on the porosity and the transformation behavior two different approaches were used:

- **Broad approach:** In the broad approach, different laser powers (65-228 W), scanning speeds (556-1650 mm/s) and hatch spacings (28-145 µm) were used. The combinations of process parameters were selected to print samples with three different VEDs (70, 80 and 90 J/mm^3). The set of process parameters used are detailed in Figure 3.1. For further details, all the combinations of process parameters used are detailed in the annexes. The porosity of all of the samples will be studied and only the ones with lower porosity levels will be used for the phase transformation analysis. All VEDs were calculated as follows in Equation (2.2).

- **Systematic approach:** In the systematic approach different laser powers (72-185 W), scanning speeds (668-1739 mm/s) and hatch spacings (28-85 µm) were also used. The choice of parameters was made to obtain volumetric energy densities (VEDs) between 50 and 150 J/mm^3 since in the literature different values within this range have been used to obtain samples without porosity [143, 195, 145, 21, 25]. The study involved varying one of the processing parameters while keeping the other two constant, starting from a central reference parameter set, which is referred to as the anchor point. The set of parameters employed are detailed can be observed in Figure 3.2. In this approach, phase transformation analysis will be performed in all samples independently of the

results of the porosity analysis.

As can be observed, the broad approach studied the porosity maps in a deeper way using a total of 80 samples, while the systematic approach only uses a smaller group of 15 samples. Square samples with a section of 1x1 mm^2 and 10 mm of height were produced to characterize the relative density. Furthermore, in order to study the transformation temperatures, cylindrical samples with a diameter of 1.4 mm and a height of 4 mm were printed and sliced into thin cylindrical sections of thickness 0.7 mm, using electrical discharge machining (EDM) (see Figure 3.3).

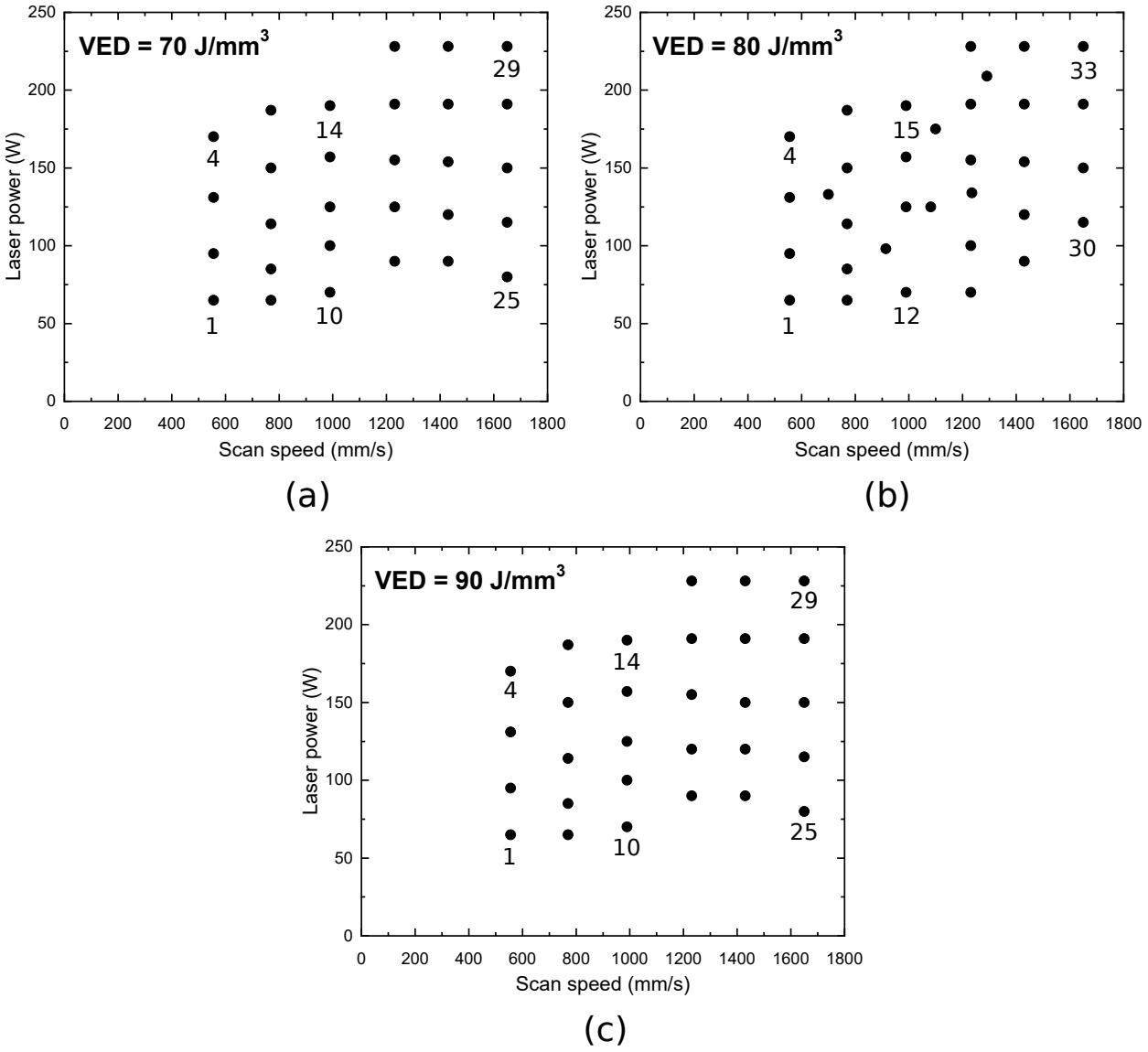


Figure 3.1: Combinations of process parameters selected in the broad approach to perform the porosity analysis for (a) 70 J/mm^3, (b) 80 J/mm^3 and (c) 90 J/mm^3. More information about the process parameters can be found in the Annex.

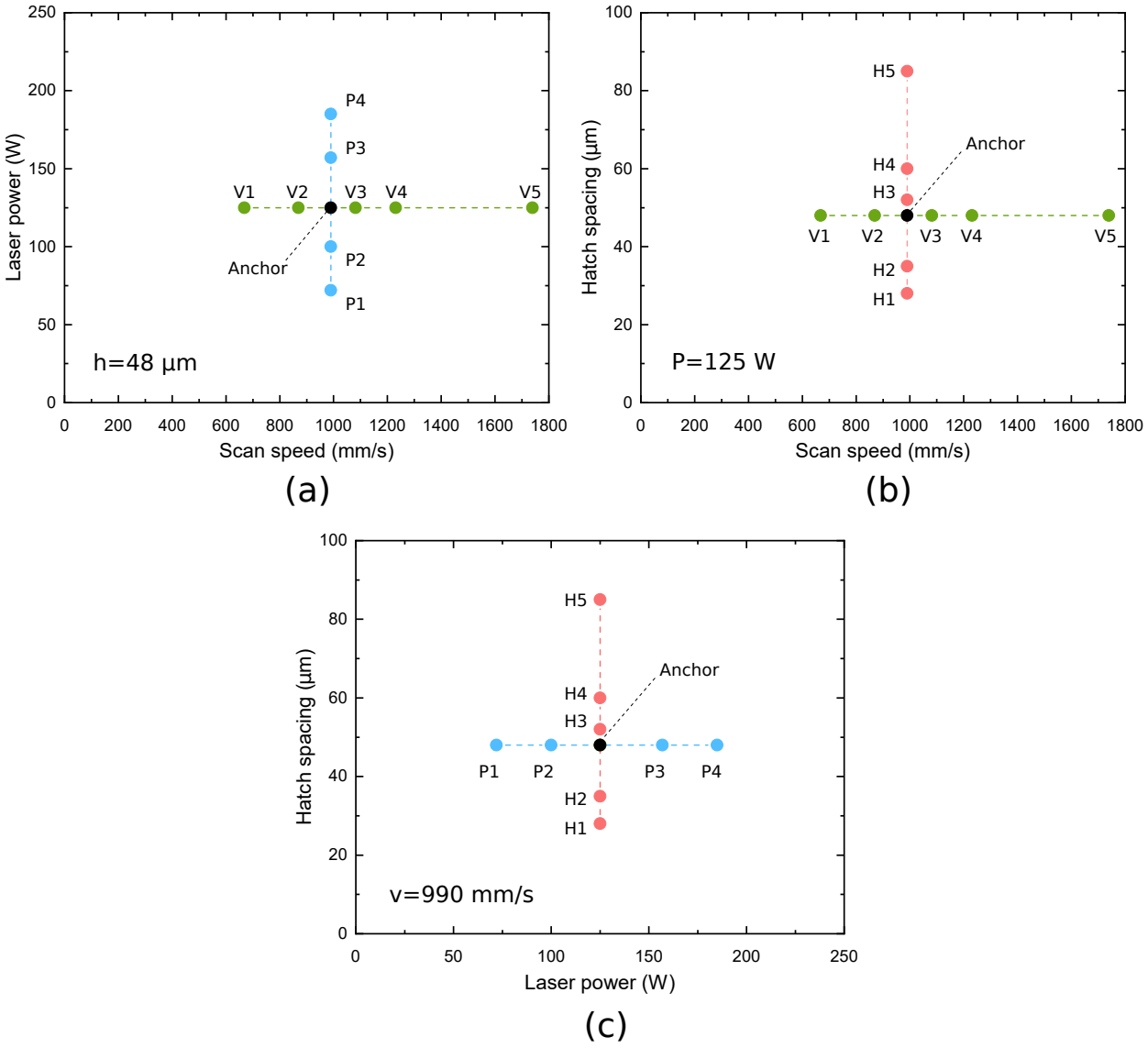


Figure 3.2: Combinations of process parameters selected in the systematic approach to perform the porosity and phase transformation analysis. The anchor point is represented in black. P (in blue) refers to the samples fabricated with different laser powers, V (in green) to the ones manufactured with variations in scanning speed, and H (in red) to the ones with variations in hatch spacing. More information about the process parameters can be found in the Annex.

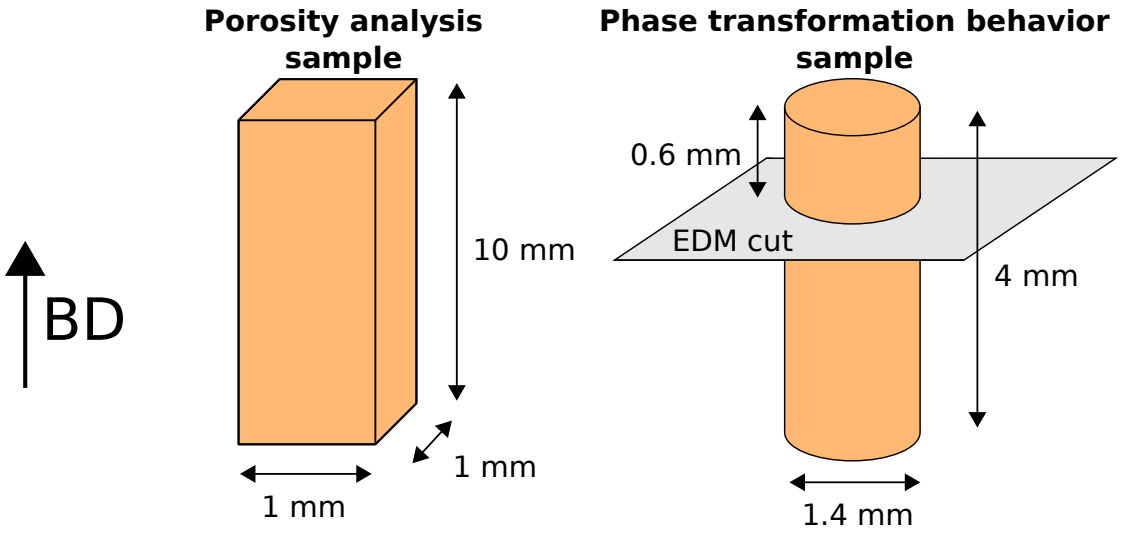


Figure 3.3: Geometries of the samples manufactured to perform the porosity and phase transformation analysis.

3.2.2 Material characterization

Porosity analysis

An Olympus GX53 optical microscope was employed to examine the porosity. In order to perform the analysis, the specimens were mounted in epoxy. The metallographic preparation of the samples involved an initial grinding step using up to 1200-grit abrasive paper, followed by a polishing stage involving 9 µm and 3 µm diamond suspension. A final step with colloidal silica suspension was carried out. For the porosity quantification, in order to detect the pores in each image, a Sauvola filter was applied.

Phase transformation temperatures characterization

The phase transformation behavior was characterized by using Differential Scanning Calorimetry (DSC) in a Q2000 DSC (TA INSTRUMENTS) to determine the NiTi TTs as a function of the processing parameters. DSC was performed under a flowing nitrogen atmosphere and with a constant heating/cooling rate of 10 K/min following ASTM-F2004, except for the fact that the samples were kept in as built condition to address the influence of the building parameters. The TTs were calculated using the tangent method (see Figure 3.4).

Composition analysis

Energy Dispersive X-Ray (EDS) was used to analyze the chemical composition present in the polished samples as a function of their processing parameters. The atomic nickel percentages (Ni at.%) present on each sample were quantified. Three measurements were extracted at different locations in each sample.

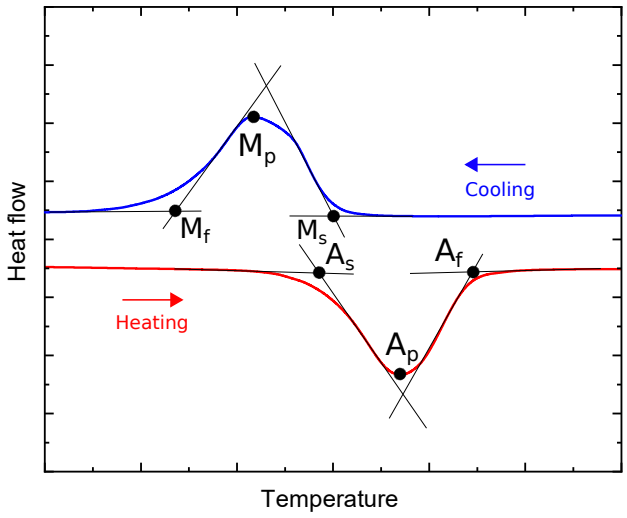


Figure 3.4: Example of how TTs variables are extracted from Differential Scanning Calorimetry (DSC).

3.3 Results

3.3.1 Porosity analysis

Figures 3.5a-c present the porosity maps corresponding to VEDs of 70, 80 and 90 J/mm^3, extracted from the porosity measurements of the samples from the broad approach. In all three cases, a similar trend is observed. A process window exists within the range of laser powers between 75–200 W and scan speeds of 500–1600 mm/s, where defect-free NiTi parts can be achieved. In particular, regions with high laser power (>130 W) and low scan speed (<800 mm/s) exhibit porosity levels exceeding 1%. Similarly, high porosity levels (>1%) are observed in regions with low laser power (<100 W) and high scan speed (>1000 mm/s).

Figure 3.6 illustrates the LPBF NiTi cubes that exhibited porosity levels below 0.2%. Samples that met this criterion were classified as defect-free and subsequently selected for transformation temperature analysis using DSC.

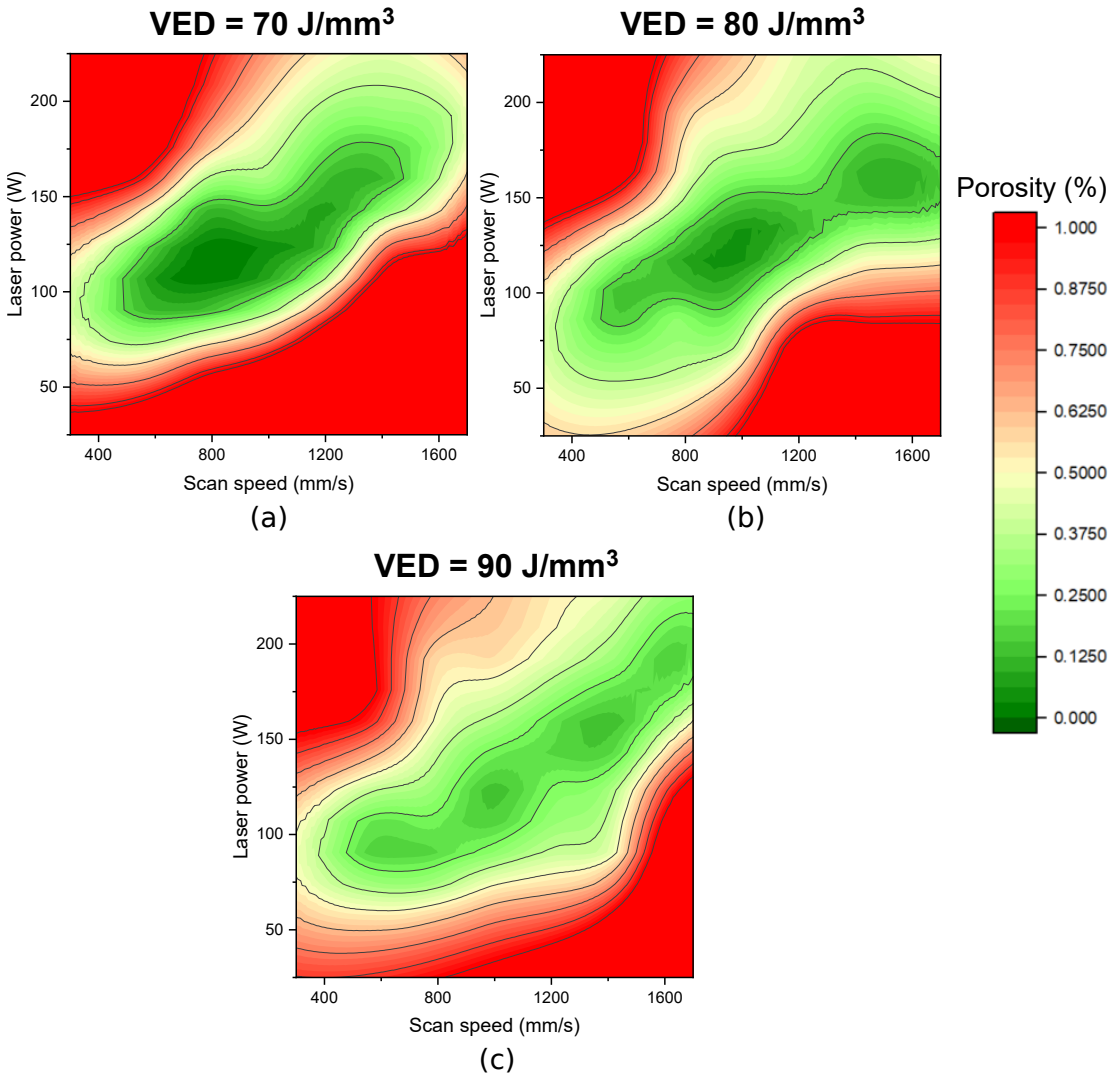


Figure 3.5: Porosity maps of the LPBF NiTi cubes for VEDs of (a) 70 J/mm^3, (b) 80 J/mm^3 and (c) 90 J/mm^3 used in the broad approach.

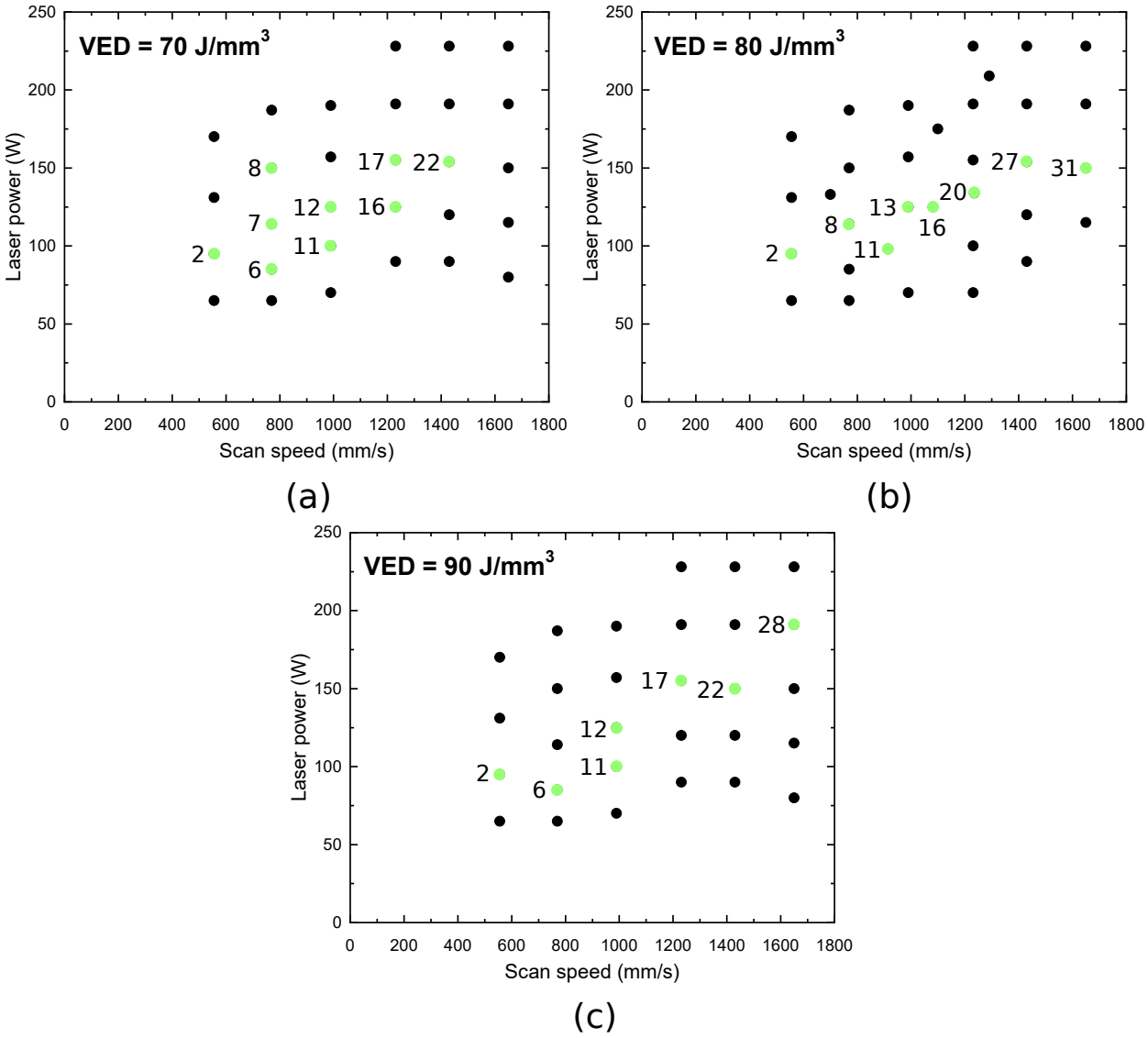


Figure 3.6: LPBF samples with porosity levels below 0.2 % in the broad approach.

Table 3.2 presents the results of the porosity analysis of the LBPF NiTi samples from the second experimental approach. The data indicate that porosity levels remain low for most samples, except for sample P4, which was fabricated using the highest laser power (185 W), and sample V1, produced with the lowest scanning speed (668 mm/s).

Sample	**Porosity (%)**	**LED (J/mm)**	**VED (J/mm^3)**
Anchor	0.12	0.126	90
P1	0.14	0.073	50
P2	0.15	0.101	70
P3	0.13	0.159	110
P4	0.46	0.187	130
V1	0.45	0.187	130
V2	0.11	0.144	100
V3	0.10	0.116	80
V4	0.09	0.102	70
V5	0.07	0.072	50
H1	0.07	0.126	150
H2	0.06	0.126	120
H3	0.08	0.126	80
H4	0.14	0.126	70
H5	0.09	0.126	50

Table 3.2: Average porosity (in percentage) for LPBF NiTi samples from the systematic approach and the values of LED and VED for each set of process parameters according to equations 2.1 and 2.2 respectively.

3.3.2 Phase transformation analysis

Figure 3.7a-c presents the DSC results for samples with porosity levels below 0.2 % (see Figure 3.6) fabricated using VEDs of 70, 80, and 90 J/mm^3 from the samples from the broad approach. DSC curves show two different phase transformations of NiTi, which involve the exchange of latent heat. During heating, endothermic peaks are observed, corresponding to heat absorption as the alloy undergoes the phase transformation from martensite to austenite. This endothermic process indicates the latent heat necessary for the rearrangement of the crystal structure. In contrast, during cooling, exothermic peaks indicate the release of heat associated with the reverse phase transformation from austenite to martensite. This exothermic reaction displays the release of the latent heat absorbed during the forward transformation, as the martensite phase is thermodynamically more stable at lower temperatures. It is clear that different processing parameters can result in similar TTs, though with slight variations in their transformation behavior. This indicates that TTs are not determined solely by the

volume energy density; instead, they can depend on other factors influenced by the combined effects of laser power, hatch spacing, and scan speed. No evidence of R-phase is observed. All TTs calculated from these curves are shown in the Annex.

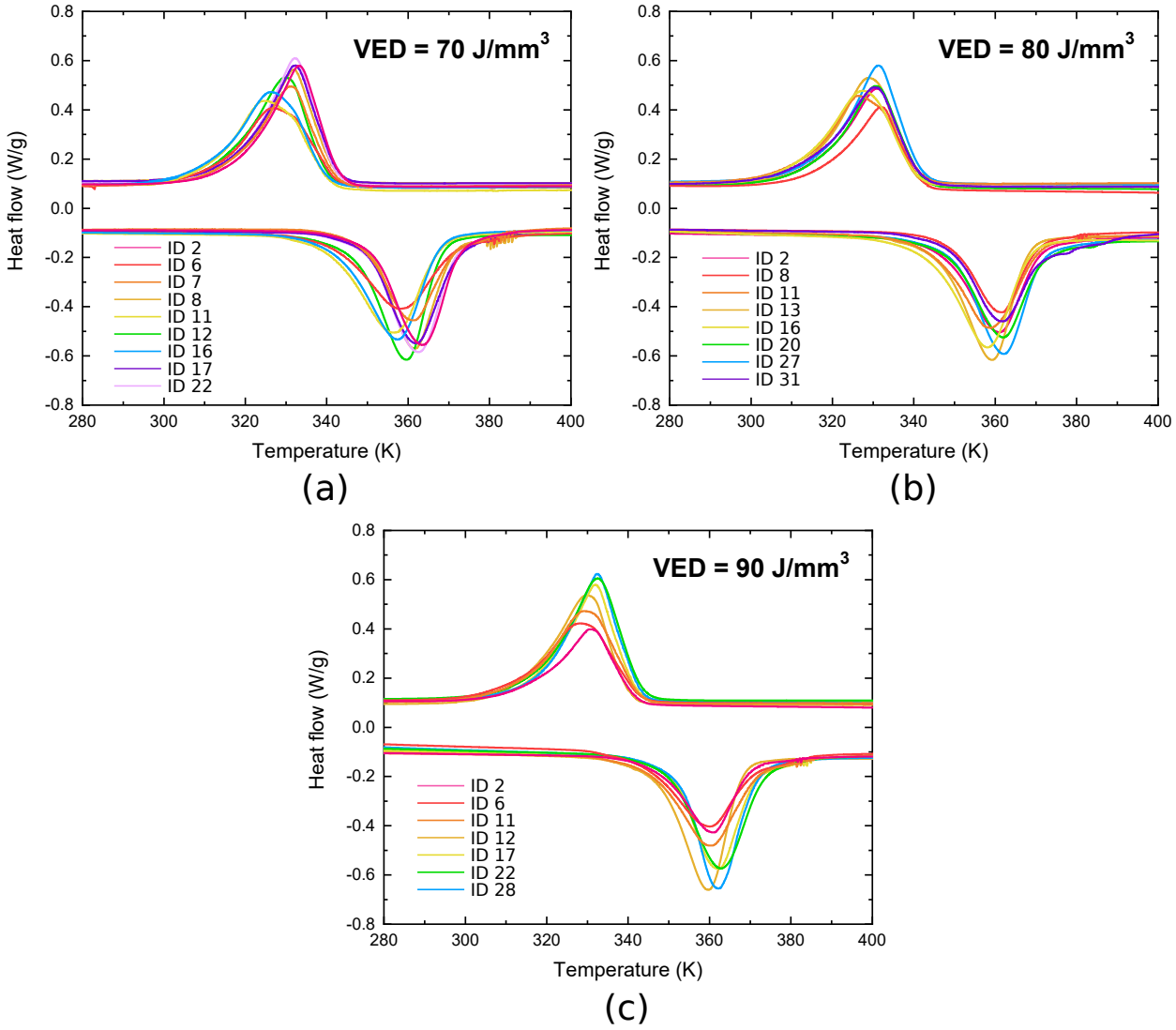


Figure 3.7: DSC curves of the defect-free LPBF NiTi samples for VEDs of (a) 70 J/mm^3, (b) 80 J/mm^3 and (c) 90 J/mm^3 used in the broad approach.

The influence of each processing parameter on the TTs of LPBF NiTi samples was investigated using the samples of the systematic approach. Figure 3.8 presents the DSC curves and TTs corresponding to variations in laser power (P), scanning speed (v), and hatch spacing (h), respectively. The numerical values of the TTs extracted from DSCs are shown in Table 8 using the tangent method as it was indicated in Figure 3.4. Notably, no peaks associated with R-phase formation have been observed in any case.

In Figures 3.8a and 3.8b, the peaks of the TTs shift towards higher temperature values with the escalation of laser power from 72 to 185 W in a monotonic fashion (scanning speed = 990 mm/s and hatch spacing = 48 µm). Conversely, in Figures 3.8c and 3.8d, an increase in scanning speed from 668 to 1739 mm/s (laser power = 125 W and hatch spacing = 48 µm) leads to a decline in the TTs until 1200 mm/s, beyond which the TTs stabilize with the scanning speed. Figures 3.8e and 3.8f depict how increasing the hatch spacing from 28 to 85 µm (laser power = 125 W and scan speed = 990 mm/s) results in a decrease in the TTs. Beyond 50 μm, the TTs remain constant with the hatch spacing. Based on these results, the following effect of the processing parameters on the TTs can be noted: a higher laser power (P4), a lower scan speed (V1) and lower hatch spacing (H1), which result in high VEDs, lead to a raise of the TTs.

3.4 Discussion

3.4.1 Effect of the process parameters on the manufactured structure

As demonstrated by the results (see Figure 3.5), porosity is used as a reliable criterion to define the optimal process window to print LPBF NiTi samples. However, a detailed examination of the printed samples provides a deeper understanding of the underlying mechanisms influencing the LPBF process. For this study, samples with VEDs of 70, 80, and 90 J/mm^3 were printed by varying the laser power, scan speed, and hatch spacing to achieve the desired VED in the broad approach. For the same VED, a wide range of porosity levels is reached. The result suggests that VED may not be a good indicator for porosity level of the LPBF NiTi samples.

Figure 3.9 illustrates the porosity levels of the samples fabricated in the broad approach and their corresponding LED values. The LED was calculated according to Equation (2.1). It can be observed that a consistent trend is followed across the various printed VEDs. Samples produced at low LED levels (<0.09 J/mm) exhibit porosity levels exceeding the threshold established for defect-free samples (0.2%), as defined in this study. Similarly, samples manufactured at high LED levels (>0.21 J/mm) also fall outside these limits. Samples processed with LEDs in the range of 0.1–0.2 J/mm achieve porosity levels below 0.2%, although some exceed this threshold.

Figures 3.10 a-b present the porosity levels of the samples analyzed in the systematic approach, together with their corresponding LED and VED values. As shown in Figure 3.10a, samples

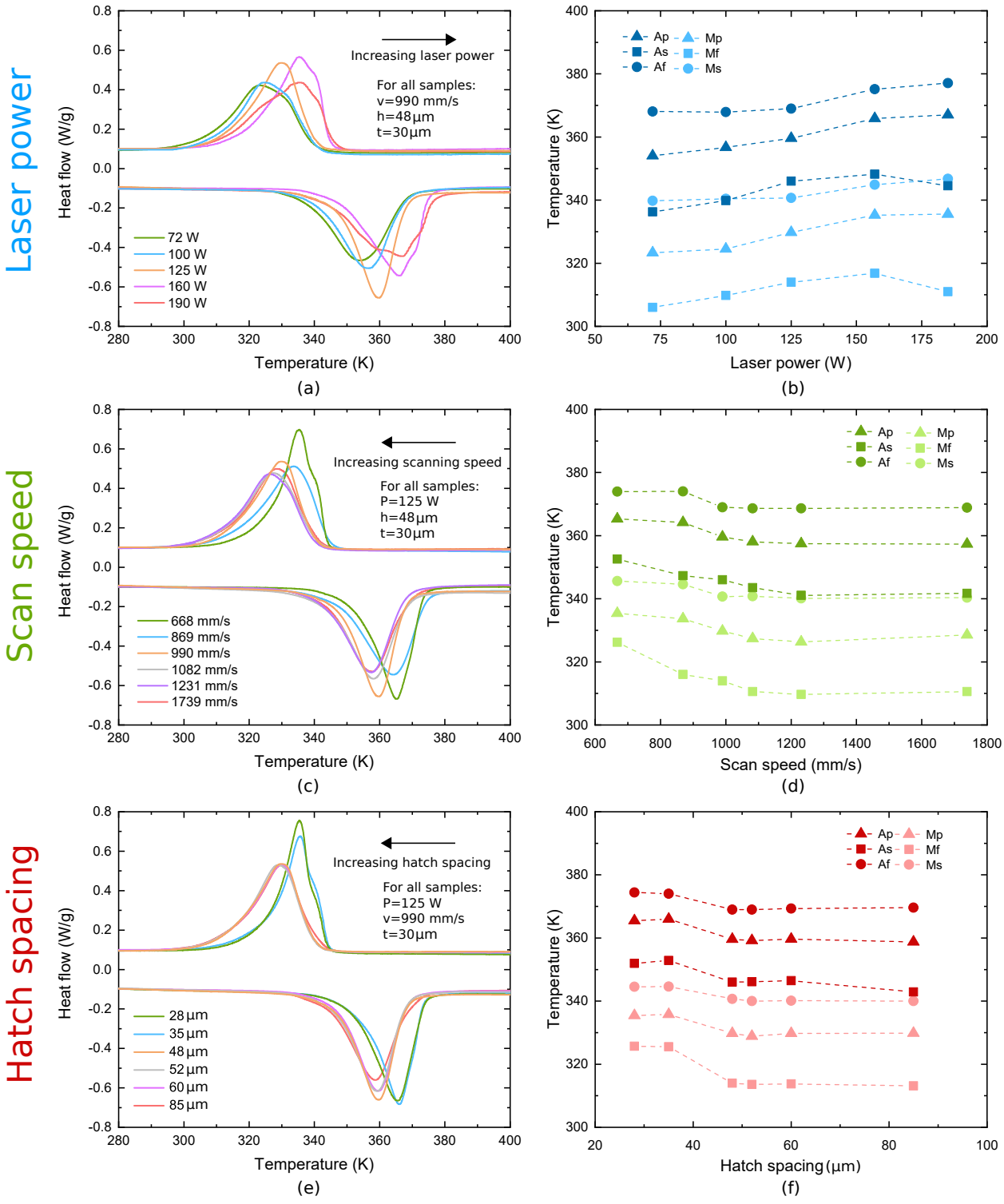


Figure 3.8: (a,c,e) Differential Scanning Calorimetry (DSC) results, and (b,d,f) variation of the martensite transformation start temperature (M_s), the martensite transformation finish temperature (M_f), the peak of the martensite transformation (M_p), the austenite start transformation temperature (A_s), the austenite finish transformation temperature (A_f) and the peak of the austenite transformation (A_p), for (a-b) samples P1-P4, (c-d) samples V1-V5 and (e-f) samples H1-H5. More information about the calculated TTs can be found in the Annex.

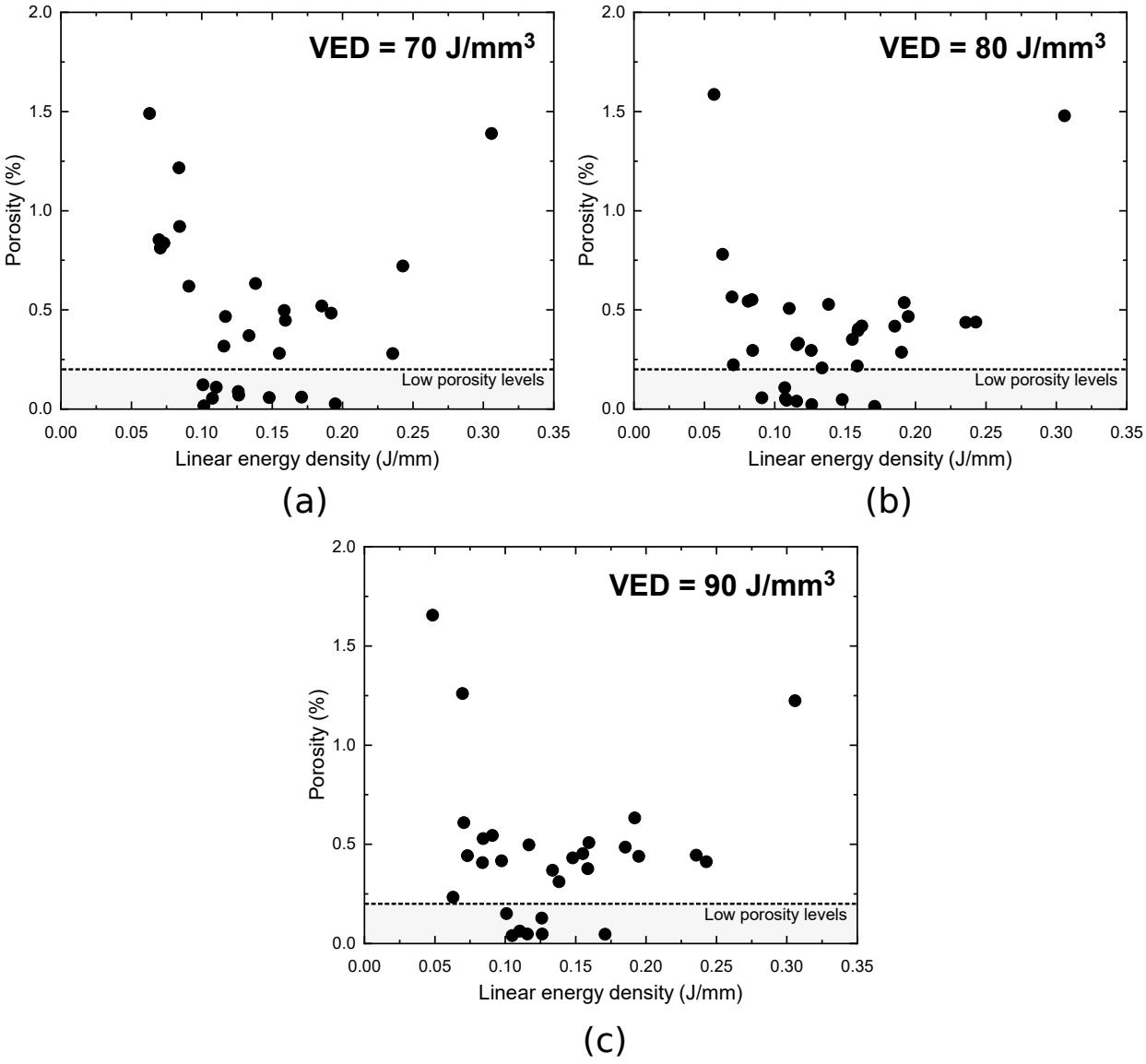


Figure 3.9: Porosity levels of the samples used in the broad approach and their LED for samples manufactured using VEDs of (a) 70 J/mm^3, (b) 80 J/mm^3 and (c) 90 J/mm^3.

printed with LEDs below 0.16 J/mm exhibit porosity levels under 0.2%. A notable increase in porosity is observed for the parameters P4 (highest laser power) and V1 (lowest scanning speed), which correspond to the highest LED values, while the remaining parameters demonstrate low porosity levels without observable trend. As depicted in Figure 3.10b, and consistent with the observations of the broad approach, the printed VED does not reliably represent the expected porosity levels. This is in agreement with previous work, in which LED has been observed to directly correlate with the porosity of AM samples [196]. As LED increases, porosity levels also increase, reaching high porosity levels above 0.25 - 0.3 J/mm [196].

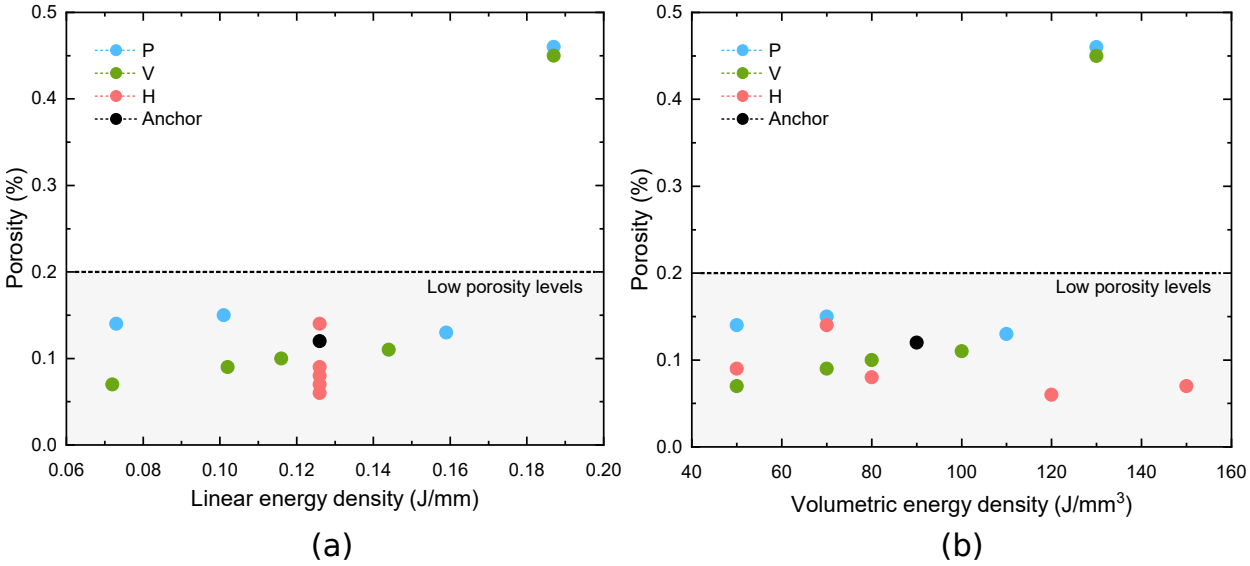


Figure 3.10: Porosity levels of the samples manufactured in the systematic approach as function of (a) LED and (b) VED. The anchor point is represented in black. P (in blue) refers to the samples fabricated with different laser powers, V (in green) to the ones manufactured with variations in scanning speed, and H (in red) to the ones with variations in hatch spacing.

This meant that the VED was not the only factor that determined the forming quality of LPBF NiTi. Other studies also suggest that LED is a more reliable method to stabilize porosity levels in LPBF samples [197]. In the systematic approach (see Figure 3.10) the trend with the LED is clear modifying each process parameter only. In contrast, in the broad approach (see Figure 3.9), there is a trend, but there are samples in the conductive zone that are outside the limits of the low porosity levels considered. This means that using the LED a broad approach about the printability can be obtained but more complex effects between process parameters are happening.

3.4.2 Effect on the process parameters on the phase transformation

Figure 3.11 displays the TTs obtained from the DSCs test from the broad approach (see Figure 3.7). TTs have been grouped by printed VED. It can be observed that similar results are obtained regardless of the VEDs. This means that independently of the different sets of process parameters used to manufacture, TTs of defect-free NiTi samples will remain similar.

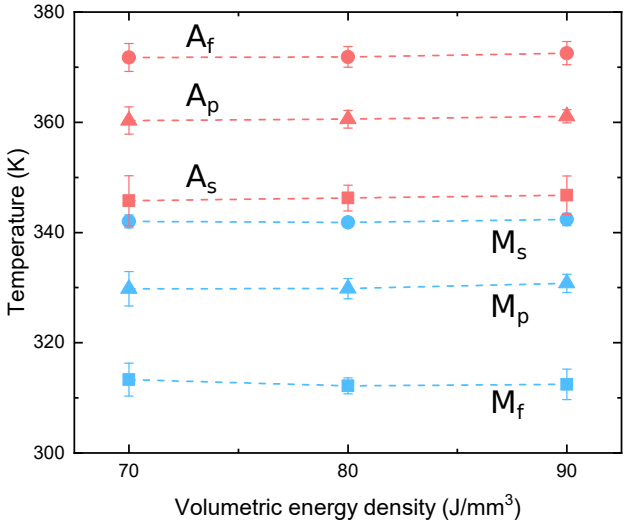


Figure 3.11: Average TTs and their respective error bars obtained from the analysis of the DSC curves in Figure 3.7 showing the martensite transformation start temperature (M_s), the martensite transformation finish temperature (M_f), the peak of the martensite transformation (M_p), the austenite start transformation temperature (A_s), the austenite finish transformation temperature (A_f) and the peak of the austenite transformation (A_p). More information about the calculated TTs can be found in the Annex.

On the other hand, during the DSCs from the systematic approach, interesting trends are observed changing each process parameter while the other two remain constant. During the LPBF process, some chemical elements with higher partial pressure evaporate more readily from the melt pools [198]. To elucidate the effect of the temperature on nickel and titanium evaporation, the partial pressure of both elements has been calculated following the equations presented in the work of Alcock *et al.* [199]. The results are presented in Figure 3.12a. As the temperature increases to the typical values reached in the AM process, the partial pressure of nickel increases more rapidly than for titanium, and therefore nickel becomes more volatile. This preferential Ni evaporation leads to a change in the overall Ni/Ti ratio.

To study the change in nickel content under the different process parameters used in the systematic approach, EDS compositional analysis of the manufactured samples was conducted. Figure 3.12b shows the average atomic percentage of nickel for each LPBF condition as a

function of the VED for the different LPBF variables under study (laser power P, scanning speed V and hatch spacing H). The results show that samples printed with lower VEDs – resulting from low laser power (P1), high scanning speed (V5) and large hatch spacing (H5) – present a higher nickel content ($\sim$ 1.9-2.0%) compared to those fabricated with higher VEDs – resulting from high laser power (P4), low scanning speed (V1), and small hatch spacing (H1). This data reveals a consistent trend: an increase in VED results in greater Ni evaporation. Furthermore, no relevant differences were found in the values of Ni evaporation for different VEDs with the selected processing parameters (e.g., laser power, scan speed, or hatch spacing) for the same VED. Examining the initial composition of the powders (see Table 3.1), the initial nickel content is about 50.8 at.% and, after printing, the nickel content decreases to values lower than 48.5 at.% (see Figure 3.12b).

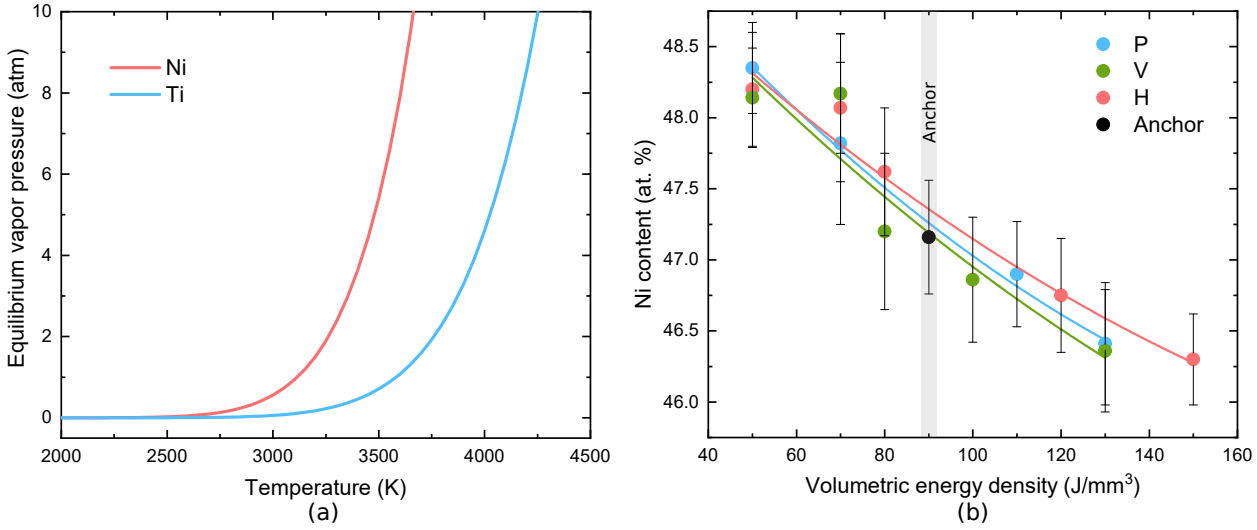


Figure 3.12: (a) Equilibrium vapor pressures of Ni (red) and Ti (blue) calculated according to the equations presented in [199]. (b) Atomic nickel (Ni) content (%) present in the LPBF manufactured samples as a function of the VED. The anchor point is represented in black. P (in blue) refers to the samples fabricated with different laser powers, V (in green) to the ones manufactured with variations in scanning speed, and H (in red) to the ones with variations in hatch spacing. In general, the Ni content reduces with increased VED due to higher Ni evaporation.

As reported in other studies, the composition of NiTi alloys significantly affects TTs [200, 20, 201]. Some studies have reported that TTs decrease by 20-40 K with just a 0.1 at.% increase in nickel content for Ni-rich alloys [86]. As a result, the lower Ni/Ti ratio found in samples with higher VEDs (see Figure 3.12b) can lead to an increase in TT [86]. This is confirmed in the results presented previously in Figure 3.7, which shows the significance of varying each process parameter. To further elucidate the comparison effect of each processing parameter on the TTs, the austenite and martensite peak TTs in Figure 3.7 (A_p and M_p) have been

plotted as a function of the VED in Figure 3.13 for samples fabricated by changing laser power, scan speed and hatch spacing. The same trend inferred from Figure 3.8 is observed here – the TTs peaks for austenite and martensite increase as the VED increases. Notably, a shift in transformation behavior is evident within the range of 75 to 110 J/mm^3.

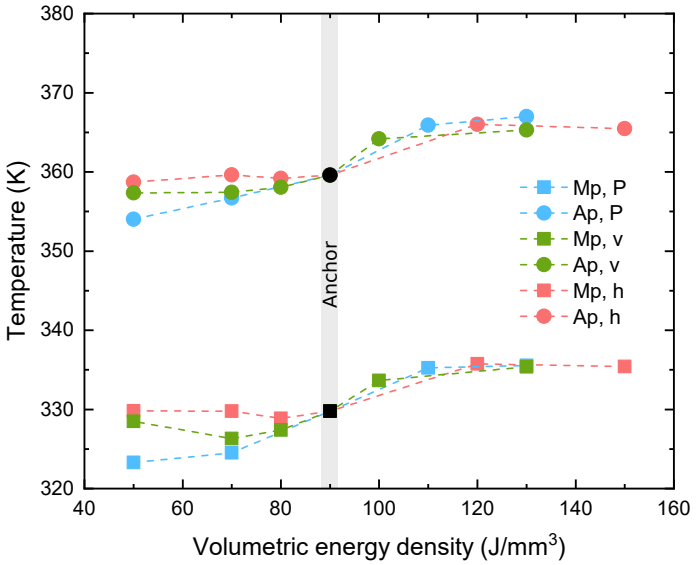


Figure 3.13: Austenite (A_p) and martensite (M_p) peak temperatures as a function of the VED. VED is changed through the three LPBF process parameters under study: laser power (blue), scanning speed (green) and hatch spacing (red). The anchor point is highlighted in black.

3.5 Conclusions

In this study, the influence of laser power, scanning speed and hatch spacing on porosity levels and the phase transformation behavior of samples produced by LPBF with a nearly equiatomic NiTi powder (Ni 55.86 wt.%) was investigated. Two approaches were used: The first one is a more traditional approach that tries to fill all the design space. On the other hand, the systematic approach is based in the study of each processing parameter and their effect both in manufacture and phase transformation behavior. The following conclusions are extracted:

1. In the broad approach, dense NiTi samples were obtained using VEDs in a range of 70-90 J/mm^3. An optimal process window was identified for VEDs of 70, 80 and 90 J/mm^3. The optimal design space was identified in similar ranges of laser power and scanning speed across all three VEDs.

2. In the systematic approach, dense NiTi samples were obtained using VEDs in a range

of 50-150 J/mm^3. Most of the samples displayed low porosity levels, less samples P4 and V1 the ones manufactured with the highest laser power (185 W) and the lowest scan speed (668 mm/s), respectively.

3. LED has proven to be an effective correlation method for predicting porosity levels in samples. However, variations in porosity levels between samples with the same LED indicate the presence of complex interactions between processing parameters. In contrast, VED showed a poor correlation with porosity levels in all approaches.

4. in the broad approach, DSC tests were performed on defect-free samples obtained from the porosity analysis (porosity<0.2%). Similar TTs were observed across these samples, independently of the processing parameters used and the selected VED.

5. In the systematic approach, TTs increase with VED regardless of the individual process parameter that is changed (laser power, scanning speed or hatch spacing). The highest TT changes were found between 75 to 110 J/mm^3 where the temperature increased 10 K. The variation of the TTs is attributed mostly to the Ni loss during the LPBF process.

6. The results indicate that, for the LPBF samples, the systematic approach provides a clearer understanding of the manufacturing effects and phase transformations associated with the process parameters. This approach, in which one parameter is varied while the other two remain constant, also requires fewer samples (15 samples) compared to the broad approach (54 samples), highlighting its lower economic cost.

Chapter 4

Thermomechanical and phase transformation behavior of additively manufactured NiTi SMA

4.1 Introduction

In the previous chapter, the influence of processing parameters on the LPBF NiTi structure and phase transformation was systematically investigated, revealing interesting trends. The findings demonstrated how these parameters impact both structural characteristics and phase transformations. However, the effect of these processing parameters on the thermomechanical properties remains to be explored. These thermomechanical properties are expected to be significantly influenced by the resulting microstructure.

It is widely acknowledged that variations in LPBF process parameters significantly influence the microstructure [55, 202, 21]. Soheil *et al.* [25] investigated the effects of laser power and scanning speed, demonstrating their significant influence on texture and grain size. Sayed *et al.* [195] examined the impact of input parameters on grain solidification, suggesting that hatch spacing is the most crucial variable to obtain a required texture. These microstructural variations are linked to the transformation behavior [27, 188, 189, 190].

Moreover, attaining desired mechanical properties in NiTi alloys holds paramount importance across diverse applications. Extensive research efforts have been centered on determining the mechanical characteristics of NiTi alloys under compression [203, 192, 204]. Additionally, some investigations have focused on understanding the anisotropic behavior of NiTi alloys

under varying mechanical stimuli [38]. Furthermore, other studies have observed the impact of cycling under different processing parameters [193].

The challenge inherent in the aforementioned studies lies in the lack of a holistic understanding of the connection between LPBF processing of NiTi SMAs and their thermomechanical behavior. Consequently, there is a pressing need for a research study with a carefully designed methodology to reveal the relationship between LPBF processing parameters and the SMA microstructure and thermomechanical properties. This chapter presents a comprehensive investigation into the alterations observed in the microstructure, transformation behavior, and thermomechanical properties of a carefully designed range of processing parameters. To perform this study each processing parameter has been monotonically altered from a proposed anchor point that served as a central point of the study. The results arising from this investigation aim to facilitate a deeper understanding of how each parameter influences the main characteristics of the LPBF NiTi-SMAs. This chapter is the second part of our published work [194].

4.2 Methodology

4.2.1 Design of experiments

To further investigate the influence of the processing parameters, the parameter sets applied in the second approach outlined in Chapter 3 were employed: laser powers (72-185 W), scanning speeds (668-1739 mm/s) and hatch spacings (28-85 µm) were used. The choice of parameters was made to obtain VEDs between 50 and 150 J/mm^3. More details can be shown in Figure 3.2 and Table 6.

Square samples with a section of 1x1 mm^2 and 10 mm of height were produced to study the microstructure. Furthermore, for investigating the thermomechanical behaviors, NiTi tensile samples with a gauge length of 5 mm and a cross-sectional area of 1x1 mm^2, were printed perpendicular to the build plate. Tensile samples of anchor, and P1, P4, V1, V5, H1, and H5, representing the extreme points for each processing parameter were printed. The NiTi powder used in this chapter is the same as that used in Chapter 3. All samples were printed using the same building conditions as those explained in the Chapter 3.

4.2.2 Material characterization

Microstructure analysis and precipitates' quantification

In order to perform the analysis, the specimens were mounted in epoxy. The metallographic preparation of the samples involved an initial grinding step using up to 1200-grit abrasive paper, followed by a polishing stage involving 9 µm and 3 µm diamond suspension. A final step with colloidal silica suspension was carried out. The polished specimens were etched using a solution of H_2O (80%) + HNO_3 (15%) + HF (5%) which has been used in other studies [143, 21]. Subsequently, images of the samples were captured using a Hitachi S-3400N Scanning Electron Microscope (SEM) with a magnification of 3000x and 6000x, a beam voltage of 15 kV, and high image contrast. For the precipitates' quantification, a convolution filter was initially applied to improve the contrast between the matrix and the precipitates in the black and white image. Subsequently, the Sauvola thresholding method was utilized to binarize the image, allowing the separate analysis of the precipitates. The threshold level was maintained across all analyzed images to ensure consistency between the results. Following binarization, a particle filter was applied as the final step to isolate the precipitates, effectively eliminating small particles from the background noise. Three images were extracted in diverse locations of each sample to obtain a statistically significant measurement of the precipitates' percentage.

4.2.3 Mechanical testing

Thermomechanical tests were conducted in an universal mechanical testing machine equipped with a climate chamber. A strain rate of 10^{-2} s^{-1} was used. The macroscopic strain of the samples was measured using Digital Imaging Correlation (DIC). The samples were heated and cooled at a rate of 10 K/min in a climate chamber for the actuation, training and TWSME tests. Three different tests were performed:

1. **Tensile tests:** Tensile tests were conducted to determine the elastic modulus of the austenite and martensite phases in each sample (see Figure 4.1a). The samples were loaded within the elastic regime, ensuring that no plastic deformation occurred. For the martensitic phase, tests were performed at RT. For the austenite phase, the temperature was first increased to a temperature of A_f+15 K. Once the temperature stabilized, the tensile tests were performed.

2. **Actuation tests:** A complete thermal cycle (440 - 300 - 440 K) was performed to observe the entire austenite-martensite transformations at stress levels of 50, 100, 150,

and 200 MPa, to study how the TTs change with the stress level. As it is observed in Figure 4.2a, the test temperature initially begins at a maximum of 440 K. Subsequently, the sample experiences the first loading to a stress of 50 MPa. Once this stress is achieved, the thermal cycle begins with the temperature being lowered up to 300 K and then raised again to 440 K. The same process is repeated for three additional loads (100, 150 and 200 MPa). In addition, both recoverable and plastic strain were measured according to Figure 4.1b.

3. **Training and TWSME tests:** Five complete thermal cycles at a stress of 200 MPa were performed to measure the saturation of the irrecoverable strain. Figure 4.2b indicates how the training test was performed. Similarly to the actuation test, the temperature started at 400 K but the sample was loaded at 200 MPa. Five thermal cycles were performed maintaining the sample loaded at the same stress level. Once the training was completed, the samples were unloaded (0 MPa) and subjected to one complete thermal cycle (TWSME). After the training test, the recoverable strain was measured (see Figure 4.1b).

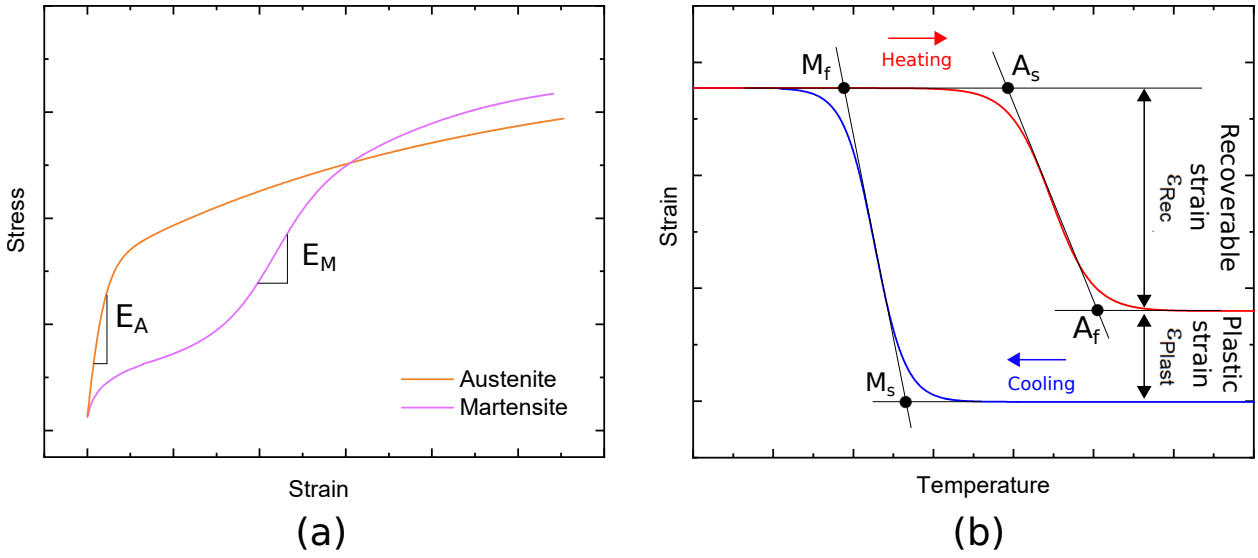


Figure 4.1: Example of how the thermomechanical variables are extracted from: (a) Tensile tests, (b) actuation and training tests.

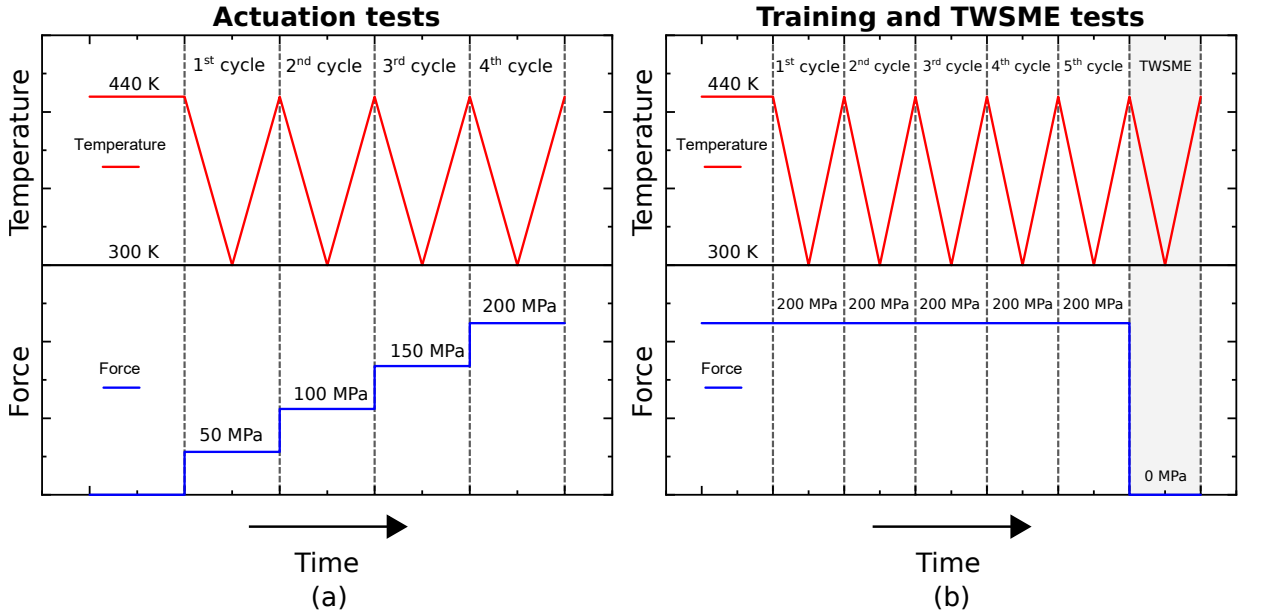


Figure 4.2: Force and temperature variations during: (a) actuation test, (b) training and TWSME tests.

4.3 Results

4.3.1 Microstructure

Figure 4.3 shows the different microstructures observed under the SEM for the variations in laser powers (samples P1-P4), scanning speeds (samples V1-V5), and hatch spacing (samples H1-H5). In most of the cases, the microstructure shows an arrangement of black precipitates (marked with yellow lines in the images) embedded in a grey matrix. Numerous studies [205, 206, 207, 208, 209] using similar equiatomic NiTi and Ti-rich compositions have reported that these precipitates correspond to Ti_2Ni embedded in a TiNi matrix (shown as grey in the images). These precipitates are known to play a crucial role in influencing the mechanical properties and phase transformation behavior of the alloy [205, 206, 207, 208, 209]. Changes in the population of these precipitates can be observed in Figure 4.3 as a function of the processing parameters. Notably, the amount of Ti_2Ni precipitates increases as the VED increases. Samples processed with the highest laser power (P4), lowest scanning speed (V1), and smaller hatch spacing (H1) exhibit a higher quantity of Ti_2Ni precipitates. In addition, the distribution of the precipitates changes with VED: they are evenly distributed for higher VEDs (90-150 J/mm^3, e.g., P4-V1-H1) and constrained to the melt pool boundaries at lower VEDs (70 J/mm^3, e.g., P2-V4-H4). Finally, at lower laser power (P1), high scan speed (V5),

and large hatch spacing (H5), non or a negligible amount of Ti_2Ni precipitates is observed. Furthermore, no cracks were observed during the analysis of the samples.

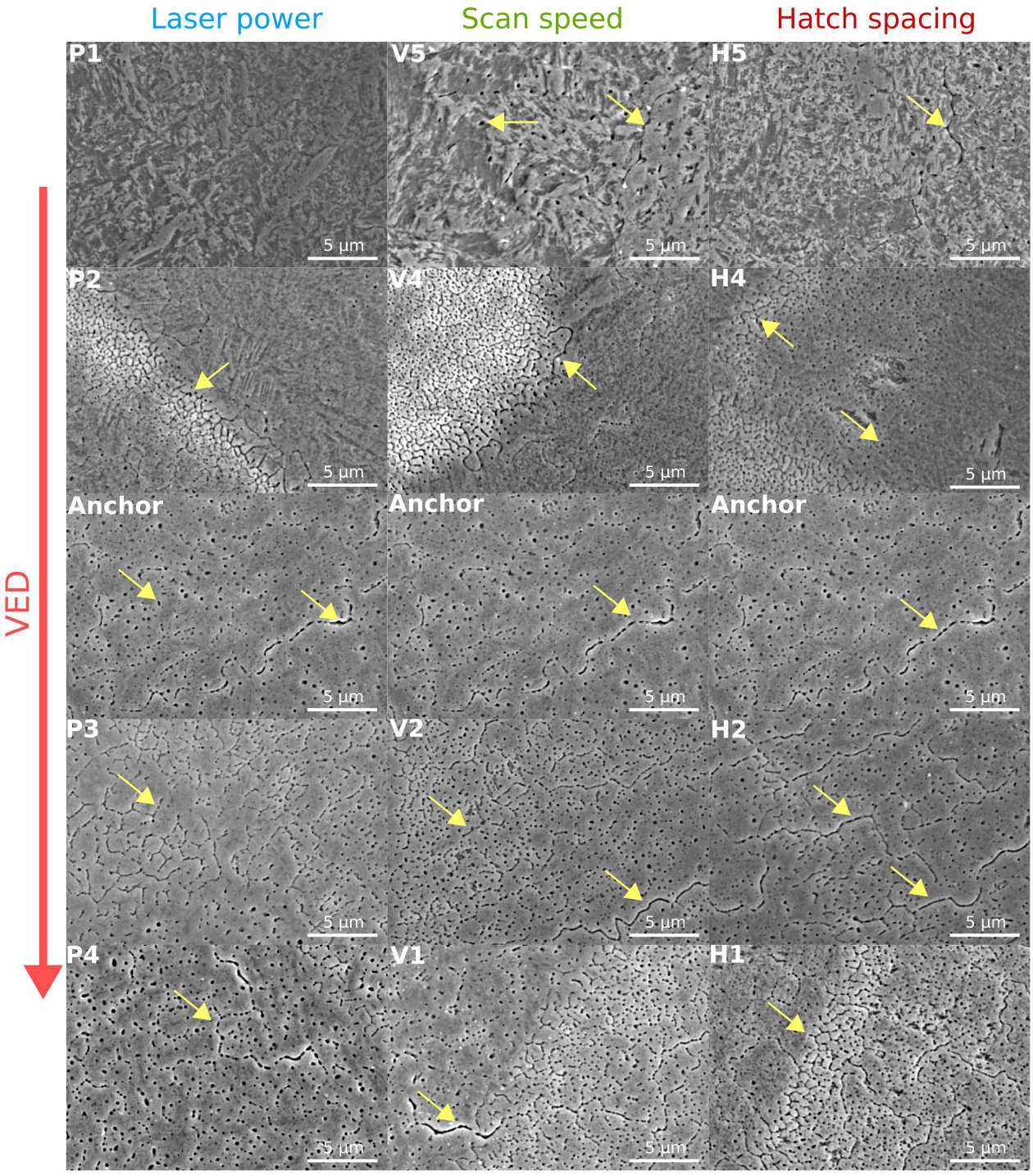


Figure 4.3: SEM images of the LPBF NiTi samples obtained by changing the process parameters: laser power (samples P1-P4), scanning speed (samples V1-V5) and hatch spacing (samples H1-H5). The results for the sample fabricated with the anchor parameter sets is also represented. Yellow arrows indicate the presence of Ti_2Ni precipitates.

4.3.2 Thermomechanical performance

Table 4.1 shows the elastic modulus for the martensite and austenite phases in each sample after the tensile tests. Similar results can be observed for the different processing parameters. The elastic modulus of the austenite ranges between 44-49 GPa, while the results of the martensite phase are lower moving between 14-17 GPa also observed in other works in the literature [210].

Sample	**E_A (GPa)**	**E_M (GPa)**
Anchor	48.37	16.41
P1	49.17	14.83
P4	44.92	14.66
V1	45.95	15.14
V5	44.73	15.29
H1	49.25	16.68
H5	45.45	14.72

Table 4.1: Elastic modulus of the austenite and martensite phases in each sample.

Figure 4.4 depicts the strain-temperature results of the actuation tests performed on the NiTi tensile samples. The samples were initially loaded to 50 MPa at 440 K, subsequently cooled to 300 K, and then reheated to 440 K. The same thermal cycle was repeated while the samples were loaded at 100 MPa, 150 MPa and 200 MPa. The curves of the samples with variations in laser power, scanning speed, and hatch spacing are shown in blue, green, and red respectively. Darker colors represent higher VEDs, while lighter colors indicate lower VEDs. The anchor point is indicated in black and it is used as a reference in all cases. Figure 4.4 shows that for different stresses between low and high VED parameters, there are changes in the curves along the x-axis (temperature) and y-axis (strain).

To further elucidate these changes, the thermomechanical curves presented in Figure 4.4 have been processed as indicated in Figure 4.1 to extract the recoverable strain (ε_{Rec}), the plastic strain ($\varepsilon_{\text{Plast}}$) and the TTs ($M_s$, M_f, A_s and A_f) as a function of the stress level. The obtained values for these variables are presented in Figure 4.5. The color-coded used is the same as explained previously for Figure 4.4.

The values of ε_{Rec} and $\varepsilon_{\text{Plast}}$ are represented in Figures 4.5a, 4.5c and 4.5e. Lower VED levels – which result from low laser power (P1), high scanning speed (V5) and high hatch spacing (H5) – result in higher recoverable strains (∼3.0-3.5%), while higher VED levels – which result from high laser power (P4), low scan speed (V1) and low hatch spacing (H1) – result in lower

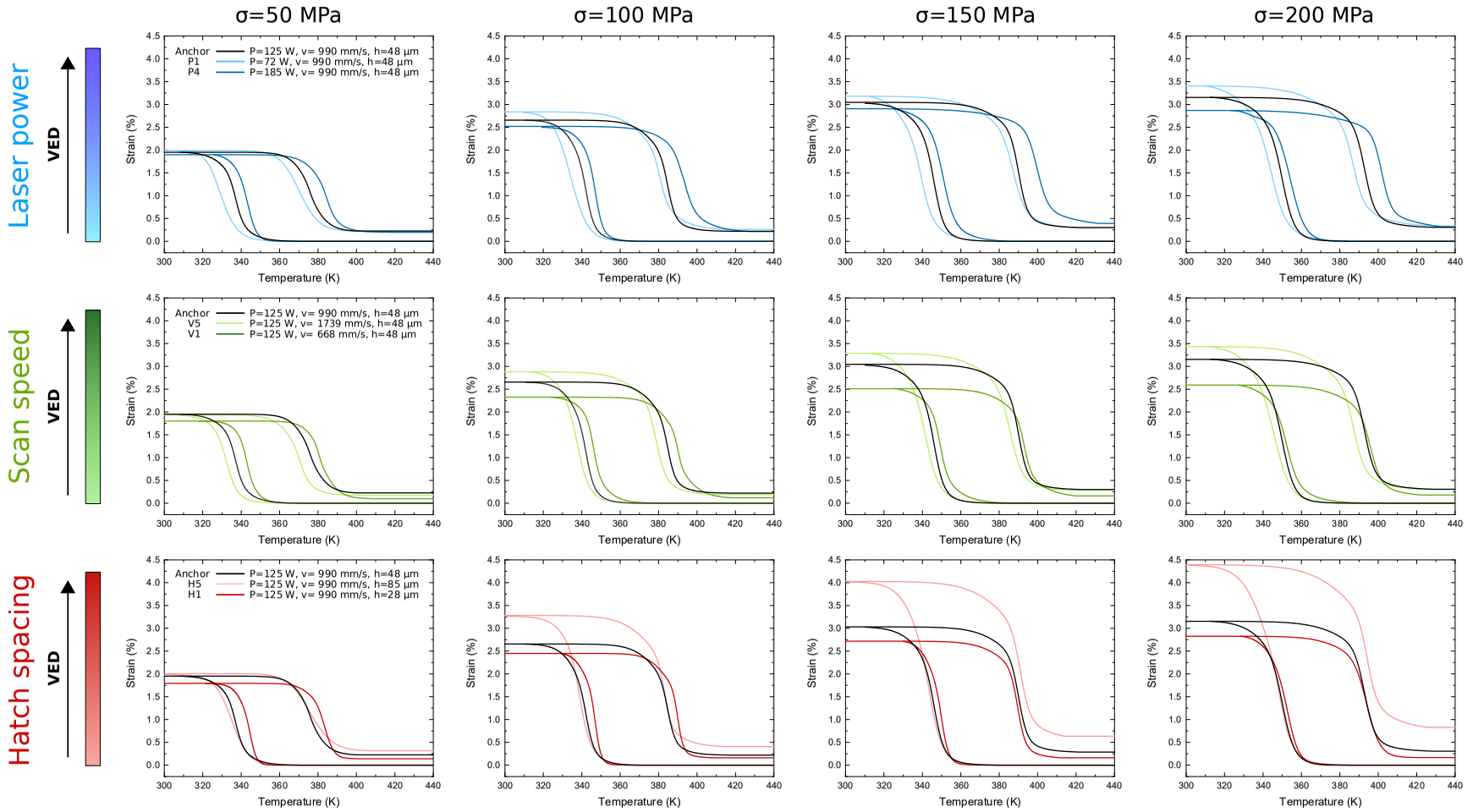


Figure 4.4: Actuation test: strain-temperature response under constant stresses of 50, 100, 150 and 200 MPa, of the NiTi tensile samples additively manufactured by changing the process parameters: laser power (samples P1 and P4), scanning speed (samples V1 and V5) and hatch spacing (samples H1 and H5). The results for the sample fabricated with the anchor parameter sets are represented in black.

recoverable strains (∼2.25-2.5%). In addition, a saturation of the recoverable strain at 200 MPa can be observed in all cases. Furthermore, it is interesting to note a smaller influence of the processing parameters on the ε_{Rec} and $\varepsilon_{\text{Plast}}$ at lower stress levels (e.g., $\sigma = 50$ MPa). Generally, the increase of the stress level (50 to 200 MPa) produces an increment of the recoverable strain in all cases from 1.75% to 2.25-3.5%. In contrast, the plastic strain remains minimal for all the processing conditions except for the one with higher hatch spacing (H5) in which the plastic strain reaches a value of approximately 0.8% at 200 MPa.

In terms of the TTs depicted in Figures 4.5b, 4.5d and 4.5f, a consistent trend is also visualized. The TTs of the samples with lower VEDs (P1, V5 and H5) present lower values than the ones fabricated with higher VEDs (P4, V1 and H1), with the TTs of the anchor point situated between the extreme cases. An increase of the TTs with higher stress levels can also be observed.

Figures 4.6a and 4.6b show five training cycles at 200 MPa for each tensile sample tested. For all cases, the strain-temperature curves decrease in strain magnitude, and also experience a slight downward and leftward shift along the cycles. In Figure 4.6c, the strain-temperature curves at zero stress level for the different processing parameters are plotted to show the two-way shape memory effect (TWSME). The anchor point (in black) is used as a reference. A similar trend to the previous actuation test is observed: samples fabricated with lower VEDs (P1, V5 and H5) exhibit a higher strain level than the samples fabricated with higher VEDs (P4, V1 and H1). In addition, the cycle for the anchor point lays between the lower and higher VEDs.

The training curves from Figure 4.6 have been analysed to extract the ε_{Rec} and $\varepsilon_{\text{Plast}}$, see Figure 4.7. Similar tendencies can be observed for the plastic strain across all the processing conditions. The maximum plastic strain (∼0.8-0.9%) per cycle is reached during the first cycle and then it decreases until reaching a saturation point by the third cycle (∼0.25%). This phenomenon has also been observed by Lahoz *et al.* [211]; they found a reduction on the transformation temperatures as the number of cycles increases. In addition, samples produced with lower VEDs (P1, V5 and H5) experience higher plastic strains in the first cycle (∼0.8-0.9%) than the ones produced with higher VEDs (P4, V1 and H1) (∼0.3-0.6%). Furthermore, the plastic strain levels at 200 MPa for the first cycle of the training tests are found to be higher (∼0.3-0.9%) than the ones observed in the actuation tests (∼0.1-0.8%) (see Figure 4.5). This difference occurs because during the actuation test, the plastic strain is accumulated from the first cycle at 50 MPa. Hence, when the sample reaches the fourth cycle at 200 MPa, the total accumulated plastic strain is more saturated when compared to the first cycle of the actuation test, where the sample did not undergo any previous plastic

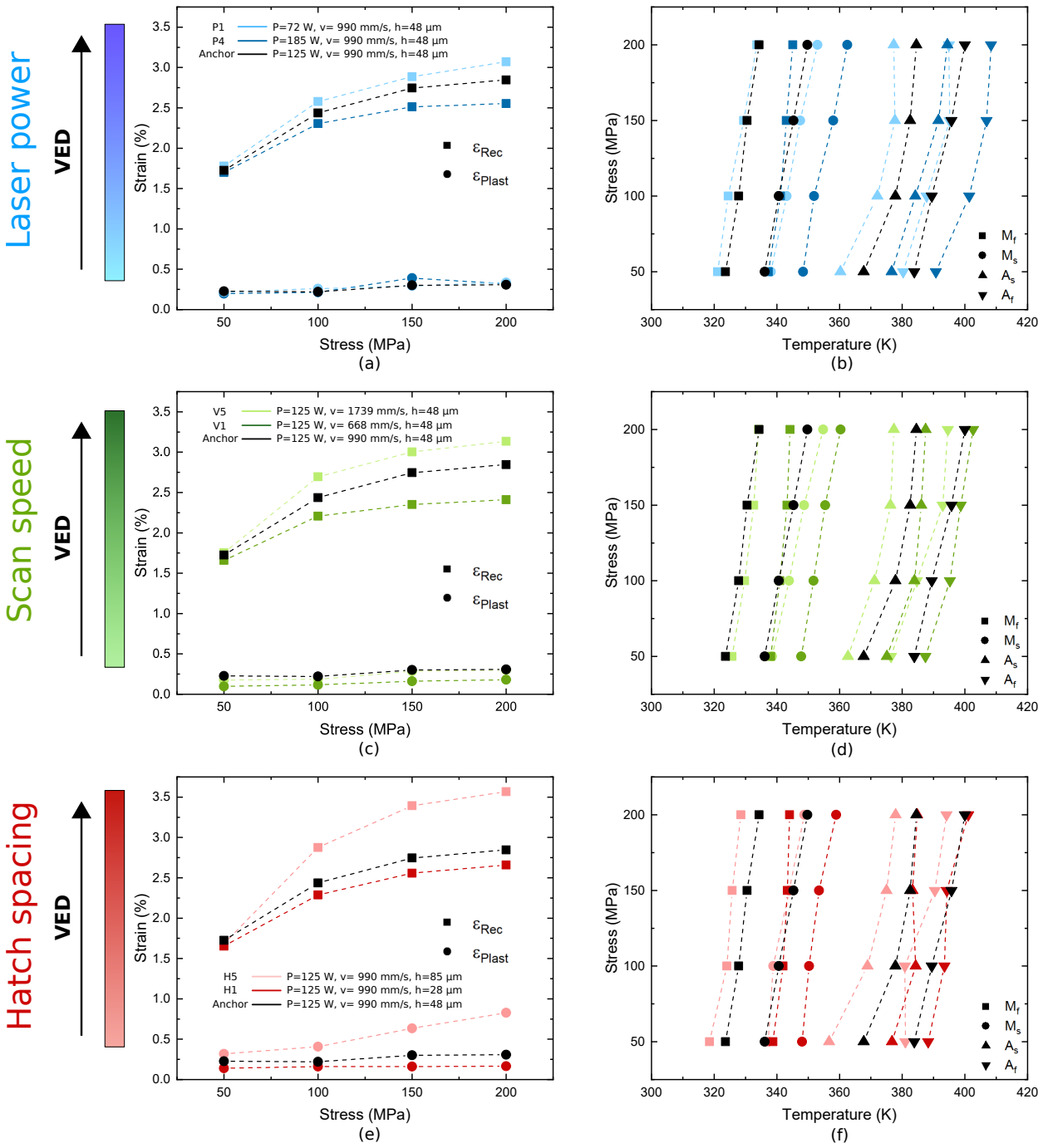


Figure 4.5: Actuation test: (a,c,e) Recoverable strain (squares) and plastic strain (circles) are shown as a function of the stress level. (b,d,f) The TTs are displayed as a function of the stress level. (a-b) correspond to variations in laser power (samples P1 and P4), (c-d) depict changes in scanning speed (samples V1 and V5), and (e-f) represent the changes in hatch spacing (samples H1 and H5). In all diagrams, the anchor point is highlighted in black. Results are obtained from the analysis of the curves in Figure 4.4.

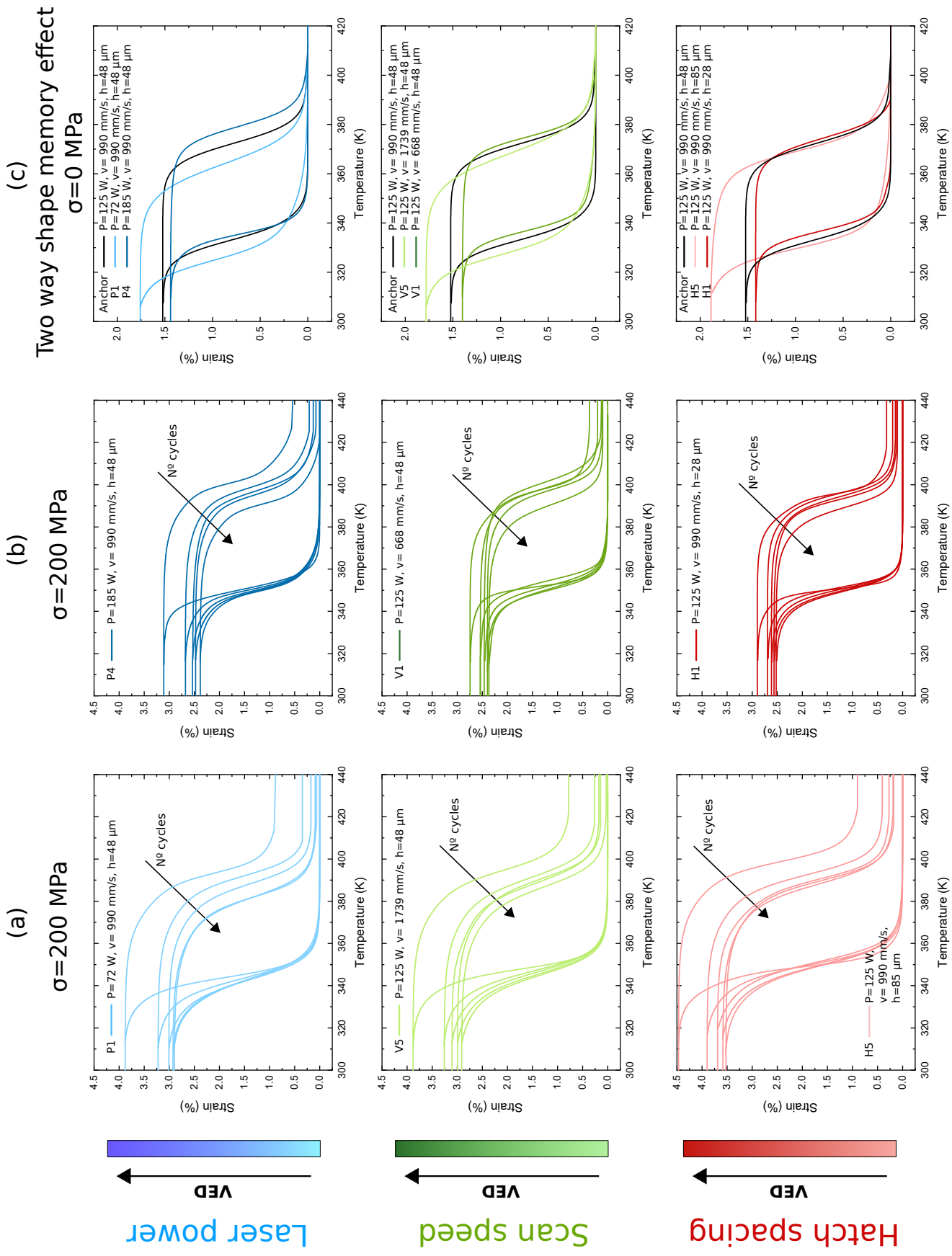


Figure 4.6: Training and TWSME tests: (a-b) Five training cycles under a constant stress of 200 MPa and (c) TWSME cycle after the 5 training cycles, of the tensile samples fabricated by changing: laser power (blue), scanning speed (green) and hatch spacing (red).

deformation.

The TWSME curves presented in Figure 4.6 have been processed to extract the recoverable strains as a function of the laser power, scan speed and hatch spacing, as indicated in Figure 4.8. According to the obtained values, samples fabricated with lower VEDs (e.g., lower laser powers (P1), higher scan speeds (V5) and larger hatch spacings (H5)) display higher recoverable strains (∼1.75-1.90%), while printing with higher VEDs (e.g., higher laser powers (P4), lower scan speeds (V1) and lower hatch spacings (H1)) result in lower recoverable strains (∼1.40-1.45%). It is noticeable the capability of the processing conditions in varying the recoverable strain of the alloy from the same foundational power: 18% ε_{TWSME} decrease per 113 W of laser power, 28% ε_{TWSME} increase per 1071 mm/s of scan velocity and 33% ε_{TWSME} increase per 57 µm of hatch spacing. The specific differences in the effect of each processing parameter will be analyzed in more detail in Section 4.4.

4.4 Discussion

4.4.1 Influence of processing parameters on the microstructure

The most common precipitates in SMAs are Ti_2Ni, which primarily form in Ti-rich or near-equiatomic NiTi, and Ni_4Ti_3, which are typical in Ni-rich compositions [212]. As observed in Figure 4.3, Ti_2Ni precipitates can form at grain boundaries or be uniformly dispersed within the matrix. The formation of these precipitates can be explained as follows: during the LPBF process, the thermal impact of the laser causes the formation of different melt pools (in shape and size). This input energy causes rapid melting of the powder particles. The molten material experiences rapid cooling and solidification due to the localized laser heating and the adjacent cooler material. This rapid cooling leads to high solidification rates, which affects the microstructure of the alloy [213]. Nickel has a higher tendency to evaporate during the LPBF process due to its higher vapor pressure compared to titanium (see Figure 3.12a) [199]. This evaporation leads to a local depletion of Ni in the melt pool. Hence, in the absence of nickel, the chance of Ti-rich precipitations to occur, increases. As the molten material solidifies, the remaining Ni and Ti atoms redistribute, sometimes leading to segregation of Ti-rich regions. The rapid solidification can lead to supersaturation of Ti in the matrix because the equilibrium concentration of Ti in the NiTi phase cannot be maintained due to the fast cooling rates [214] . This supersaturation can drive the nucleation and growth of Ti_2Ni precipitates. These precipitates form to reduce the supersaturation of Ti in the NiTi

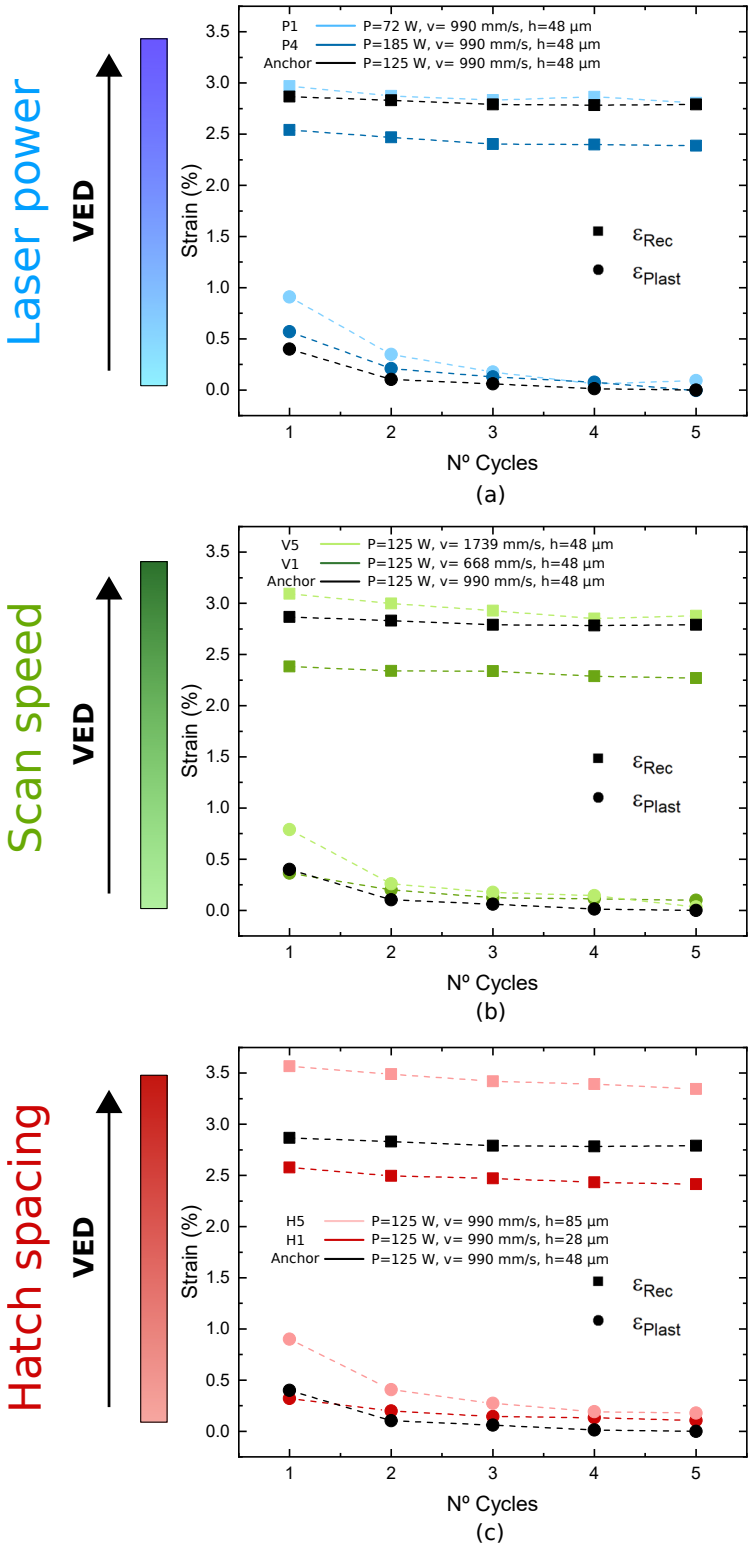


Figure 4.7: Training test: recoverable strain and plastic strain plotted along the number of cycles for the training tests for: (a) variations in laser power (samples P1 and P4), (b) changes in scanning speed (samples V1 and V5) and (c) changes in hatch space (samples H1 and H5). In all diagrams the anchor point is highlighted in black.

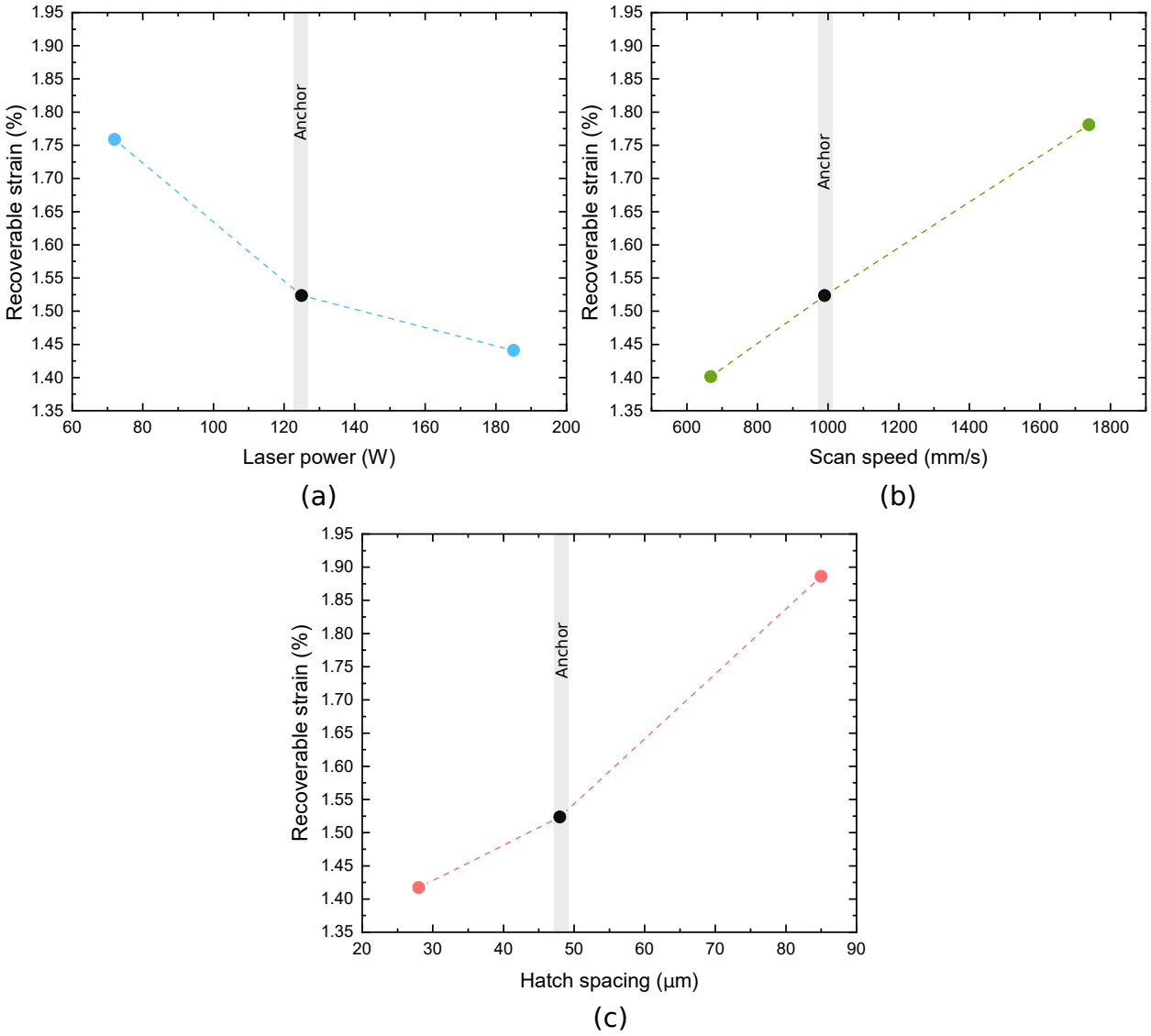


Figure 4.8: TWSME test: Recoverable strain extracted from the TWSME tests shown in Figure 4.6c modifying the laser power (blue), scanning speed (green) and hatch spacing (red). The anchor point is highlighted in black.

matrix, effectively acting as a sink for the excess of Ti atoms [50].

To quantify the effect of the processing parameters on the formation of Ti_2Ni precipitates, the solid fraction of Ti_2Ni precipitates was evaluated from SEM micrographs of the samples printed with different processing parameters. Figure 4.9a shows the measured values of the fraction of Ti_2Ni precipitates as a function of the VED, obtained by varying the laser power, scanning speed and hatch spacing. The results show that the processing parameters used during the LPBF process affect the amount of precipitates formed - as the VED increases, a higher amount of Ti_2Ni is found.

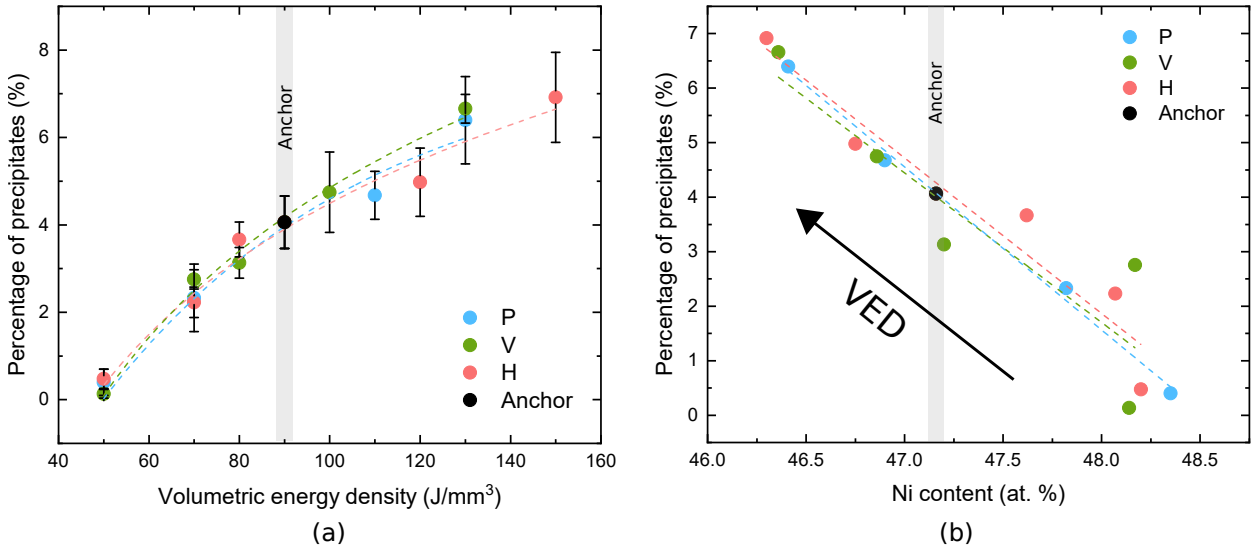


Figure 4.9: (a) Percentage of precipitates present in all LPBF fabricated samples; (b) Correlation between the percentage of precipitates and the nickel content in all LPBF fabricated samples. In all diagrams the anchor point is represented in black, while samples manufactured with variations in: laser power (P) are denoted in blue, scanning speed (V) in green, and hatch spacing (H) in red.

This higher precipitation of Ti_2Ni as the VED is increased can be explained by the increased evaporation of nickel - Figure 3.12b. The whole process is schematically presented in Figure 4.10. As elucidated previously, higher VEDs lead to an increased evaporation of Ni. This local depletion of Ni results in a Ti-rich environment which, as explained before, can produce a higher driving force for the formation of Ti_2Ni precipitates. Therefore, the higher the VED, the higher fraction of Ti_2Ni precipitates, which is in agreement with the trends observed in Figure 4.9a-b. Furthermore, no relevant differences were found in the percentage of Ti_2Ni precipitates with the selected processing parameters (e.g., laser power, scan speed, or hatch spacing) for the same VED.

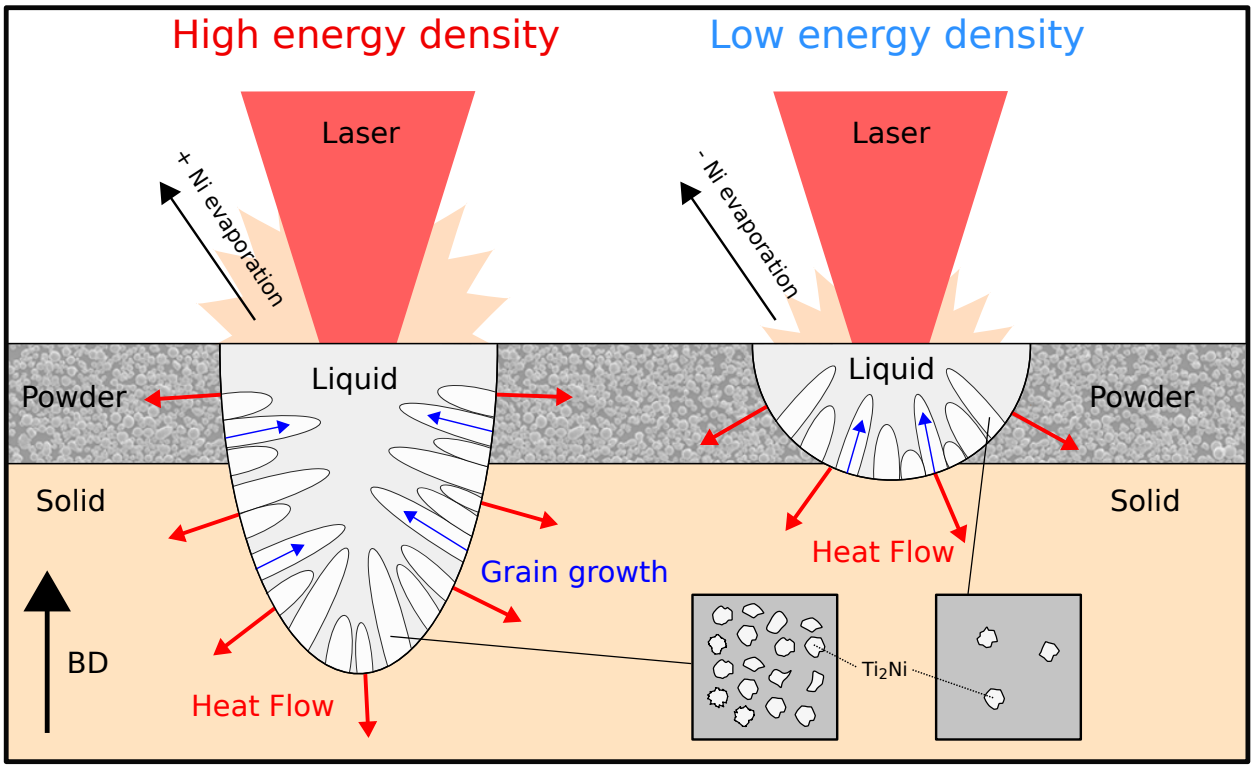


Figure 4.10: Schematic of the physical processes occurring at the melt pool during the LPBF manufacturing of NiTi alloys. At higher VED, higher amounts of nickel evaporate. BD stands for build direction (of the LPBF process).

4.4.2 Influence of processing parameters on the transformation temperatures TTs

The lower Ni/Ti ratio found in samples with higher VEDs (see Figure 3.12b) can lead to an increase of the TTs [86]. This is confirmed in the results presented previously in Figure 3.13 (Chapter 3), which shows the significance of VED on TTs. This same effect observed on the TTs in the unloaded samples is observed for the case of the TTs of the loaded samples (through stress actuation tests) as indicated in Figure 4.11. In this Figure, the evolution of the transformation temperatures extracted from Figures 4.5b, 4.5d and 4.5f is presented as a function of the VED for each stress level (50, 100, 150 and 200 MPa). It is noted that in terms of TTs, at the low stress level of 50 MPa, there are not relevant differences in the parameter selected to achieve a given VED (e.g., laser power, scan speed or hatch spacing) as indicated in Figures 3.13 and 4.11a. However, at higher stress levels (e.g., 100-200MPa – see Figures 4.11b-d), it can be observed that for higher VEDs (120-150 J/mm^3), the effect of the stress in increasing the peak TTs is more acute if the VED is achieved through changes in power or scan velocity rather than in hatch spacing.

Figure 4.12 illustrates the A_s TT for all samples in the training test. A diminishing trend in the TT is observed as the number of cycles increases, which can be attributed to the cyclic hysteresis behavior of NiTi. Despite this reduction, the overall phase transformation trend remains consistent. Samples P4, V1, and H1 exhibit the highest TTs, while samples P1, V5 and H5 display the lowest values. This behavior is further demonstrated in Figure 4.13 where the A_s TT is displayed for each sample along the VED. As observed in the actuation test, as higher is the VED, higher is the TTs independently of the processing parameter used to change it. An interesting range of TTs can be achieved depending on the VED used to manufacture and the number of training cycles performed.

4.4.3 Influence of processing parameters on the thermomechanical properties

Figure 4.14 presents the elastic modulus values for both the austenite and martensite phases in all samples as a function of the VED. The results do not show a specific trend, with the elastic modulus similar in the martensite phase in all samples ($\sim$ 15 %) and the elastic modulus of the austenite phase also showing minimal variation, averaging $\sim$ 47 GPa. It is important to note the significant disparity between the two elastic modulus. The measured values of this modulus for martensite are smaller than those for austenite. This is attributed to the

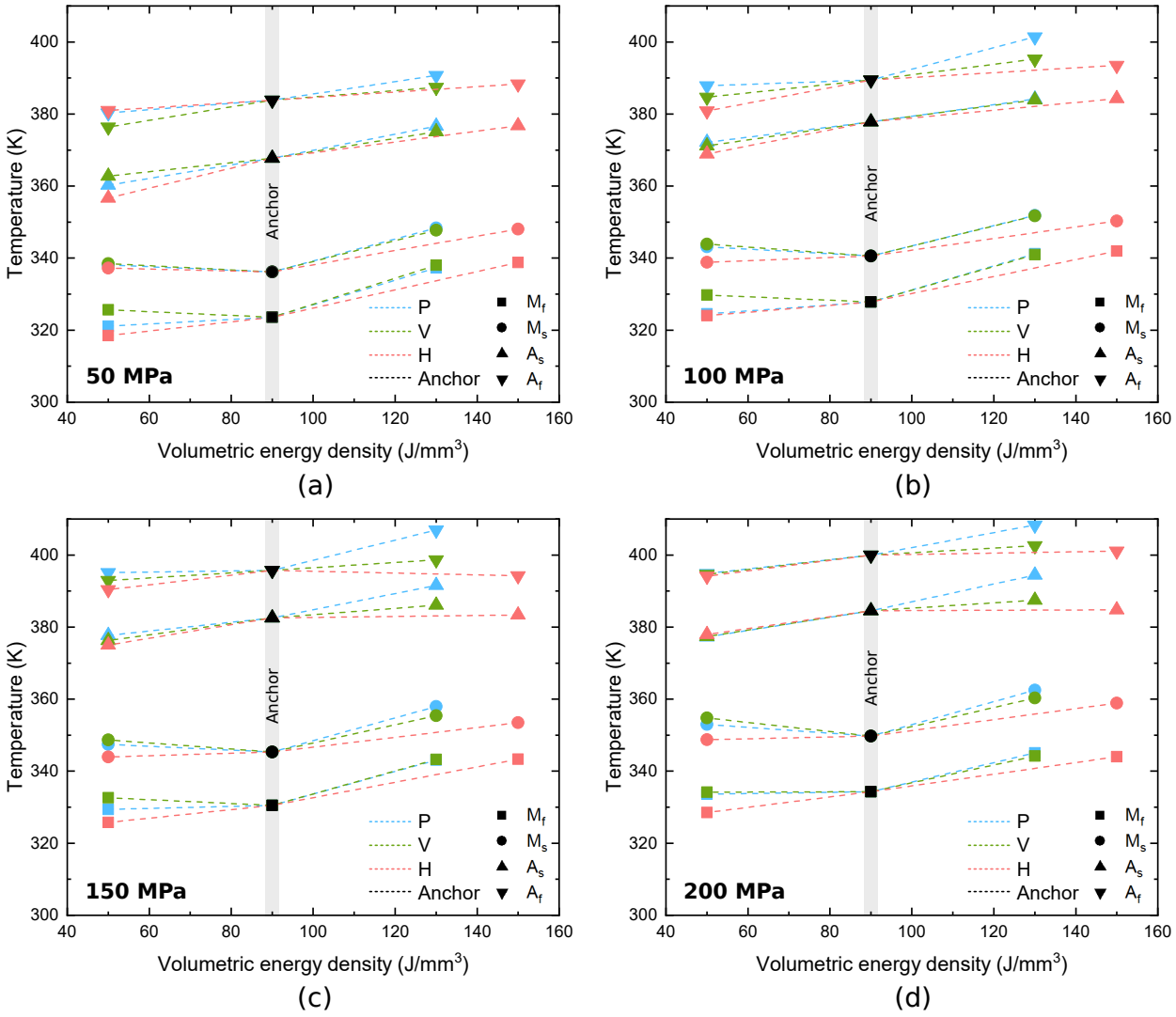


Figure 4.11: Results of the transformation temperatures at different stress levels extracted from the actuation test (Figure 4.4): (a) 50 MPa, (b) 100 MPa, (c) 150 MPa and (d) 200 MPa, where the color code correspond to changes in laser power (blue), scanning speed (green) and hatch spacing (red). The anchor point is highlighted in black. Samples corresponding to the lowest VEDs (P1, V5, and H5) are located in the lower TTs region and samples corresponding to the highest VEDs (P4, V1, and H1) are positioned on the higher TTs region.

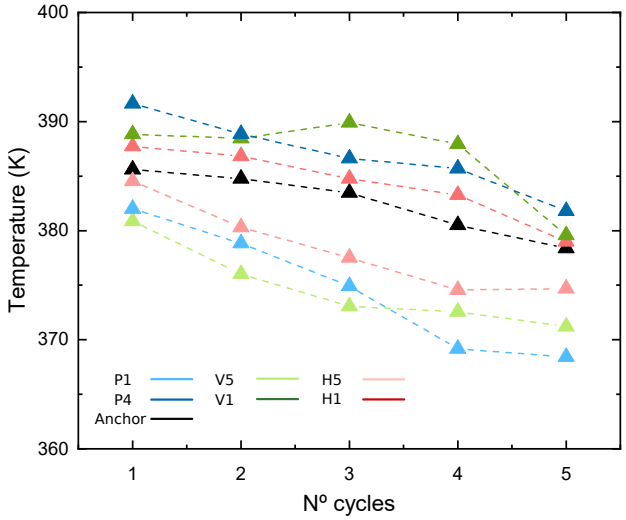


Figure 4.12: Austenite start temperature (A_s) along the training cycles for the different samples. The color code correspond to changes in laser power (blue), scanning speed (green) and hatch spacing (red). The anchor point is highlighted in black.

high mobility of the twin martensite boundaries, which makes the martensite vulnerable to deformation [215].

Figure 4.15 shows the recoverable strain of the actuation tests extracted from Figure 4.4 as a function of the VED for the different stress levels. Observing these results, a clear trend in the y-axis (strain) is observed: as the VED increases, the recoverable strain decreases, at the stress levels of 100, 150 and 200 MPa. Furthermore, it is demonstrated that the stress level seems to play an important role in the distinct effect of each laser parameter on the recoverable strain. The higher the stress level, the higher the recoverable strain values obtained for the same VED.

The observed reduction of recoverable strains as VEDs increases can arise from multiple factors occurring during processing [216, 217, 218, 102]. As previously reported, precipitates in NiTi SMAs can significantly influence their thermomechanical properties [216, 217, 218, 102]. Noteworthily, this is observed in this study, where NiTi samples additively manufactured with higher VEDs (e.g., higher laser powers (P4), lower scan speeds (V1) and lower hatch spacings (H1)), which exhibit higher levels of Ti_2Ni precipitates (see Figure 4.9b), are the ones with lower recoverable strains. Previous work has found that presence of precipitates in NiTi alloys can affect the actuation response [219, 220]. That work found that coherent non-transforming precipitates can retard transformation in the surrounding matrix [219, 220].

Figure 4.16 shows the recoverable strain at zero stress level obtained from the TWSME tests presented in Figure 4.6. The recoverable strain values are presented as a function of VED

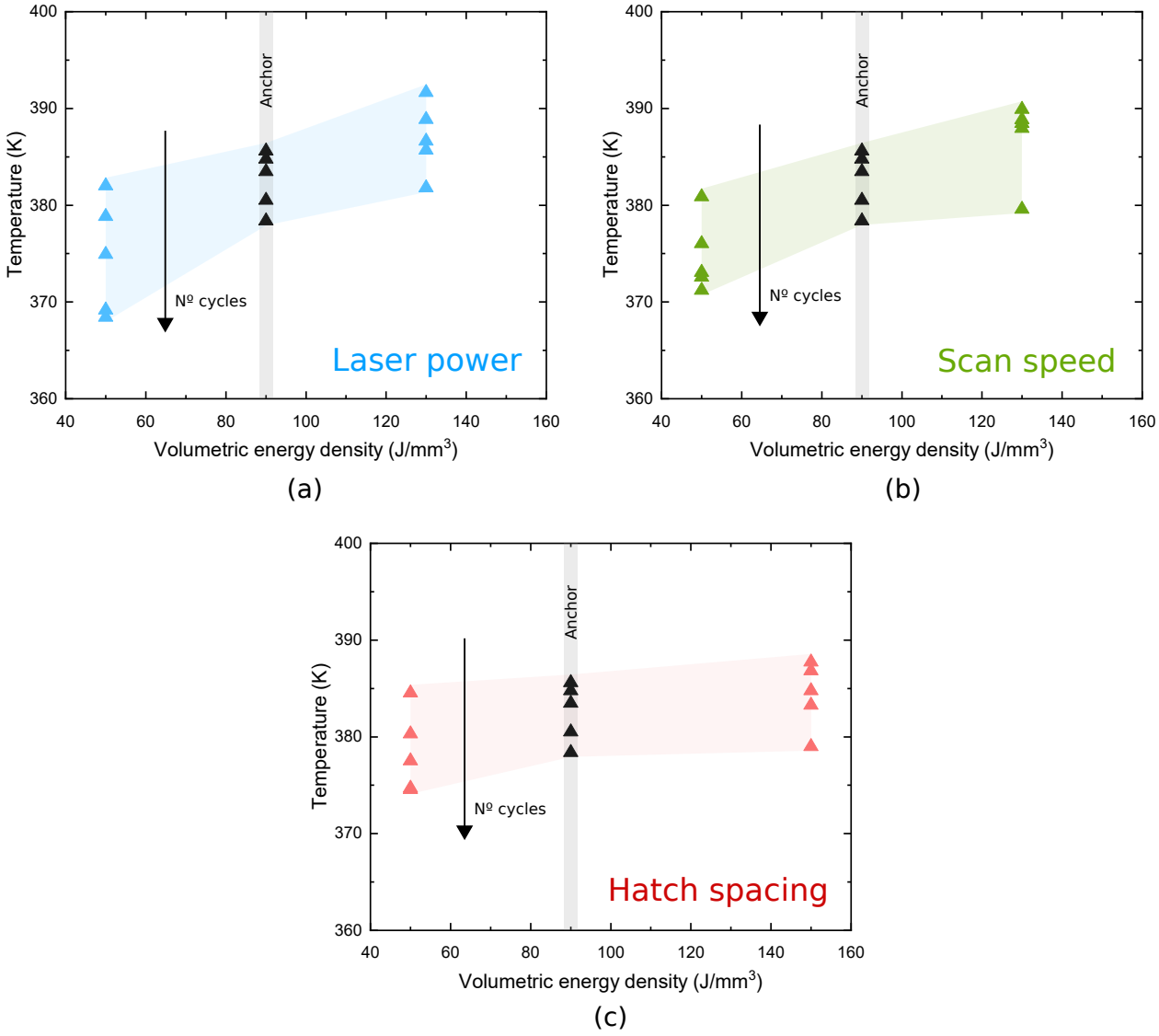


Figure 4.13: Austenite start temperature (A_s) in the different samples along the VED in the training test. The color code correspond to changes in laser power (blue), scanning speed (green) and hatch spacing (red). The anchor point is highlighted in black.

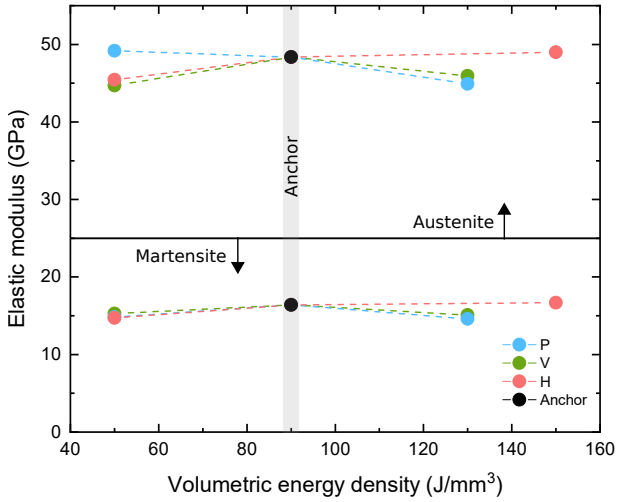


Figure 4.14: Elastic modulus of austenite (top) and martensite (bottom) phases of all the samples along VED. The color code correspond to changes in laser power (blue), scanning speed (green) and hatch spacing (red). The anchor point is highlighted in black.

achieved through changes in laser power, scan velocity and hatch spacing. The tendencies observed are similar to the ones shown for the recoverable strain in the actuation tests: lower VED conditions (P1, V5 and H5) present higher recoverable strains (∼1.75-1.90%) than higher VED conditions (P4, V1 and H1) (∼1.40-1.45%). Additionally, by observing the slope of the recoverable strain change with the VED, increasing the hatching distance seems to be the most effective way to achieve a higher recovery strain (∼1.9%) for the case of low VEDs (50-90 J/mm^3). However, for higher VEDs (90-150 J/mm^3) the hatching distance present a lower impact on the recoverable strain rate, similarly to the laser power. This lower impact of the processing conditions at higher VED might be produced by the overlapping of the heat affected tracks [221].

Figure 4.17 depicts the recoverability rate of all samples in the training test during thermomechanical cycles at 200 MPa. This rate was calculate using the recoverable strain and dividing by the total strain of the cycle. It can be shown how a similar trend occurs for all samples, obtaining lower recoverable rates in the first cycles and higher levels after the second/third cycle. This happens because the recoverable and plastic strains decrease as the number of cycles increases (see Figure 4.7). The degradation of recoverable strain has also been reported in other studies and is attributed to the accumulation of retained martensite [222, 223]. Conversely, during phase transformation, strain incompatibilities in the austenite-martensite interface induce local stresses that exceed the plastic yield stress triggering dislocation slip. During propagation of the austenite-martensite interfaces, dislocations spread through the transformed regions. Upon completion of the reverse transformation, a significant number

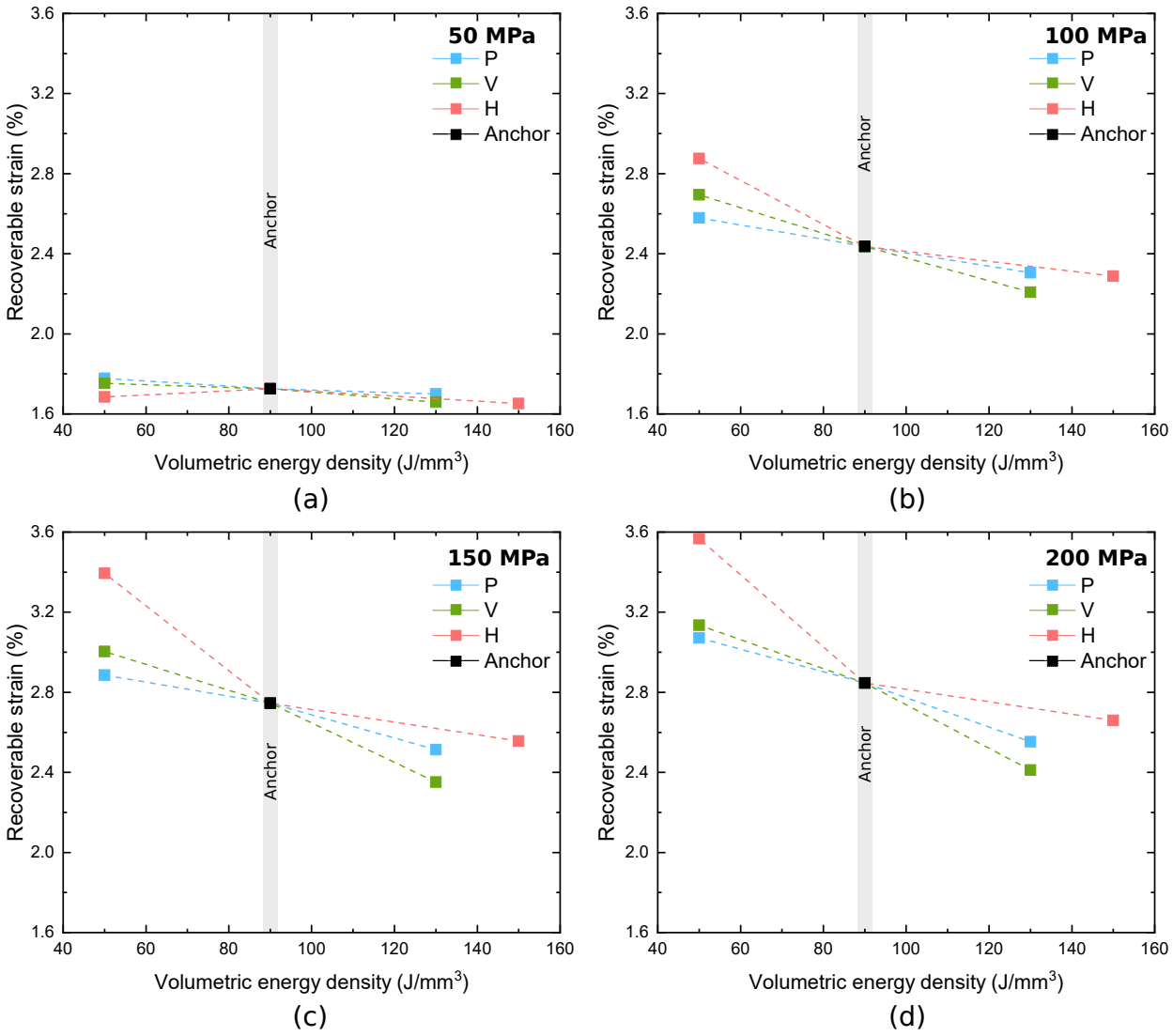


Figure 4.15: Recoverable strain as a function of the VED extracted from the actuation tests shown in Figure 4.4 for each stress level: (a) 50 MPa, (b) 100 MPa, (c) 150 MPa and (d) 200 MPa. Changes in the VED were produced by modifying the laser power (blue), scanning speed (green) or the hatch space (red). The anchor point is highlighted in black.

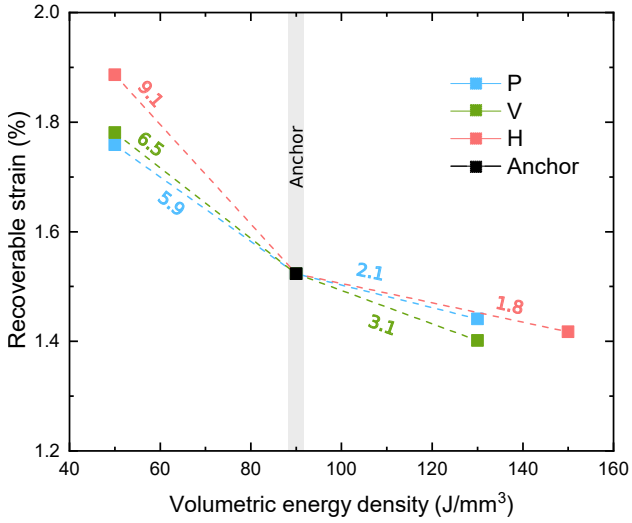


Figure 4.16: Recoverable strain as a function of the VED extracted from the TWSME tests shown in Figure 4.6c. Changes in the VED were produced by modifying the laser power (blue), scanning speed (green) or the hatch space (red). The anchor point is highlighted in black. The slopes of the lines ($\frac{\Delta\varepsilon_{Rec}}{\Delta \mathrm{VED}}10^{-5}$) are also depicted.

of dislocations remain, leading to a residual strain (plastic strain). As a result of plastic hardening, slip deformation progressively becomes more constrained along the cycles up to stabilization of the thermomechanical response (saturation) [224].

Furthermore, another trend is visualized in Figure 4.17. High VED samples (P4, V1 and H1) have lower recoverable strain along the cycles and lower plastic strain in the first cycle, obtaining higher recoverability rates. In contrast, low VED samples (P1, V5 and H5) show greater recoverable strains along the cycles and higher plastic strain in the first cycle, obtaining lower recoverability rates. Lower recoverable strains are produced in high VED samples due to the presence of Ti_2Ni, which restricts the transformation strain [219, 225]. Higher VED also implies higher thermal gradients during the LPBF process, which results in elongated grain structures [21, 226]. This rapid heating and cooling creates thermal stresses in the material that promote dislocation formation as the VED used increases [227, 228, 229]. The higher amount of dislocations makes slip deformation more difficult, so higher local stresses are needed to create dislocation slip during the first cycle [224]. Therefore, samples manufactured with high VED parameters obtained low levels of plastic deformation in the first cycle compared to the sample manufactured with low VED parameters.

Figure 4.18 illustrates the recoverable strain of all samples during the training tests as a function of VED. A similar trend to that observed in the actuation and TWSME tests is depicted: higher VED values used in sample fabrication correspond to lower recoverable

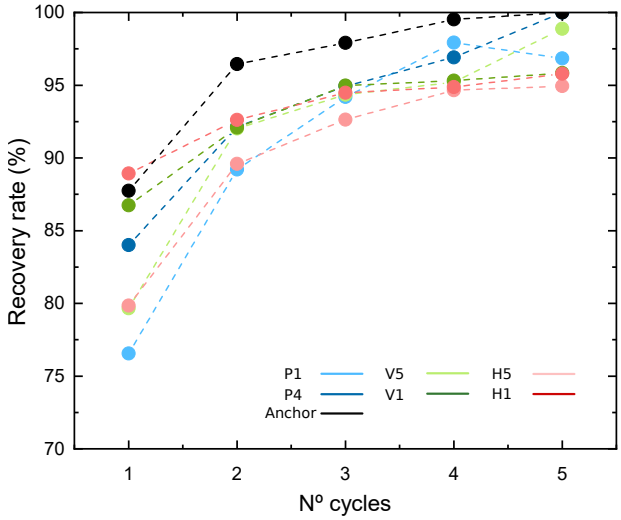


Figure 4.17: Recovery rate of all samples along cycles in the training test. The color code correspond to changes in laser power (blue), scanning speed (green) and hatch spacing (red). The anchor point is highlighted in black.

strain. In addition, the degradation of recoverable strain is consistent across all samples, demonstrating no dependence on the VED employed during the manufacturing process.

4.4.4 Implications of the observed results in the LPBF of SMAs

Based on these results, the role of LPBF processing parameters in defining the thermomechanical behaviour of this SMA alloy, is noted. Further studies should be made to extend these findings to a wider range of alloys. Nevertheless, it seems plausible to tailor the transformation behaviour (e.g., the recoverable strain as seen in Figures 4.15 and 4.16, or the TTs as seen in Figure 4.11) of the material through the adequate selection of the processing parameters. Therefore, in the LPBF of SMAs, parameter selection needs to be considered, not only for achieving low defect levels as typically for other materials, but also to achieve the desired transformation behaviour defined by the intended application of the part. This change in the transformation behaviour could be exploited for example in the construction of monolithic SMA actuators like bistable microvalves. Typically, SMA actuators are composed of several parts with different thermomechanical properties than in conjunction would provide the desired actuation response [230, 231, 232, 233, 234]. By using LPBF and careful selecting the processing parameters for different regions of the part, the same SMA powder may be used for the whole part while producing the desired actuation response. For example, in the case of SMA bistable valves or positioning stages, the traditional design used in previous studies [235, 236] involves the selective increase of the temperature of a given region/part of the valve to

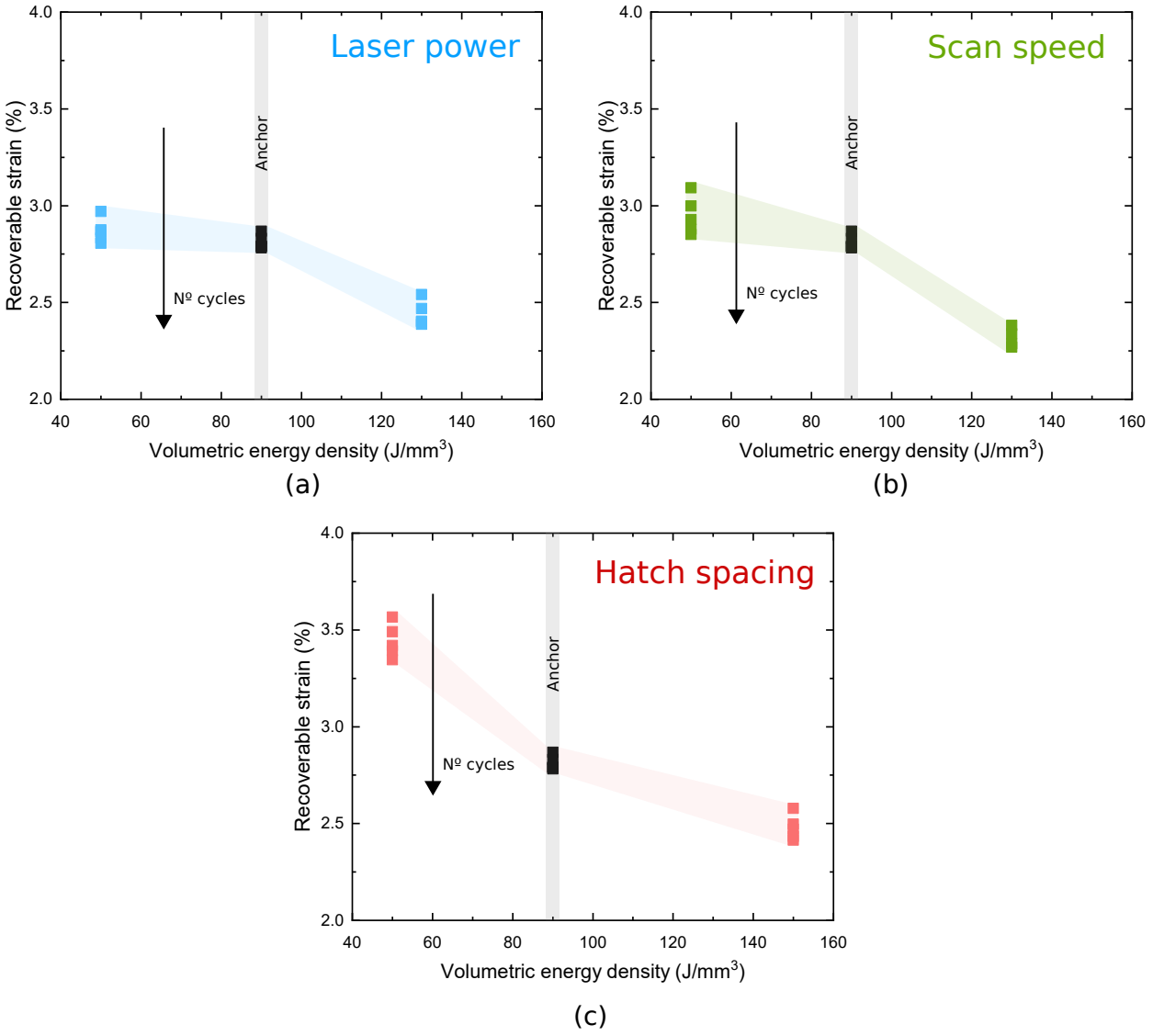


Figure 4.18: Recoverable strain in the different samples along the VED in the training test. The color code correspond to changes in laser power (blue), scanning speed (green) and hatch spacing (red). The anchor point is highlighted in black.

produce the actuation response. This can increase the complexity of the actuator due to the need of selective heating and control units [235, 236]. In these cases, what is used to control the actuation is the local variation of the stimulus (increase in temperature). Instead, one could replace this selective heating approach by changes in the transformational behaviour of the foundational alloy through variations in the LPBF conditions during manufacturing. For example, part´s regions that require actuation could be manufactured with low VED conditions (e.g., conditions P1, H5, V5) and part´s regions that require to act as static pieces could be fabricated with high VED conditions (e.g., conditions P4, V1 or H1). This would cause static regions to present a higher TT (e.g., T_2) than actuation regions (e.g., $T_1 < T_2$) as shown in results presented in Figure 4.11, leading in fact to a selective activation of the regions printed with the lower VED conditions when the temperature is set to $T_1 < T < T_2$. This approach could reduce the complexity of the actuator and enhance the reliability of the response due to less parts being involved in the system.

4.5 Conclusions

In this study, the influence of laser power, scanning speed and hatch spacing on the microstructure, phase transformation behavior, and thermomechanical properties of samples produced by LPBF with a nearly equiatomic NiTi powder (Ni 55.86 wt.%) was investigated. The results for samples with varying laser power, scanning speed, and hatch spacing demonstrate the extensive design space available in LPBF of nearly equiatomic NiTi alloys to achieve desired thermomechanical properties for specific applications. The main conclusions arising from this work are:

1. TTs increase with VED regardless of the individual process parameter that is changed (laser power, scanning speed or hatch spacing). The variation of the TTs is attributed mostly to the Ni loss during the LPBF process.

2. Ti_2Ni precipitates were found in the NiTi AM samples. The percentage of precipitates increased as the samples were printed with higher VEDs. This phenomenon is rationalized by the fact that higher VEDs are found to produce a greater evaporation of nickel, producing a more Ti-rich environment which can promote the formation of Ti_2Ni precipitates.

3. AM NiTi tensile samples exhibit recovery strains between 2-3.5% and plastic strains <1%. Samples fabricated with lower VEDs displayed lower TTs and higher strains, while samples with higher VEDs showed higher TTs and lower strains.

4. The presence of Ti_2Ni was found to significantly influence the thermomechanical properties of LPBF NiTi samples. Higher concentrations of Ti2Ni correlate with reduced recoverable and plastic strains, while lower concentrations of Ti_2Ni are associated with increased recoverable and plastic strains.

Chapter 5

Design of graded bulk NiTi SMA metamaterials by local change of processing conditions

5.1 Introduction

The design freedom using LPBF is clear after the investigations realized in the previous chapters. Understanding how process parameters affect the thermomechanical behavior of LPBF NiTi opens the door to the use of 4D printing concept [237]. This concept is characterized by "pre-programming" the shape morphing behavior of a deformable structure during its 3D manufacturing. Nowadays, most of the published works of the 4D printing materials are based on polymers [238, 239], but NiTi SMAs are considered to be candidate for 4D printed material due to their unique shape memory capabilities. As preliminary studied, Nematollahi *et al.* [28] printed a LPBF NiTi material using two different sets of process parameters. One half of the sample experienced SME behavior and the other half PE behavior. Ma *et al.* [27] used LPBF to fabricate a U-shaped sample with different structural responses between sides, altering the hatch spacing. Wang *et al.* [147] utilized two different sets of laser parameters to fabricate a layered functionally graded NiTi material with alternating martensitic and austenite phases, which exhibited a martensitic transformation temperature range of approximately 130 K and showed excellent damping characteristics. Yu *et al.* [57] fabricated austenite-martensite-austenite layered functionally graded NiTi utilizing the principle of rigid-flexible coupling. This approach led to enhanced compressive fracture strength and ductility relative to both martensitic and austenitic NiTi. The studies mentioned

above illustrate that the mechanical properties of NiTi alloy can be notably modified by the chemical composition and microstructural gradients induced by LPBF, presenting a promising tool for the creation of tailored materials.

It is clear that the LBPF NiTi alloys can be used as a 4D printed material, which advances the human desire to create materials with tailorable thermomechancal performance. However, most existing studies focus on simple layered graded NiTi samples, highlighting the need for a deeper investigation of how various gradient configurations and their mechanisms affect the actuation properties of LPBF NiTi materials. The challenge lies in the limited understanding of the non-linear phenomena induced by the LPBF process during the complex manufacturing of these graded structures, which significantly influence the overall thermomechanical behavior of the material. In this study, various NiTi samples were manufactured using local changes in the process parameters. Three graded NiTi samples were studied. All fabricated samples maintain a consistent ratio of area processed by each set of process parameters. The aim is to evaluate the individual behavior of the process parameters and their combined effects when they are incorporated into different graded NiTi samples. Furthermore, to have a deeper understanding of the non-linear effects arising from the interaction between the sets of processing parameters across different patterned geometries, thermal simulations of the LPBF process were conducted. These simulations offer valuable insights showing differences in the local temperature and the heat conduction across the patterned geometries during the LPBF process. In addition, structural simulations were performed on the patterned geometries to analyze the resulting stress fields between the areas processed with different laser parameters. These stress fields completely define the thermomechanical behavior after the training process, in the TWSME test.

5.2 Methodology

5.2.1 Design of experiments

To study the effect of graded processing conditions, different tensile samples were printed using three graded patterns (See Figure 5.1a). Three combinations of parameters were used: A-B, A-C and A-D (See table 5.1). The graded process parameters were selected from the previous study (see Chapter 4). All combinations used to manufacture the pattern geometries were composed by a low VED parameter (A) paired with a high VED parameter (B,C,D). The volumetric energy density (VED) was calculated using Equation (2.2). The NiTi powder

used in this chapter is the same as that used in Chapter 3. The same building conditions detailed in Chapter 3 were used to manufacture the samples.

Parameter ID	P (W)	v (mm/s)	h (µm)	t (µm)	VED (J/mm^3)
A	72	990	48	30	50
B	125	668	48	30	130
C	185	990	48	30	130
D	125	990	28	30	150

Table 5.1: LPBF processing parameters used in the manufacturing of NiTi samples.

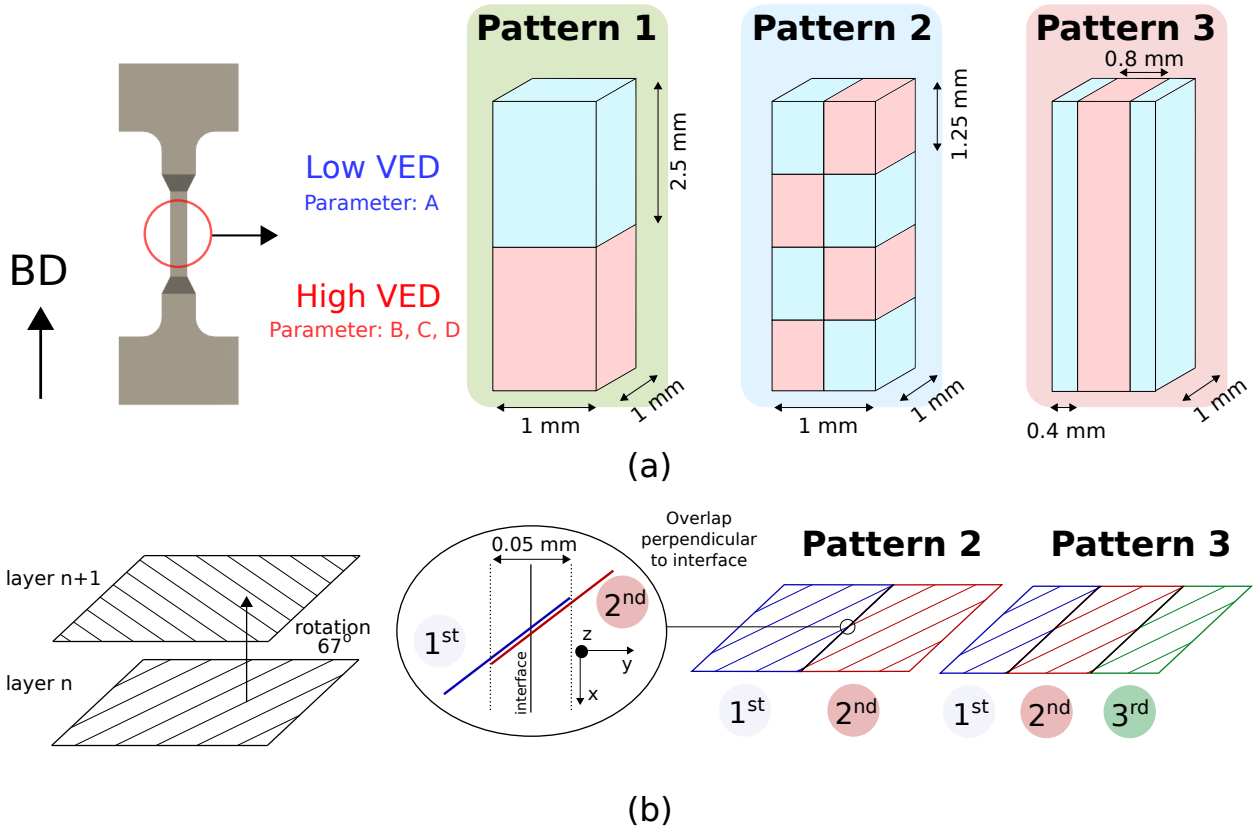


Figure 5.1: (a) Pattern geometries proposed in this study to the manufacture heterogeneous NiTi samples. (b) Scanning strategy employed during the manufacturing of the patterned geometries.

5.2.2 Material characterization

To study the grain morphology and for precipitate quantification, an Olympus GX53 optical microscope was employed to examine the samples using a magnification of 500x. The

metallographic preparation of the samples involved an initial grinding step using up to 1200-grit abrasive paper, followed by a polishing stage involving 9 μm and 3 μm diamond suspension. A final step with colloidal silica suspension was performed. The polished specimens were etched using a solution of H_2O (80%) + HNO_3 (15%) + HF (5%). A Hitachi S-3400N Scanning Electron Microscope (SEM) was employed for microstructural evaluation, using a magnification of 2500x, a beam voltage of 15 kV, and high image contrast.

5.2.3 Thermomechanical testing

Thermomechanical tests were performed in an universal mechanical testing machine equipped with a climate chamber. A strain rate of 10^{-2} s^{-1} was used. The strain of the samples was measured by Digital Imaging Correlation (DIC). The samples were heated and cooled at a rate of 10 K/min. Figure 4.2b indicates how the training test was performed. The test temperature started at 400 K and the sample was loaded at 200 MPa. Five thermal cycles were performed, maintaining the sample loaded at the same stress level. Once training was complete, the samples were unloaded (0 MPa) and subjected to a complete thermal cycle (TWSME). After the training and TWSME tests, the recoverable and plastic strains were measured according to Figure 4.1b.

5.2.4 Computational approaches

LPBF thermal modeling

To gain deeper insight into the non-linear effects resulting from the interplay of processing parameters across the different patterned geometries, thermal simulations of the LPBF manufacturing process were performed. These simulations provide insightful results on the differences between patterns in the amount of time the material is at molten state and high temperature. In order to recreate conditions of the LPBF process, a simplified heat conduction model with appropriate boundary conditions and flux loads was used based from previous work in the literature [240, 241]. The base material is thermally modeled as a solid substrate, the top layer is considered as a homogeneous continuum solid having properties of powder, and the laser beam occurs at the top surface of the powder layer and travels along the x-axis with a constant speed. The following points have been addressed in the thermal model:

- **Heat transfer equations:** During the LPBF process, the temperature distribution satisfies the 3D heat transport equation:

$$\rho c_p \frac{\partial T}{\partial t} = k\nabla^2 T + q \tag{5.1}$$

where ρ is the density, c_p is the specific heat capacity, T the is temperature, k is the thermal conductivity, and q is the absorbed heat flux. The radiation between the top surface of the powder layer and the environment is given by equation:

$$-k\frac{\partial T}{\partial n} = \varepsilon\sigma\left(T^4 - T_e^4\right) \tag{5.2}$$

where n represents the normal direction to the surface, ε is the emissivity, σ is the Stefan Boltzmann constant and T_e is the environment temperature. The enthalpy is represented as:

$$H(T) = \int c\, dT + L_f f \tag{5.3}$$

with the inclusion of latent heat of fusion (L_f) for a material undergoing phase change where f is the volumetric fraction of liquid, representing the fraction of material molten material. Finally, this function describing the phase transformation in terms of temperature is:

$$f = \begin{cases} 0 & T < T_S \\ \frac{T-T_S}{T_L-T_S} & T_S \leq T \leq T_L \\ 1 & T > T_L \end{cases} \tag{5.4}$$

being T_S and T_L solidus and liquidus temperatures respectively.

- **Heat source equations**: A Gaussian heat source model was used to represent the flux produced by the laser during the LPBF process with a Gaussian distribution and parabolically decaying along the beam penetration direction. This is mathematically represented as:

$$q(x, y, z) = \eta\frac{H_S I_Z}{S} \tag{5.5}$$

being:

$$I_Z = \frac{1}{0.75}\left(-2.25\left(\frac{z}{S}\right)^2 + 1.5\left(\frac{z}{S}\right) + 0.75\right) \tag{5.6}$$

$$H_S = \frac{2P}{\pi\phi_E^2} exp\left(-\frac{2\left((x-x_0)^2+(y-y_0)^2\right)}{\phi_E^2}\right) \tag{5.7}$$

where η is the laser beam abortion efficiency, H_S represents the Gaussian distribution, I_Z is the parabolic decaying, S is the penetration depth, P is the power of the laser beam, Φ_E is the beam diameter and x_0 and y_0 are the position of the heat source in the x-y plane.

- **Material properties**: The material properties considered for the thermal simulation are shown in Figure 5.2. During the LPBF process, there is a rapid change in temperature, so the properties of the solid and powder materials were considered as functions of the temperature. The thermal properties of powder differ from those of a solid; thus, the transition in the material stage from a powder to a liquid and subsequently to a solid will also result in changes in the properties of the material. The temperature dependent material properties for solid and powder were taken from previous studies in the literature using NiTi alloys [242, 243] (see Figure 5.2a-c). The latent heat of fusion and the transition temperatures were extracted from [244, 245] (see Figure 5.2d). Furthermore additional model parameters were used, as emissivity and absorption efficiency extracted from [246, 247]. The selected values of beam diameter, penetration depth and laser power will be detailed in the next section.

Thermal finite element simulation

The LPBF process was investigated using ABAQUS 2023/Standard software package [248]. The thermal modeling configuration with the boundary conditions imposed is shown in Figure 5.3a. The FE model was meshed with 3D solid elements type DC3D8. The FE model consists of a solid substrate with dimensions of 2 mm x 0.8 mm x 0.53 mm and above the substrate, there is one layer of powder, of 0.03 mm thickness. The temperature gradients are expected to be very high, so for the powder, cubic elements of 0.015 mm x 0.015 mm were used. In order to improve computational efficiency, the element size of the substrate was increased in the z direction (up to 0.025 mm). A thermal boundary condition of a constant temperature of 300 K was applied to the bottom surface of the substrate ($z = 0$ mm). Radiation boundary conditions were applied to the top surface of the powder layer using an emissivity of 0.7 (see Figure 5.2d).

Six different cases were simulated as indicated in Figure 5.3b. In all cases, the laser beam begins on the left and travels along the x-axis with a constant speed (990 mm/s). In order to

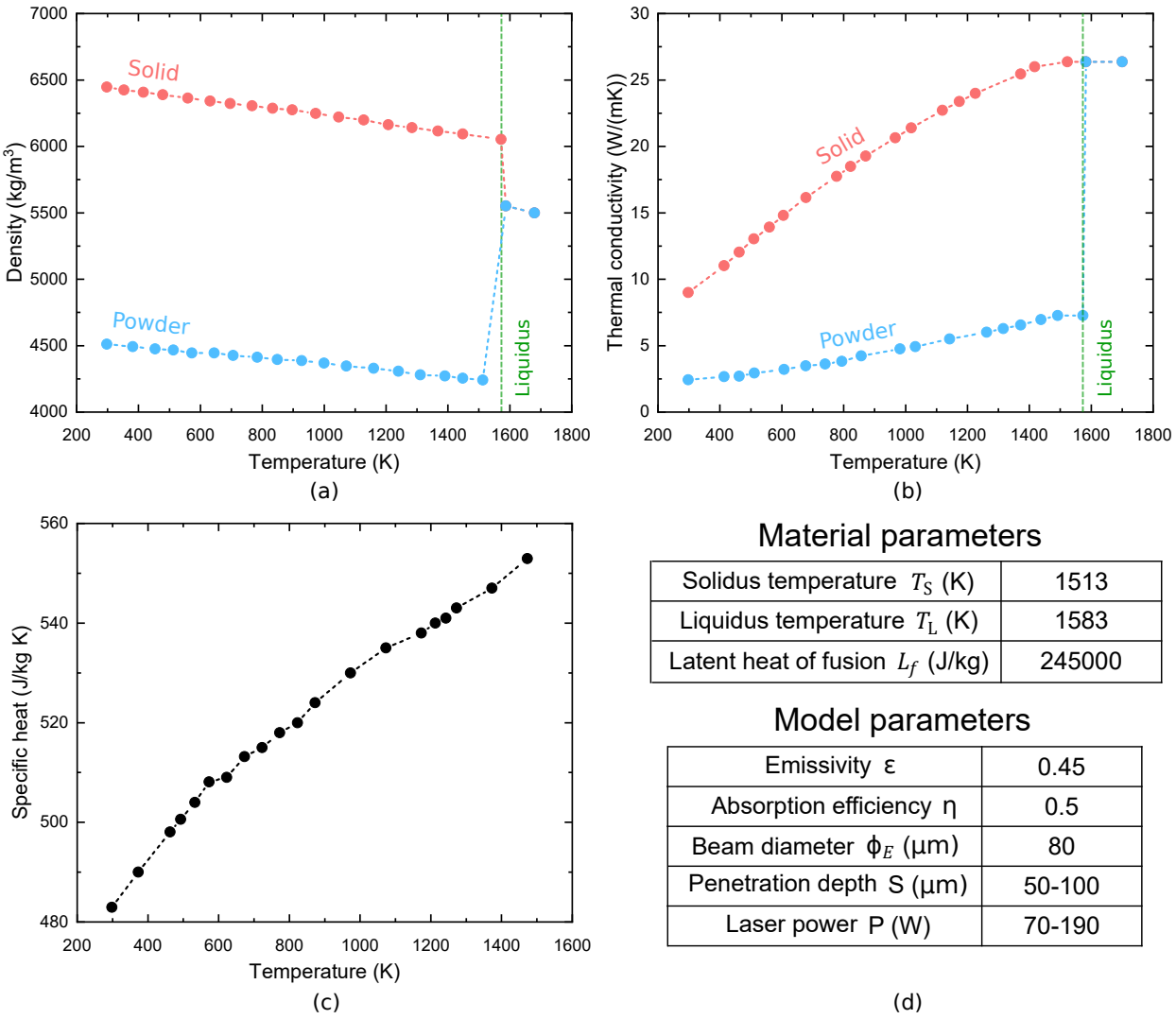


Figure 5.2: Temperature dependent material properties of solid and powder NiTi. (a) Density [242], (b) thermal conductivity [243], (c) specific heat [243] and (d) solidus and liquidus temperatures [244], latent heat of fusion [245], emissivity [246], absorption efficiency [247], beam diameter, penetration depth and laser power .

reduce the number of simulations, the low VED parameter selected is parameter A and the high VED parameter is parameter C (see Table 5.1). The beam diameter used and the laser powers are the same values employed during the manufacturing of the samples. The values used in the simulations for penetration depth in the low and high VED were obtained from the experimental results. The following cases were simulated:

- **Cases L and H**: In these cases a single laser track is simulated using the low VED set of processing parameters (Case 1) or the high VED set of processing parameters (Case 2). The laser beam travels 1 mm until it is stopped.
- **Cases L⊥H and H⊥L**: These cases simulate the effect of the overlapping from a low VED laser track to a high VED (Case 3) laser track and vice versa (Case 4). As observed in Figure 5.1, the second track does not begin when the first track ends. A realistic waiting time between the end of the first laser track and the beginning of the second one is set. This time simulates the rest of the laser path spent printing all the tracks until reaching the continuation of the previously simulated segment. Similarly to previous cases, the second laser will stop when the total laser track measures 1 mm.
- **Cases L∠H and H∠L**: These cases are equal to Cases 3 and 4. The only difference is in the total distance of the laser tracks. This distance will be the maximum possible during the manufacturing of a 1 mm x 1 mm section sample. In addition, the overlapping region will be higher than in Cases 3 and 4.

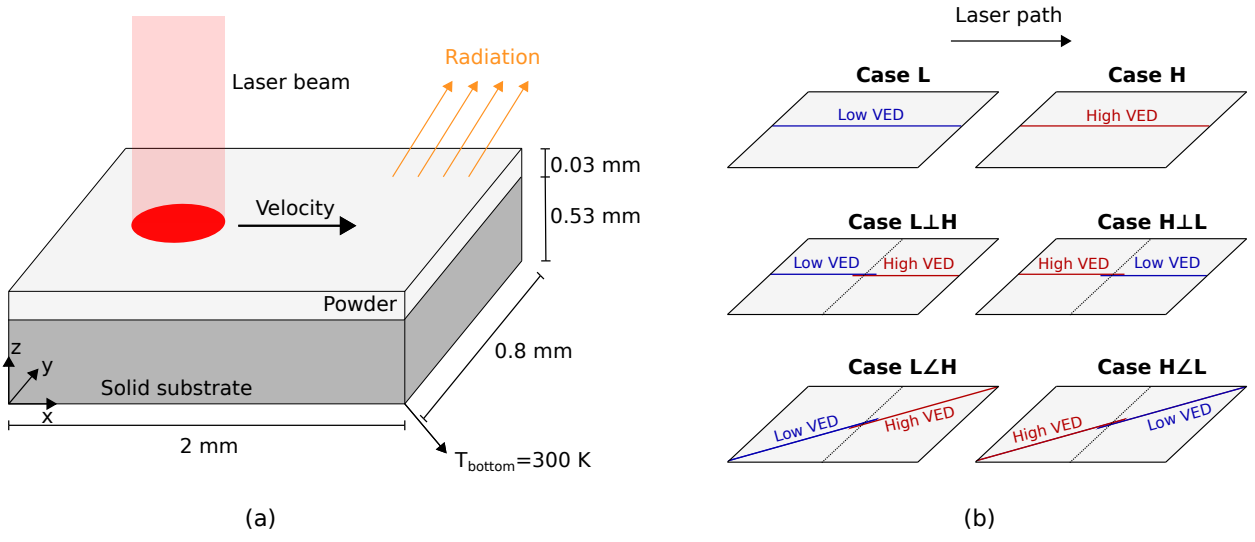


Figure 5.3: (a) Thermal modeling configuration of the SLM process with boundary conditions. (b) Overview of the FE simulated cases studied on this work.

5.3 Results

5.4 Results and discussion

5.4.1 Microstructural analysis

Grain structure and porosity

Figure 5.4 presents the microstructural analysis of the patterned samples produced in this study. The white dotted lines indicate the interfaces between different processing parameters in the patterned samples. For the shake of comparison, the microstructure of monoparameter samples fabricated with processing parameters A to D is presented. This was the focus of the previous study (see Chapter 4).

The microstructures of the samples printed with Pattern 1, show a transition zone at the interface of two regions with different microstructural features. It can be observed that the region manufactured with low VED exhibits smaller grains with no preferential growth direction, while those produced using high VED parameters (B, C, and D) develop larger columnar grains oriented along the laser direction. This difference is attributed to the deeper and wider melt pool generated by the high VED process parameters [249]. This is consistent with the observations in monoparameter samples. The width of this transition zone between the low VED and high VED regions varies from $\sim$ 50 to 150 μ m depending on the processing parameters. For the case of the samples printed with Pattern 2, the high VED region (B,C,D) shows larger columnar grains and some porosity, while the low VED region (on the left) exhibits smaller melt pools and low porosity levels. The interface is less pronounced in this pattern compared to the samples manufactured using the first pattern geometry. Finally, the samples printed with Pattern 3 show the microstructure of larger columnar grains in the high VED regions as in previous cases, while smaller grains are found again in the low VED regions, consistent again with the microstructures observed in the homogeneous samples.

In terms of porosity, regions fabricated with parameters B, C and D (high VED) show the presence of pores, while no pores or reduced number of them are observed in those produced using the process parameter A. This difference might be produced by the method used to achieve high VED. For parameters B and C there is a change of laser power and scan speed with respect to baseline A, respectively, affecting the laser input along the laser path. However, for the case of parameter D, the linear energy input of the laser along the track is maintained,

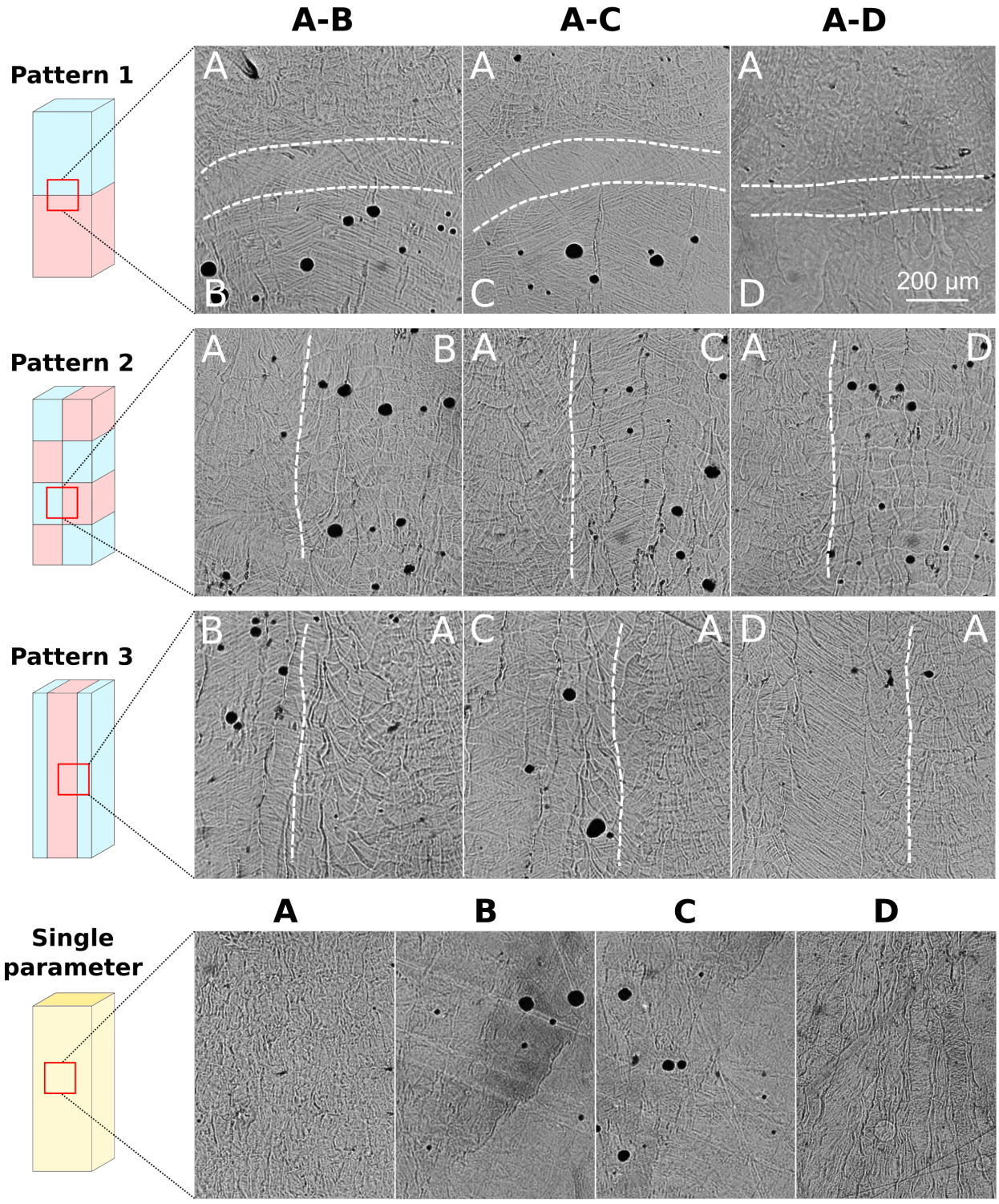


Figure 5.4: Microstructure of the patterned samples and monoparameter samples manufactured. White dotted line represents the interface between the different processing parameter used.

and the higher VED is achieved by reducing the hatch spacing (thus making the laser track closer together). The previous work on the same alloy (see Chapter 4) established that laser power and scan speed have a greater influence on porosity than hatch spacing due to the correlation effect between porosity and linear energy density (LED). The higher the LED, the higher the resultant pores obtained. This is now confirmed in this work for the case of heterogeneous materials, where independently of the selected patterns, each region with a given parameter set presents the same porosity phenomena as homogeneous samples printed with the same parameter set.

Sub-grain structure: precipitate distribution

To address the microstructural changes at the subgrain level, SEM microscopy of each pattern has been performed. As the grain level shows small differences between the parameter set combination, the combination of parameter A-B was selected as representative for the study of the subgrain microstructural changes. Figure 5.5 illustrates the microstructures in selected representative regions of each pattern. Specific regions are selected to study the microstructures of each parameter set within the pattern.

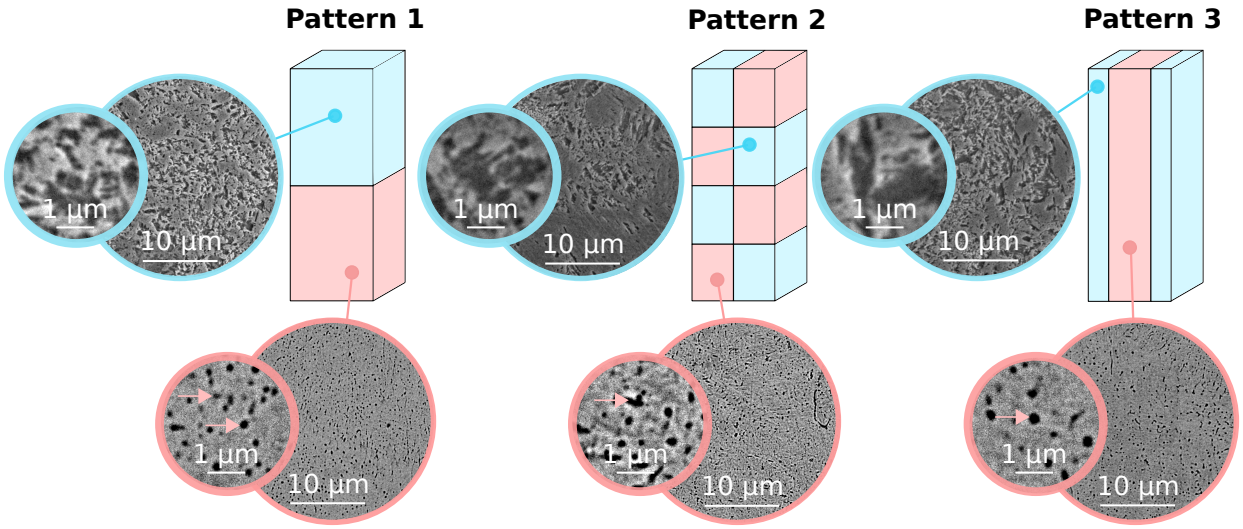


Figure 5.5: Microstructures of the different regions in the patterned samples.

Two different microstructures can be observed corresponding to the two different regions (high VED and low VED). The regions manufactured with low VED display the absence of precipitates and just martensite can be inferred. However, for the high VED regions (manufactured with parameter B), a fine distribution of precipitates is observed (indicated using red arrows). These precipitates have been identified in previous studies as Ti_2Ni [194,

206, 207]. The appearance of Ti_2Ni is associated with a higher evaporation of Ni during the LPBF process. Nickel has a higher tendency to evaporate during the LPBF process due to its higher vapor pressure compared to titanium [199]. Higher evaporation of Ni, reduced the Ni content of the matrix, thus displacing the alloy composition in the equilibrium of phases diagram, leading to oversaturation of titanium and therefore a precipitation of the Ti-rich precipitate Ti_2Ni [50]. The implications of these precipitates are multiple [194, 216, 217], e.g., known to affect the transformation behavior as they serve as obstacles for phase growth (they do not undergo phase transformation). The effect on each aspect of the transformation (TTs, recoverable strain or plastic strain), will be discussed in the following section.

Despite the different thermal histories of each pattern, Ti_2Ni precipitates and martensite plates found in high and low VED regions respectively, do not show any difference between patterns suggesting that the same emergence process has been followed in all areas, as observed in Figure 5.5. The precipitated area extends beyond the theoretical boundary of the region printed with high VED parameters. This will be further rationalized in the following section, supported by thermal simulations, but it can be anticipated that the overlapping of laser tracks in the vertical interfaces (see Figure 5.1) increases the thermal fingerprint of the laser and the Ni evaporation at the boundary. This results in regions within the low VED boundaries but with precipitates of Ti_2Ni due to the thermal effect of the boundary.

5.4.2 Homogenized macro-thermomechanical behavior

The thermomechancial behavior of the material printed with the different patterns is presented in this section. As indicated before, the performed tests consist on an initial training step composed of thermal cycles under a constant load and a second step of thermal cycling without stress to evaluate the TWSME of the alloy. Figure 5.6 shows the training (continuous line) and TWSME (dotted lines) steps of these tests in the designed patterns for different combinations of parameters. Green, blue and red curves represent samples fabricated with Patterns 1, 2 and 3 respectively. The first, second and third columns of the figure display the combinations of parameters A-B, A-C and A-D used to manufacture the samples. In all cases, the strain-temperature curves exhibit a reduction in strain magnitude and undergo a slight shift downward and to the left over the cycles. Furthermore, the TWSME curves (zero load) exhibit a shorter strain cycle, with the entire cycle shifted leftwards compared to the training cycles. Furthermore, the strain-temperature curves from Pattern 3 show narrower cycles than those of Patterns 2 and 3. In the following sections, an in-depth analysis of the phase transformation, recoverable and plastic strain is presented.

All patterns manufactured have the same volume of high and low VED parameters (see Figure 5.1). Despite that, different thermomechanical behaviors are found in the patterned samples. In the following section, the different factors affecting the training and TWSME properties of the patterns are presented.

Transformation temperatures

The transformation temperatures M_f and A_s of the different patterns have been extracted from Figure 5.6. These are presented in Figure 5.7 for both the training cycles and the TWSME step. For the sake of comparison, the results of the monoparameter samples manufactured with the same process parameters set extracted from the previous study (see Chapter 4) are also shown (dotted lines). They found that samples produced with high VED (process parameters B, C, and D) exhibit the highest values of both M_f and A_s TTs, while the sample manufactured with low VED (process parameter A) presents the opposite behavior (see Figure 5.7).

In regards to the training step (first column), As present similar value ranges for Patterns 1 (∼375–385K) and 2 (∼378–388K), while samples manufactured using Pattern 3 exhibit lower values of this transformation temperature (∼365–375K) for all parameter combinations. Regarding the M_f temperature, Patterns 2 and 3 display a similar value range (∼338–345K), while Pattern 1 shows lower values (∼332–335) for all parameter combinations. Notably, all patterned M_f results fall between those of the monoparameter samples fabricated using low and high VEDs except for the case of A_s in Pattern 3. In addition, a general decrease trend in the TTs is observed for each sample as the number of thermomechanical cycles increases.

In terms of the TWSME response (second column), a more consistent trend is observed across all combinations of process parameters. The TTs of the patterned samples fall between these two extremes (except for Pattern 1 A-C, which slightly falls below the low VED. For Mf, pattern 3 shows the highest values (∼325–330K), followed by Pattern 2 (∼322–328 K) and Pattern 1 (∼315–320K). In contrast, a different trend is observed for As, where samples produced with pattern 2 reach the highest values (∼362–366K), followed by those manufactured with Pattern 3 (∼352–354K) and Pattern 1 (∼350–354K).

It is well known in the literature that the modification of the processing parameters affect the TTs of the LPBF NiTi material, mostly by two factors: the change in the Ni/Ti ratio and the presence of precipitation structures [194, 144]. Previous studies [194] have shown that samples manufactured using high VED parameters, present higher evaporation of Ni, thus lowering the Ni/Ti ratios and producing the precipitation of Ti_2Ni precipiates, as confirmed in Section

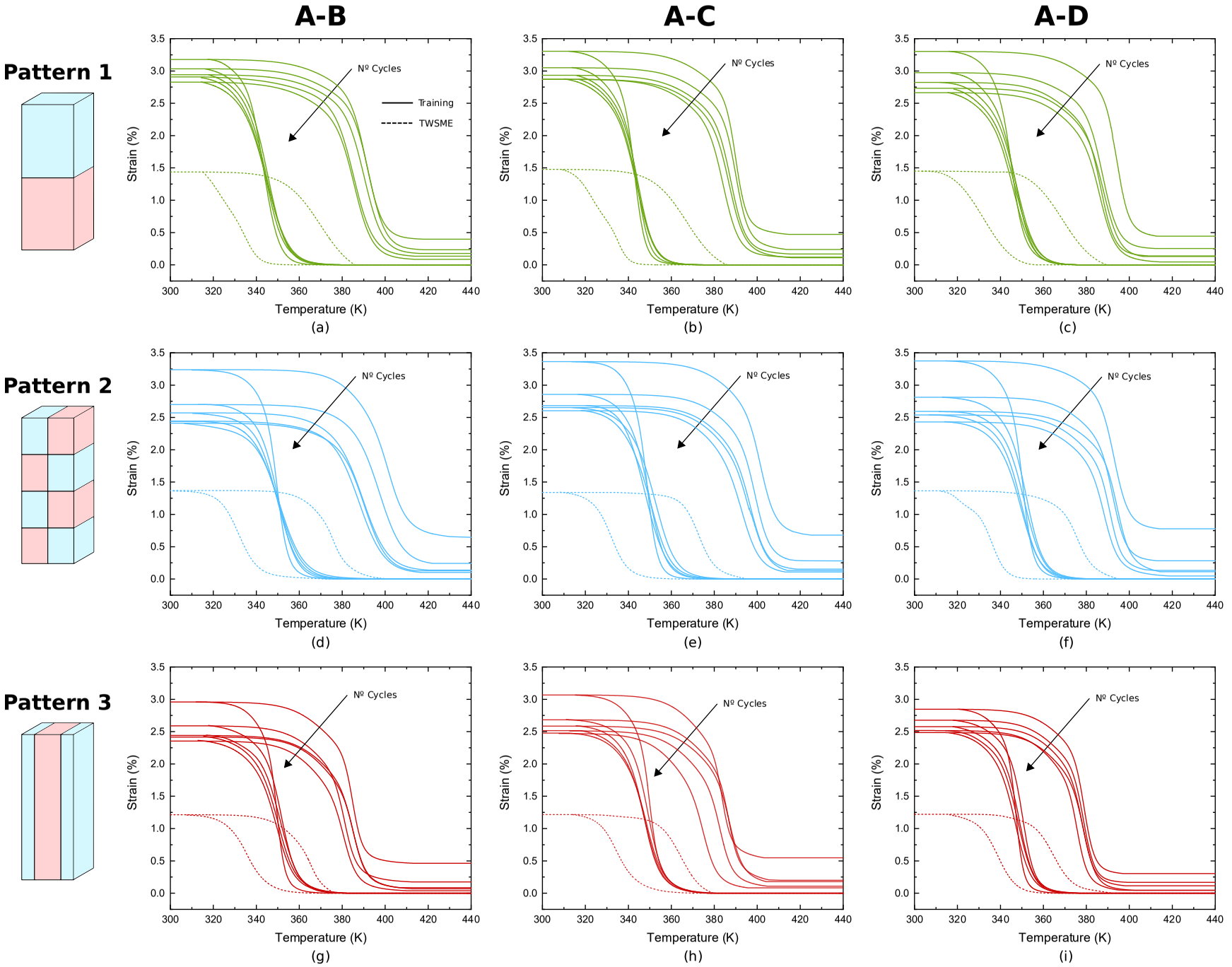


Figure 5.6: Strain-temperature curves of the LPBF NiTi samples with patterns extracted from training (continuous lines) and TWSME (dotted lines) tests. First, second and third rows correspond to samples fabricated using Patterns 1, 2 and 3 respectively. First, second and third columns correspond to the combinations A-B, A-C and A-D of process parameters used to manufacture each pattern respectively.

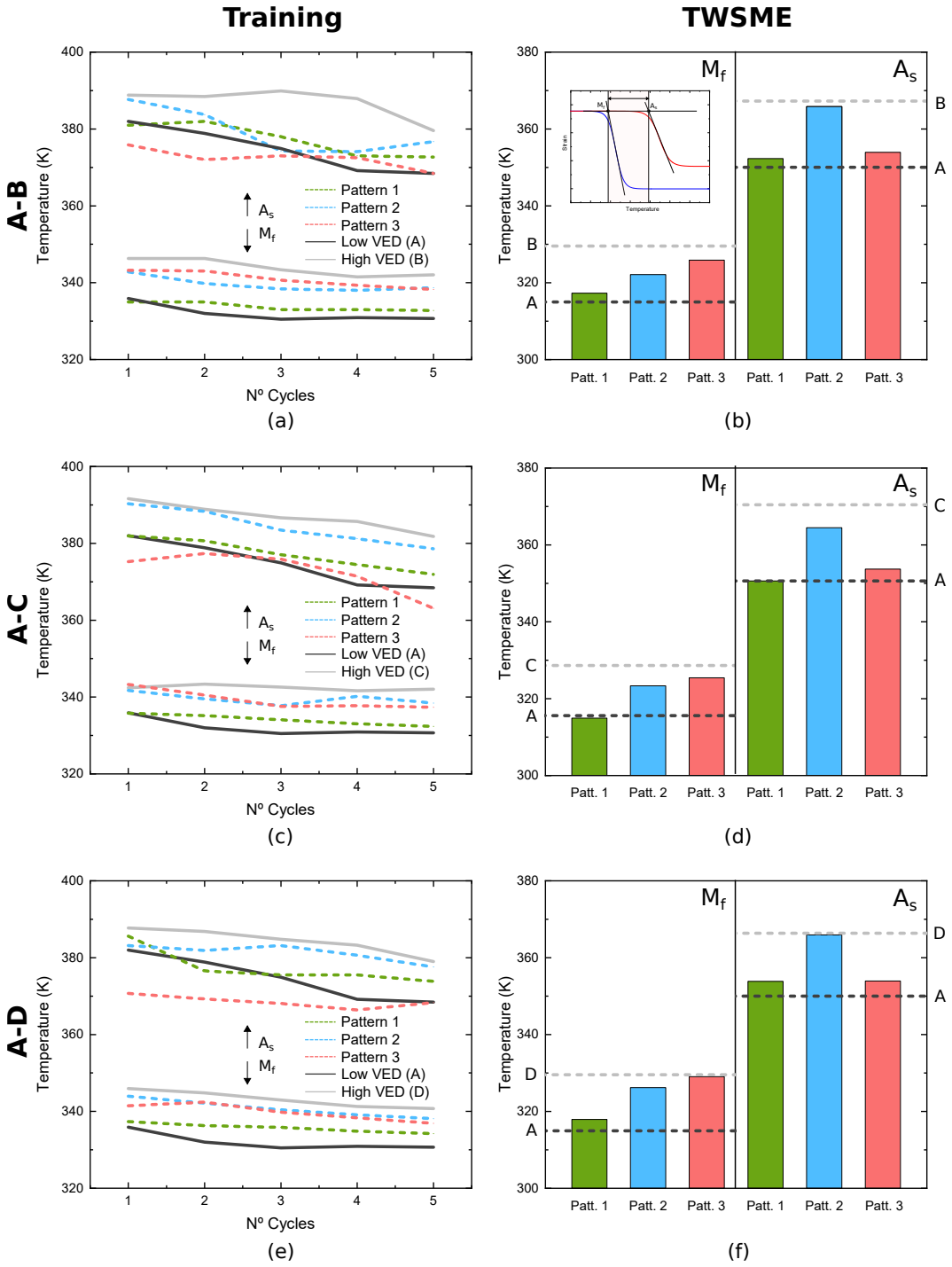


Figure 5.7: (a),(c),(e) represent the TTs of each thermomechanical cycle showing the martensite transformation finish temperature (M_f) and the austenite start transformation temperature (A_s). (b),(d),(f) predsent the M_f and A_s temperatures in the TWSME test. (a)-(b), (c)-(d) and (e)-(f) display the results of the LPBF samples manufactured with combinations of parameters A-B, A-C and A-D respectively. Dotted black and gray lines represent the results of the homogeneous samples of each combination of process parameter used to manufacture the patterned samples. The results for monoparameter homogeneous samples of the same alloy are presented for comparison.

5.4.1 of the current work. It is extensively reported in the literature that reducing the Ni/Ti ratio in a NiTi alloy leads to higher TTs, [250, 251, 194]. This would explain the differences in response between different regions of the patterns, but to understand the difference in the homogenized response and TTs between patterns, special attention should be put on the interfaces between regions.

In patterned samples, vertical interfaces exhibit overlap within the laser tracks, while horizontal interfaces do not (see Figure 5.1). Assuming a laser spot diameter of 80 µm and a laser track overlapping of 50 µm, means that a localized region of about 90 µm near the vertical interfaces undergoes local heating twice. In these areas, Ni evaporation must be higher [252], leading to a reduction in the total nickel content, which would typically result in an increase in TTs. This will be further rationalized in Section 5.4.3 by means of thermal simulations. This reheating effect is less pronounced for the case of the horizontal interfaces, as no overlapping is present. So, as the number of vertical interfaces is higher, the regions where Ni evaporation is increased should be higher, and therefore the TTs should increase. Based on this, Pattern 3 exhibits 10 mm^2 of vertical interfaces followed by Pattern 2 with 5 mm^2 and Pattern 1 with no vertical interface area. Observing the results of Figure 5.7, this expected trend is observed in the experimental results in one observed the overall results for each pattern, except for the case of Pattern 3 A_s. In this case, the temperature histeresys of the cycle (A_s-M_f) is reduced also when compared to the rest of conditions. The discrepancy for this case suggests that more complex effects take part during the phase transformation of the patterned samples and not only the overall Ni/Ti ratio explains the changes in TTs as for the case of previous studies on monoparameter samples [194, 200, 20, 201].

Recoverable and plastic strain

As for the TTs, the recoverable (ε_{rec}) and plastic ($\varepsilon_{plast)}$) strain have been extracted from the experimental curves in 5.6. The values of ε_{rec} and $\varepsilon_{plast)}$ are presented in Figure 5.8 for both the training step (as a function of the trainning cycle) and for the TWSME (in this case just the ε_{rec} is calculated) As in TTs, for the shake of scientific comparison, the results from the previous study (see Chapter 4) on homogeneous samples with parameter sets A, B, C and D are presented as dotted lines.

For the case of the recoverable strains of the patterned and homogeneous samples along the thermomechanical cycles (first column), the trend appears to be consistent across all the Patterns, regardless of the combinations of parameters used in their manufacture. Samples manufactured using Pattern 1 have the highest recoverable strains (∼2.75-2.90%) while samples

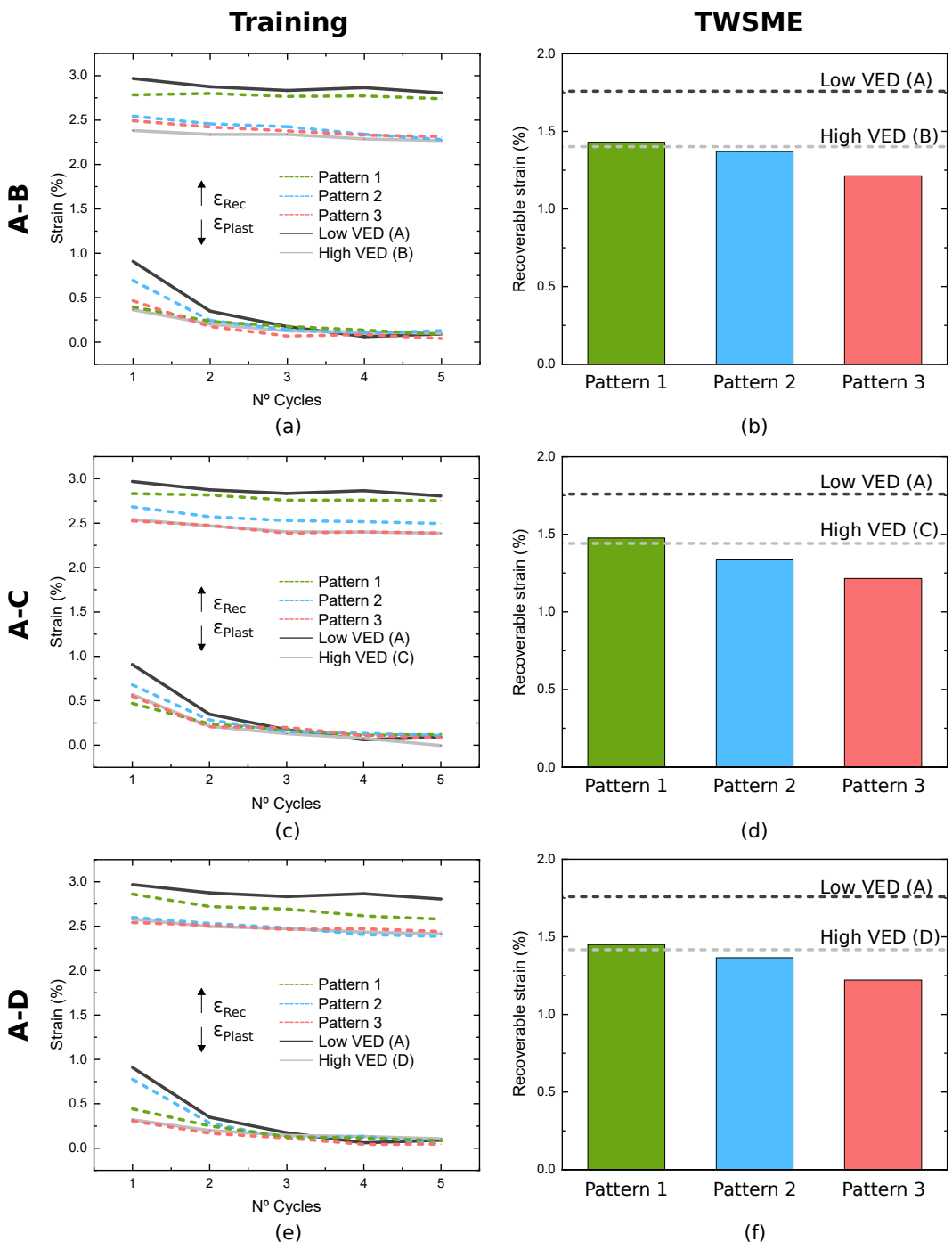


Figure 5.8: (a),(c),(e) show recoverable and plastic strains along the thermomechanical cycles of the training. (b),(d),(f) represent the recovery strain obtained from the TWSME test of each patterned geometry. (a)-(b), (c)-(d) and (e)-(f) display the results of the LPBF samples manufactured with combinations of parameters A-B, A-C and A-D respectively. Dotted black and gray lines represent the results of the homogeneous samples of each combination of process parameter used to manufacture the patterned samples. The results for monoparameter homogeneous samples of the same alloy are presented for comparison.

manufactured using Pattern 2 and 3 display lower recoverable strains (∼2.4-2.6%). This is in accordance with the previous results on homogeneous samples (see Chapter 4), where samples manufactured with high VED conditions (process parameters B, C, and D) demonstrate lower recoverable strains (∼2.4–2.6%), which are similar to those achieved in patterned geometries using patterns 2 and 3. In contrast, homogeneous samples produced under low VED conditions (process parameter A) achieve higher recoverable strains (∼2.8–3.0%), exceeding those observed for all graded samples, regardless of the pattern used. Lower recoverable strains are produced in material printed with high VED (B, C and D) due to the presence of Ti_2Ni, which restricts the transformation strain [219, 225, 194]. It is interesting to note that the recoverable strain of Pattern 2 and Pattern 3 fall closer to samples printed with higher VEDs while Pattern 1 achieves for most cases similar values of recoverable strains to the homogeneous samples printed with lower VED. This can be explained by the structure of the pattern. For the case of Pattern 1, as the sample undergoes transformation, as both regions are localized "in series" with respect to the loading direction, the sample behaves as two independent materials in which each region undergoes deformation when dictated by the local microstructure. However, for the case of the other two patterns in which the regions are not coupled "in series" along the loading direction the overall homogenized recoverable strain is controlled by the region with the lowest recoverable strain. This can be produced by the necessity of a continuous deformation along the sample, as the material regions need to adapt their deformation to the contiguous regions. In addition, for all of the LPBF NiTi samples studied, a slight decrease in the recoverable strain during the training step can be observed as the number of thermomechanical cycles increases. The degradation of recoverable strain with the number of cycles has also been reported in other studies and is attributed to the accumulation of retained martensite [222, 223].

In terms of plastic strains along the thermomechanical cycles (first column), the samples manufactured with pattern 2 show higher values (∼ 0.55-0.85 %) than samples manufactured using patterns 1 and 3 (∼ 0.30-0.55) in the first thermomechanical cycle. The plastic strains of the patterned samples in the first cycle spread between the values obtained for high VED and low VED material samples. LPBF with higher VED implies higher thermal gradients during the LPBF proces, producing also higher thermal stresses in the material that promote dislocation formation as the VED used increases [227, 228, 229]. The higher amount of dislocations makes slip deformation more difficult, so higher local stresses are needed to create dislocation slip during the first cycle [224]. Therefore, the material manufactured with high VED parameters (B, C, D) present lower levels of plastic deformation in the first cycle compared to the sample manufactured with the low VED parameter (A). It can be observed

in Figure 5.8 plastic strains decrease along thermomechanical cycles in all samples, with saturation of plastic strain reached by the third cycle. During phase transformation, strain incompatibilities in the austenite-martensite interface induce local stresses that exceed the plastic yield stress triggering the dislocation slip [224]. During propagation of the austenite-martensite interfaces, dislocations spread through the transformed regions. Upon completion of the reverse transformation, a significant number of dislocations remain, leading to a residual strain (plastic strain). As a result of plastic hardening, slip deformation progressively becomes more constrained along the cycles up to stabilization of the thermomechanical response (saturation) [224].

For the case of recoverable strains in the TWSME part of the test (second column), a trend similar to that observed in training tests is identified. Among the patterned geometries, Pattern 1 exhibits the highest recoverable strains (∼1.40–1.45%), followed by Pattern 2 (∼1.30–1.40%) and Pattern 3 (∼1.20–1.25%). However, unlike the training results, the recoverable strains of the patterned samples do not lay down between the recoverable strains of the homogeneous samples.

As reported in previous studies [215, 253], the recoverable strain in the absence of stress is controlled by dislocations and defects created during the training procedure. During the TWSME, the martensite plates disappear when the sample changes to fully austenite phase, but during the next thermal cycle, the same martensite plates are created to accommodate the internal stress generated by these defects that induce macroscopic strain. However, for the case of these patterned materials, the effect of heterogeneous transformation produces a complex stress state, which can produce different internal defects and, therefore, preferential appearance of other certain martensite variants, thereby preventing the formation of preferential martensite variants and reducing the TWSME. This will be further rationalized in Section 5.4.3 of this work.

Hysteresis behavior

Similarly to the analysis of the transformation properties, the combination of two sets of process parameters produced different results in the hysteresis behavior depending on the patterned geometry manufactured. Figure 5.9 shows the area inside the TWSME cycles for all patterned geometries. It can be observed how in Patterns 1 and 2 the area falls down between the areas of the monoparameters samples while in Pattern 3 this area is below the area of the monoparameter high VED sample. As explained in the previous section (Section 5.4.2) the complex internal stresses promote the formation of different internal defects, and thus formed

other martensite variants during the TWSME. This leads to distinct macroscopic behavior between homogeneous monoparameter samples and patterned geometries. Specifically, Pattern 3 exhibits a significantly smaller area while also having the largest area of vertical interfaces, which are the main responsible for increased internal defects during manufacturing. This probably explains why its hysteresis behavior is decreased compared to Patterns 1 and 2.

5.4.3 Local micro-thermomechanical behavior

In this section, a focus is placed on the phenomena occurring at the pattern interfaces during the LPBF and its implication on the microstructure and thermomechanical behavior observed in the previous section. The focus is placed on the horizontal interfaces, where the change in processing parameters occurs between powder layers. Then the phenomena occurring at the vertical interfaces where two distinct laser tracks overlap during the LPBF is presented.

Interlayer interfaces (Pattern 1)

In this section, the physical phenomena that occur during LPBF associated with horizontal interfaces is studied. These interfaces are composed by two layers of powder, the bottom one manufactured with high VED parameters (B, C or D) and the top one manufactured with low VED parameters (A), see Figure 5.10. During the manufacturing of NiTi layer by layer, it is well known that LPBF generally produces elongated grains along the building direction that in some cases show epitaxial growth over the grains of previous building layers, especially for higher VED parameters [254, 255]. This leads to larger elongated grains, with a vertical length exceeding the layer thickness [254, 255]. This grain structure could be inferred in the microstructural study of Section 5.4.1. However, the analysis of the austenite microstructure is not possible at RT as by observing the TTs of the material in Figure 5.7, NiTi martensite phase should be present at RT.

In any case, the austenite microstructure could be inferred by looking at the etched micrographs of Figure 5.10 showing a schematic of grain growth during the LPBF process. During LPBF, the laser creates a molten pool and causes a thermal gradient as shown in Figure 5.10a. During solidification, the grains grow toward the thermal gradient where grains of a lot orientations are expected. During the subsequent laser pass, some grains are remelted, leading to the development of a strong texture characterized by large columnar grains (see Figure 5.10), especially when large VEDs are used.

For the case of Pattern 1, the initial zone printed with high VED, leads to larger thermal

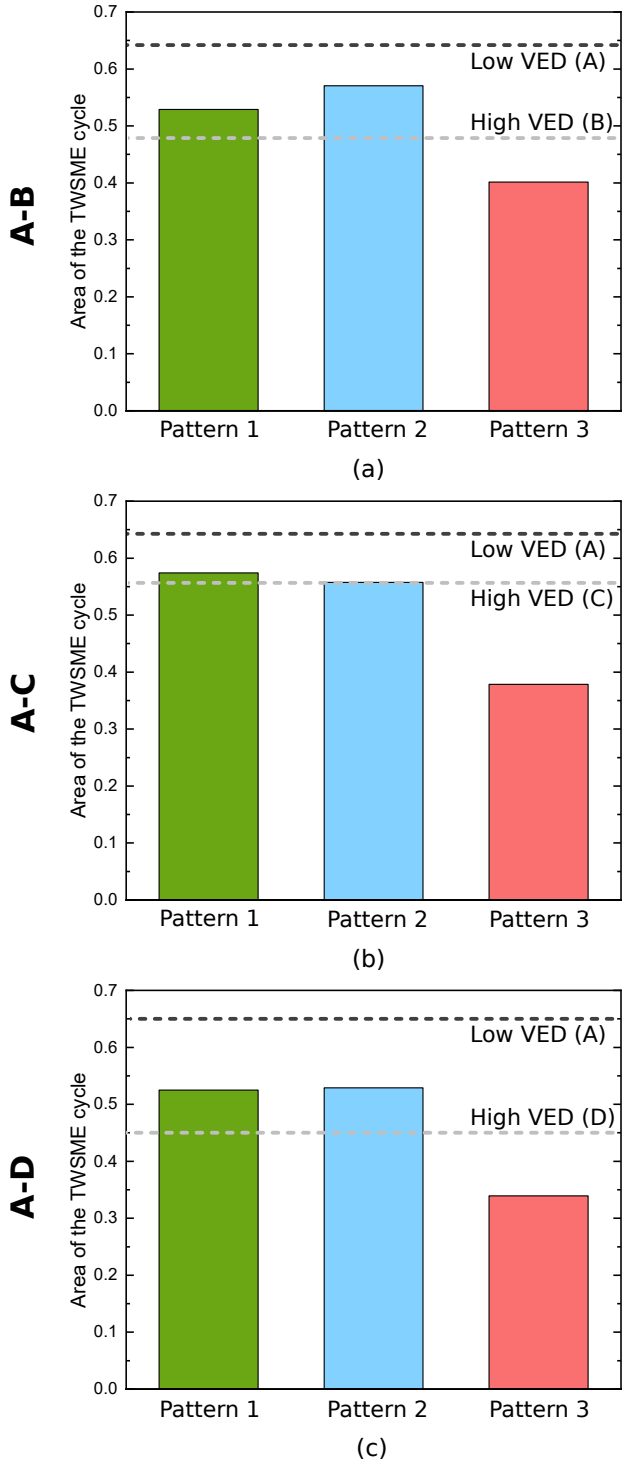


Figure 5.9: Area inside the TWSME cycles for each patterned sample. The results of the monoparameter samples have been extracted from the previous work (see Chapter 4) .

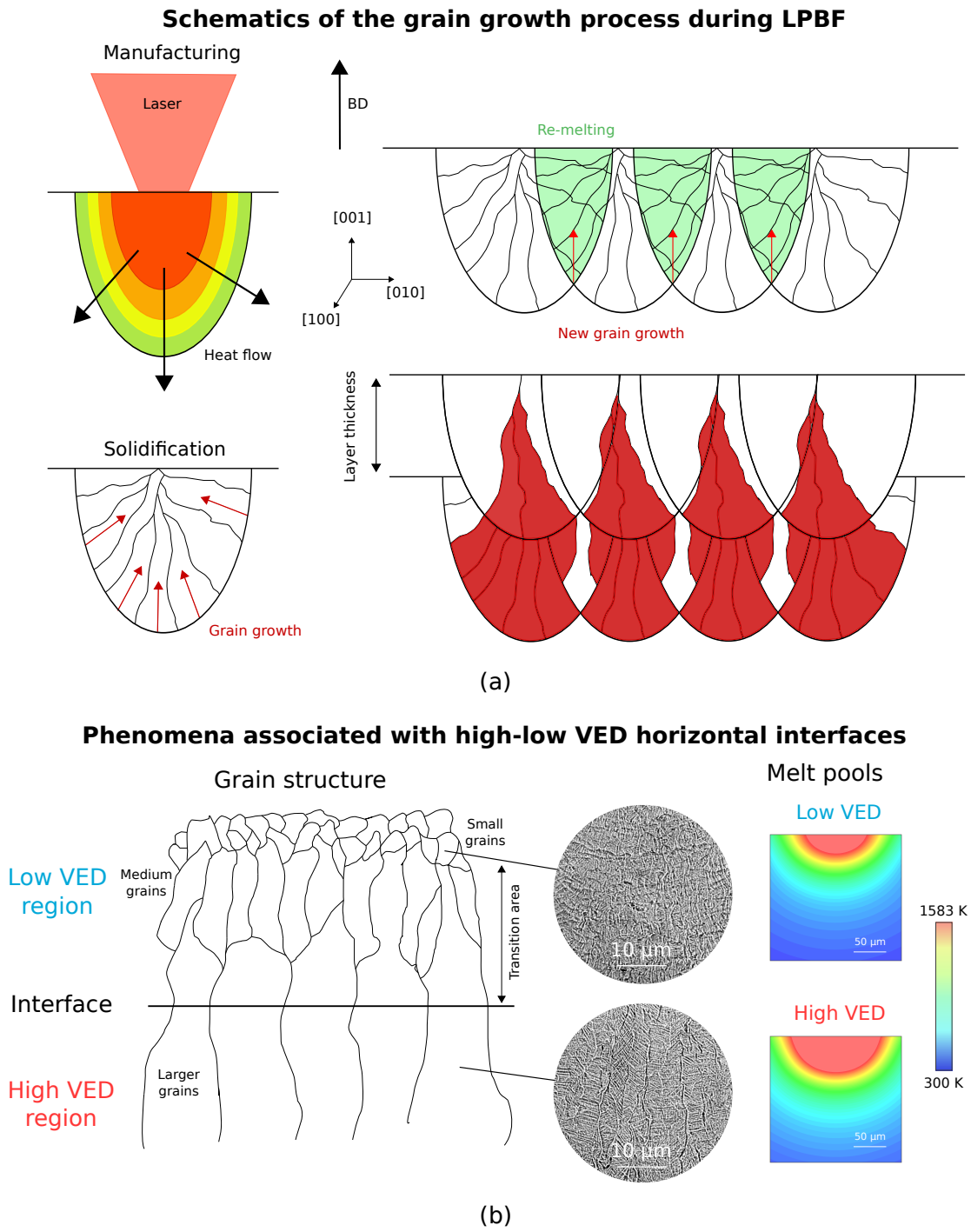


Figure 5.10: Schematic of the development of high texture during LPBF process. (a) Schematics of the austenite grain growth process during the LPBF of NiTi. Texture is create on austenite microstructure by the subsequent laser tracks, which re-melt the [010] grains creating a directional thermal gradient and favoring the epitaxial growth. (b) Schematic representation of the microstructure formed at the horizontal interfaces resulting during the AM process in Pattern 1.

gradients and promotes the growth of austenite grains along the vertical direction, as shown in Figure 5.10b. The use of high VED parameters at the bottom part is also associated with the large significant number of precipitates and internal defects discussed in the previous section. This continues layer by layer until the interface is reached, where then, low VED parameters are used. The use of low VED parameters have been found to produce a microstructure of smaller grain size with less pronounced columnar structure (see Section 5.4.1. However, the transition from the columnar microstructure of high VED to low VED is not instantaneous. At the interface, the manufacturing layers manufactured with low VED are subjected to a thermal footprint and microstructural inertia of the material underneath. This promotes the continuation of growth of previously formed columnar austenite grains extending to a certain part of the low VED region. This effect is comparable to the impact of increasing the substrate temperature in LPBF, which has previously been associated with an increase in average grain size [125]. According to the literature [256, 257], larger grain sizes produce a higher recoverable strain due to the reduced presence of grain boundaries, which otherwise act as barriers to the propagation of martensitic transformation. Furthermore, the larger grains at the interface printed with low VED do not exhibit Ti_2Ni precipitates, as the applied energy is lower, inducing a significantly reduced nickel evaporation.

To understand the effect of the local microstructure in each of the regions, the local recoverable strain of each region in the samples printed with Pattern 1 have been computed in Figure 5.11. In this figure, the results of the recoverable strain of the patterned sample are compared with the local ones of each parameter region. The results of homogenized monoparameter samples are also presented for the sake of comparison (see Chapter 4).

It can be observed that the recoverable strain of the region manufactured using a low VED parameter displays a higher recoverable strain than the monoparameter sample manufactured with the same process parameter, while the recoverable strain of the bottom part (manufactured using high VED parameter) displays a similar recoverable strain than in the monoparameter sample. This is in agreement with the previous microstructural observation, in which the high VED microstructure does not stop at the interface but extends through the low VED region. A low VED with a larger grain size than when printed in a single parameter is associated with the larger recoverable strain of the low VED region in Pattern one samples when compared with the values reported for the same parameter set but in monoparameter samples. Consequently, the overall recoverable strain observed in Pattern 1 is closer to the one obtained for high VED parameters under monoparameter conditions.

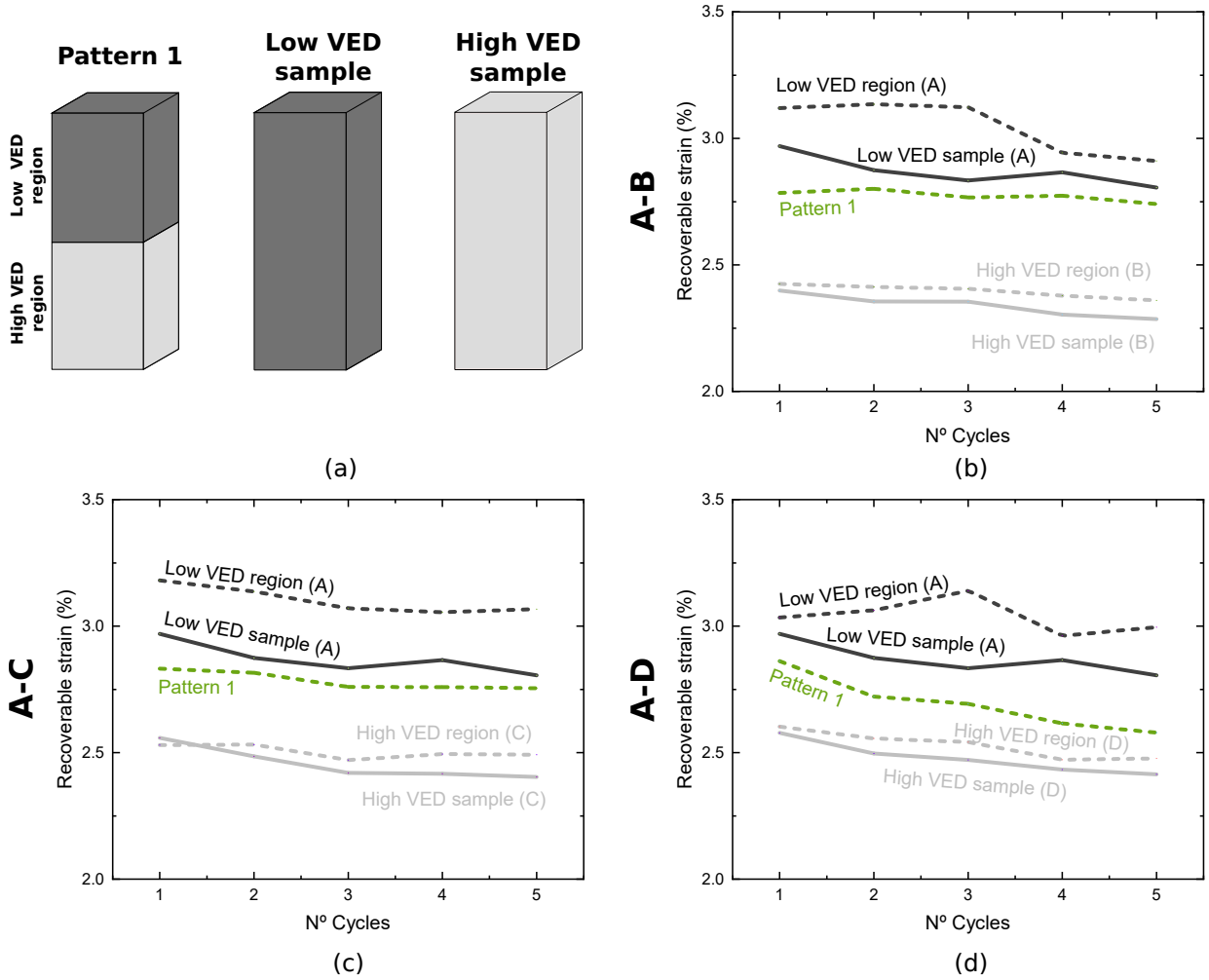


Figure 5.11: Recoverable and plastic strain results of Pattern 1 compared to the monoparameter samples (continuous lines) and the local regions (dotted lines) manufactured using each process parameter in the patterned samples during the training test.

On layer interfaces (Pattern 2 and Pattern 3)

Horizontal interfaces have been discussed in the previous section, now vertical interfaces are addressed. Vertical interfaces present a more complex phenomenon which can induce significant changes in the actuation properties after the LPBF process. As illustrated in Figure 5.1, for the case of different regions present in one layer, at a given interface, the first region is all printed with the same process parameters (low or high VED), and once completed, the printing proceeds with right side of the interface with the complementary process parameter set. The large difference in the VED used to print each region results in greater thermal gradients than for the case of monoparameter samples. These gradients are expected to be especially pronounced in the layer plane, contributing to complex thermal behavior during the LPBF process. To this end, the thermal footprint of the laser at the pattern interfaces is simulated using FEM thermal simulations, as indicated in Figure 5.3b). Once simulated, the molted and solid regions in each track pass were computed to extract the melt pool dimensions. Figure 8.1 presents the results of the melt pool dimensions . These results illustrate the contour of material that have reached temperatures exceeding the liquidus point for NiTi (1583 K). For each case, both the depth and width planes of the melt pool are presented. For the shake of comparison, the reference graphs Cases L and H simulating only the low and high VED laser track, respectively, are shown by dotted black lines indicating the maximum values of the contours.

In the cases L$\perp$H and L$\angle$H , the first half of the laser track is manufactured with the low VED parameter, while in Cases H$\perp$L and H$\angle$L, the first half is fabricated using the high VED parameter. The width of the melt pool track exhibits a symmetric relationship in all four cases, with a larger width observed in the region printed using the high VED parameter and a smaller width in the region printed with the low VED parameter, which has also been observed experimentally by Rangaswamy et al. [249]. The maximum width in the low VED regions corresponds to the maximum width observed in the simulation using only the low VED parameter (case L). The same effect is observed in the high VED region. In terms of the depth, a higher VED results in a higher depth of solid material, while a lower VED leads to a lower depth, which is consistent with the findings reported by Rangaswamy et al. [249]. However, the depths of the melt pools present an asymmetric response depending on the simulated case. A complex phenomenon is observed at the maximum depth of the melt pools in the low VED area (for all cases). The maximum depth varies depending on which set of process parameter is manufactured firstly (the high or low VED parameter). In Cases L$\perp$H and L$\angle$H, where the low VED parameter is applied first, the depth of the solid material during the manufacturing of the first half (low VED region) is identical to that achieved in

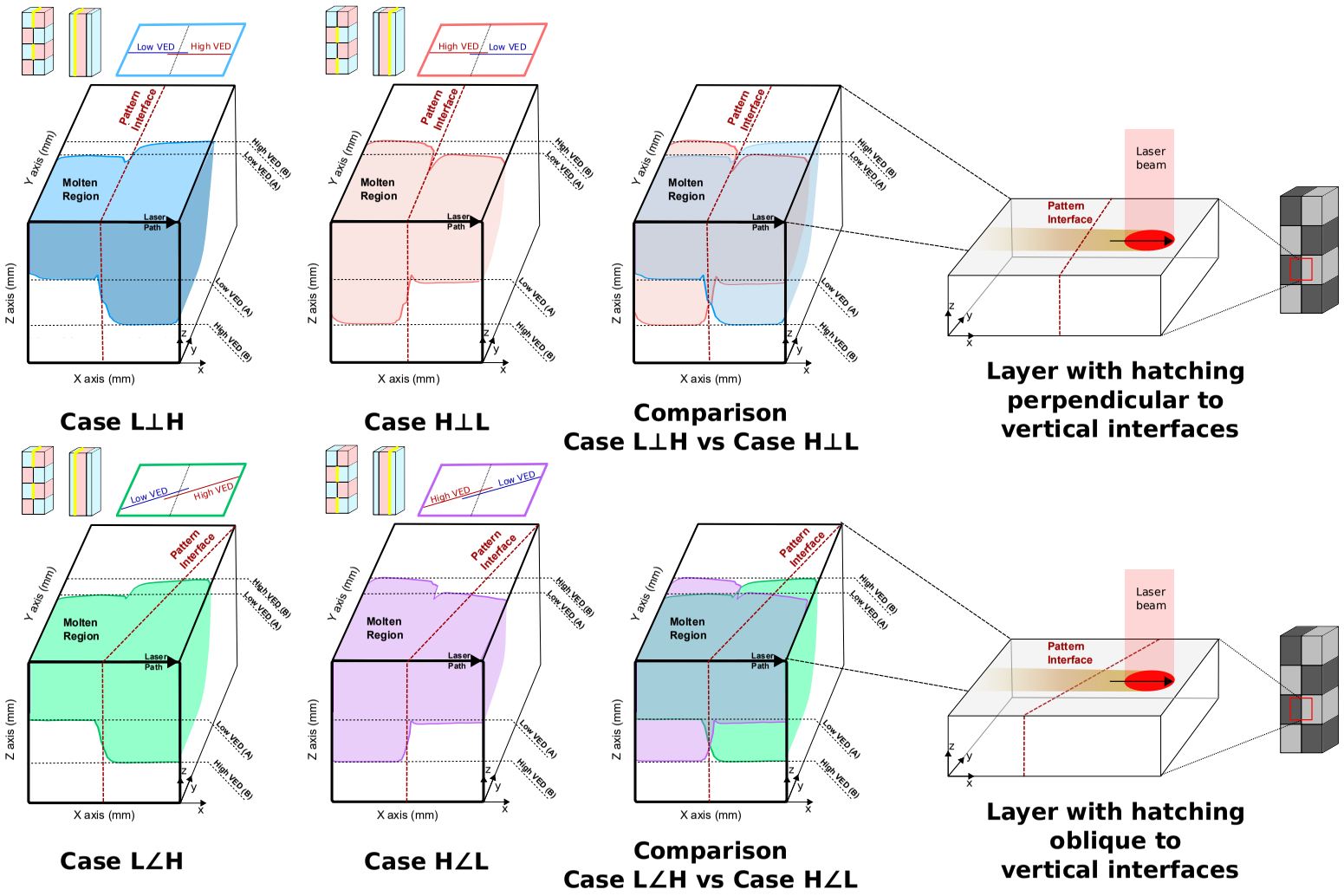


Figure 5.12: Results of the laser track simulations. Cases L and H are presented as dotted lines indicating the maximum values achieved.

Case L ($\sim$ 30 µm), where only the low VED parameter was used. During printing of the high VED parameter, the depth achieved for all 4 cases is similar to that observed in the monoporameter Case H ($\sim$ 55 µm). In contrast, for Cases H$\perp$L and H$\angle$L, where the high VED parameter is applied first, the depth reached in the second part of the path (low VED region) exceeds the result obtained in Case L. This can be attributed to thermal accumulation, the first high VED track preheats the material enabling more energy retention during the second track melting. So, the second track benefits from heat accumulation, leading to deeper penetration even using the low VED parameter. Each powder layer measures 30 µm, so during the manufacturing of the high to low VED tracks (in cases H$\perp$L and H$\angle$L), the grains of the low VED side will be different than during the manufacturing of the regions of low to high VED tracks. So, the sample will have an heterogeneous interface structure depending which region is printed first (if low or high VED). Moreover, based on these computed results, it is found that the effect of achieving an increased solid material depth using a high to low VED track during printing is independent of the laser track length, as observed in Cases H$\perp$L and H$\angle$L. This heterogeneous interface grain structure and the internal stress fields between the low and high VED areas during the phase transformation can play a role in the observed reduction in recoverable strain in Patterns 2 and 3. It is important to note that, in this analysis, only a single laser track was simulated. This effect is likely more pronounced during actual manufacturing due to the heat contribution from adjacent laser tracks.

To study the local melting at the interface by the change in laser parameters, the temperature evolution at the exact interface has been computed for each of the cases, see Figure 5.13. The results in this figure show the temperature along the time of different points located at the midpoint of the complete laser path at different depths for all cases. As observed in Figure 5.13a, Cases L and H illustrate the individual low and high VED laser tracks, respectively. As expected, the application of a higher VED (Case H) results in higher surface temperatures ($\sim$ 2700 K) compared to lower VEDs ($\sim$ 2000 K). Moreover, as demonstrated in the previous results (see Figure 8.1), the high VED shows higher temperatures at the same depths. At a depth of 45 µm the low VED laser track does not reach the melting point of the material, while in the high VED case, it is achieved. In Case L$\perp$H (low to high VED track) during the first track of the laser, the powder melts up to 30 µm. In the second pass, using high VED, half of the second powder layer (45 µm) reaches the solidus temperature but does not reach the liquidus temperature. H$\perp$L (high to low VED track) demonstrates that during the first track, the first powder layer melts completely (30 µm), along with the half of the second layer (45 µm) which reaches the liquidus temperature. During the second track, the first layer does not remelt completely. Therefore, it is clear that different thermal gradients are expected at

the interfaces, depending on the transition order of the parameter set, and differing grain growth can also be expected between different vertical interfaces.

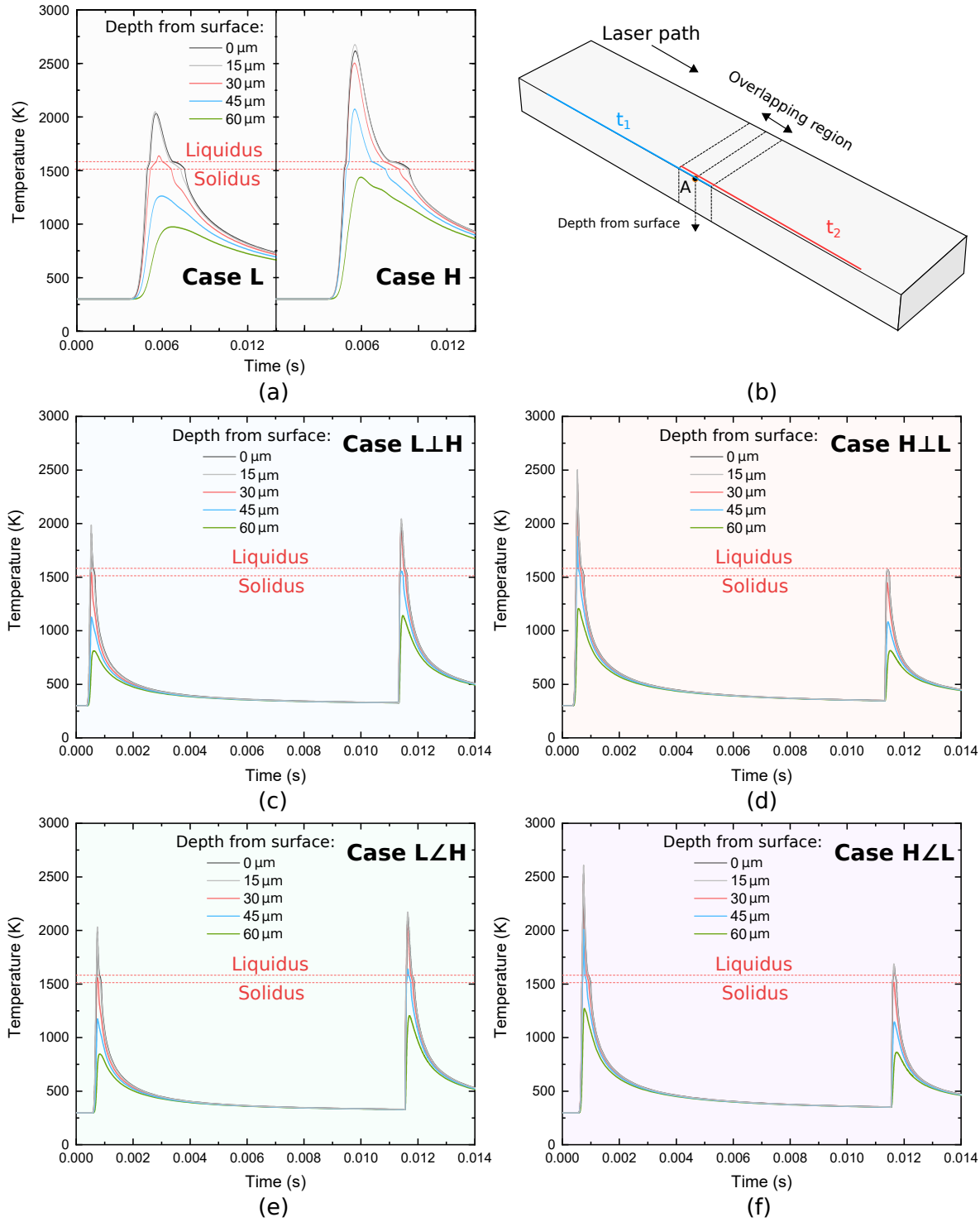


Figure 5.13: Results of the laser track simulations: temperature of points of the interface (Point A) with a depth of: 0, 15, 30, 45 and 60µm from the surface.

It is interesting to note that, in all cases with two laser tracks at the interface, the maximum temperatures reached are lower than the temperatures reached in the single laser track cases (Cases L and H). This is because the laser had an inertia effect in the way of the path, which means that when the laser, during the first half of the track, reaches the midpoint it turns off, losing the material part of the thermal energy during this process. In the second half, when the laser turns on, it incise on a material which has cooled down from the first pass, so the temperature reached in the interface is not as higher as it would be from a continuous pass. Due to heat conduction and the thermal inertia effect of the laser, the longer the overlapping region, the higher these effects. So in Cases L$\angle$H and H$\angle$L where the overlapping region is higher due to the angle between the laser track and the interface, the temperatures reached are higher than in Cases L$\perp$H and H$\perp$L.

As discussed previously, for the case of material printed with homogeneous conditions, crystallographic orientation [001] is the most common after the LPBF process (see Figure 5.10), especially for cases of high VED. However, based on these computational results, the presence of high thermal gradients in the x-axis, can influence on this preferential growth of [001] austenite columnar grains. This can influence the slip deformation observed for the different patterns and its relation to its homogeneous counterparts. The maximum Schmid factor for austenite $\{100\}\langle 110\rangle$ slip systems for the crystallographic orientation of [001] and [011] are 0.0 and 0.5 [107], respectively. So, based on this, the appearance of crystallographic orientations different from [001] during the LPBF process could be responsible for the increase of irrecoverable strains in Pattern 2 after the first thermomechancal cycle. This can be attributed to an increase in austenite yield in regions where the crystallographic texture of the grains [011] is more prevalent than [001]. Pattern 3 can experience similar effects to those in Pattern 2 due to the type of manufacturing. Both have vertical interfaces (see Figure 5.1). However, in this case, the loading direction of the test and the pattern arrangement create a continous medial zone of columnar [001] grains which are not interrupted by horizontal. This central region, which is populated with Ti_2Ni precipitates (see Figure 5.4.1) results in a constrain for the rest of the regions to deform, as the need to deform continuously. This results in a global thermomechanical behavior similar to that achieved in the high VED monoparameter sample, characterized by a lower plastic strain during the first thermomechanical cycle.

In terms of the effect of the vertical intefeaces on the TWSME, it is well established TWSME can be induced in NiTi SMAs through various training procedures [258, 259]. These procedures typically involve repeated deformation and phase transformation between austenite and martensite. In this study, the experimental approach was designed to introduce a directional

internal stress field during training. These stress fields promote the formation of martensite variants with preferred orientations. As shown in Figure 5.8, the recoverable strains for Patterns 2 and 3 are close to the lower limit, comparable to the high monoparameter VED sample, while Pattern 3 falls below this threshold. The stress fields generated at the interfaces during phase transformation in training cycles can hinder the development of new stress fields, thereby preventing the formation of preferential martensite variants and reducing the TWSME. To validate this observation, Figure 5.14 presents the stress fields computed of the elasto-plastic simulations for the different patterned geometries. Further details regarding the simulations are provided in Annex A. These simulations illustrate the start of the martensitic transformation during the training test, where regions with high VED parameters undergo transformation first, leading to elongation. In contrast, regions with low VED parameters do not reach the M_s temperature and therefore remain untransformed. Consequently, distinct stress fields develop across the patterned geometries, particularly at the interfaces, where variations in stress distribution promote the formation of specific martensite variants during training, which cannot be preferentially orientated along the loading direction specifically in Patterns 2 and 3. This phenomenon reduces the overall TWSME observed in all patterned samples when compared to the monoparameter counterparts, as discussed previously.

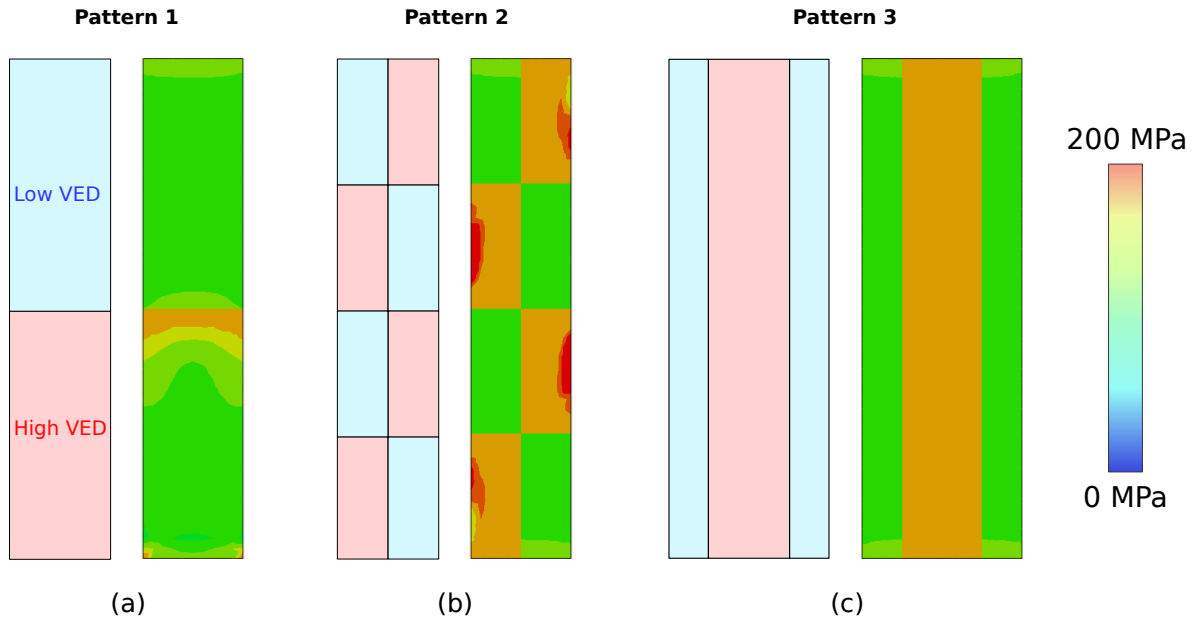


Figure 5.14: Von Mises stress results of the elasto-plastic simulations for (a) Pattern 1, (b) Pattern 2 and (c) Pattern 3.

5.5 Conclusions

In this work, the influence of the design, construction, and testing of graded patterns of nearly equiatomic NiTi metamaterials with different LPBF process parameters have been studied. The results demonstrate the design flexibility of this approach in tailoring thermomechanical properties for specific applications. The main conclusions drawn from this work are:

1. Three different graded pattens have been designed and manufactured combining both high and low VED regions: Pattern 1 with a bottom low VED region and top high VED region, Pattern 2 with a squared chess type distribution of low and high VED regions and Pattern 3 formed vertical slices of high and low VED regions. For each pattern region, a combination of low (A) and high (B,c,D) process parameters have been used resulting in a total of 9 design cases.

2. The microstructural analysis shows that for all patterns, regions printed with high VED, present a columnar grain structure promoted by the large thermal gradients and precipitation of Ti_2Ni promoted by higher nickel evaporation. On the other side, low VED regions present absence of precipitation and more equiaxed grain structure. The transition between large columnar grains to equiaxied grains is not immediate and the high VED structure pass the interface into the low VED region.

3. The TTs in the patterned samples appear to be highly sensitive to the pattern geometry and independent of the specific pair of process parameters used for manufacturing. This sensitivity seems to be associated with the total area of vertical interfaces, which promotes the formation of higher local stress fields.

4. During the training of the SMA, the recoverable strain appears to exhibit a strong correlation with the geometry of the manufactured pattern. Samples produced using pattern 1 display higher recoverable strains, whereas those printed using Patterns 2 and 3 show lower recoverable strains. This behavior has been attributed to the constraint of continuous deformation/transformation along the pattern interfaces, blocking the regions with higher transformation temperatures the transformation of the others. The plastic strains observed in the patterned geometries appear to be correlated with the formation of a larger columnar grain during the LPBF process. Pattern 1 formed larger columnar grains in the high VED region which extends partially also to the low VED region, reducing plastic strain. Pattern 2, due to exposure to complex thermal gradients, produces a more complex grain structure, leading to an increase in plastic strain.

5. The recoverable strain after training (TWSME) resulting for the graded patterned samples is similar to or lower than those of the high monoparameter samples from previous studies. This is attributed to the added difficulty of the formation of preferential martensite variants during the training procedure in these graded samples, caused by the complex stress fields that arise at the interfaces between parameters, confirmed by numerical simulations. Numerical thermal simulations have confirmed the influence of the vertical interfaces on the thermal footprint of the LPBF. The results show the importance of migrating from a low to a high VED region or a high to a low VED region, which present asymmetric results and leading to the heterogeneous interface structure and internal stress field which is related to the lower recoverable strains observed after training.

Chapter 6

Additive manufacturing of graded NiTi SMA cellular structures

6.1 Introduction

Cellular materials are a class of metamaterial that are defined by their internal cellular structure [260]. They are characterized by a network of interconnected cells or pores that form a continuous three-dimensional structure [261]. The versatility of the internal structure design leads to a wide range of properties, including a high strength-to-weight ratio, excellent energy absorption, enhanced thermal insulation, or even acoustic damping. Cellular materials are usually classified according to their internal structure and production methods [262] as shown in Figure 6.1):

- **Foams** are produced by foaming a liquid mixture and are used in applications such as insulation and packaging [263]. The shape of the unit cells in foam structures are randomly generated [264].
- **Honeycombs** are generally made by cutting or stamping sheets and are lightweight with high strength-to-weight ratios, useful in aerospace and automotive structures [265]. Their unit cells have the same sizes and have regular shapes [266].
- **Lattices** are a kind of structure that is formed by the array of spatial unit cells [267]. They can be uniform or non uniform.

This last type of cellular materials (lattice structures) is gaining interest in recent years due to their versatility enabled by AM [268]. These structures can be randomly generated

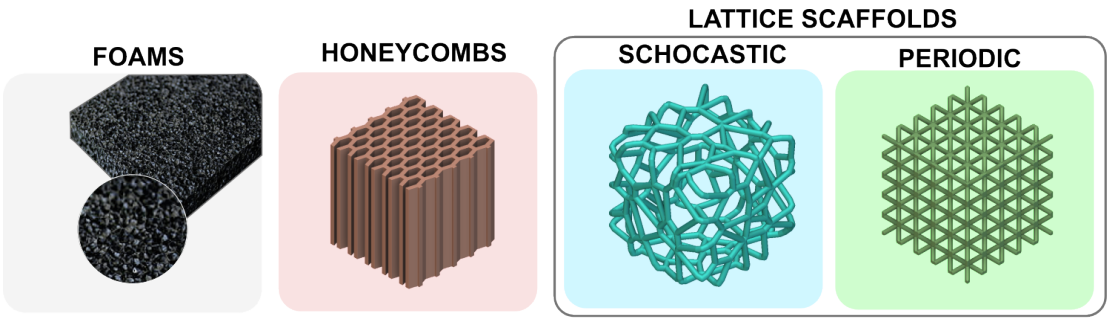


Figure 6.1: Types of cellular materials depending on their internal structure.

(stochastic lattice structures) or by repetition of a unit cell along the three-dimensional space (periodic lattice structures). The use of metal as foundational material for lattice structures have become increasingly popular due to their ability to extend the tight property space of conventional metals and its alloys. This has gained attention in a wide range of fields such as aerospace, automotive, or biomedical engineering [269, 270]. Among the advantages of lattice structures over conventional bulk materials are their unique combination of mechanical properties, including high specific stiffness and strength, low weight, and excellent energy absorption capabilities, offering several advantages over traditional solid structures [271]. Another reason for the increasing popularity of lattice structures is their versatility and ability to be heterogeneously optimized by locally adjusting the size, shape, and orientation of unit cells, all this enabled by the development of new manufacturing routes such as additive manufacturing techniques [272].

The use of SMAs in the manufacturing of more complex geometries like lattice structures has also been target for research [58, 59, 29]. The manufacturing and understanding of the thermomechanical behavior of SMA-lattices is not trivial, and although several studies have successfully printed NiTi structures using complicated shapes [273, 274], the printing of SMA lattices presents some critical challenges [150, 149]. For example, the work of Khademzadeh *et al.* and Biffi *et al.* focused on one of these challenges, trying to understand and reduce the deviation of the printed lattice structure from the designed structure [150, 149]. Other works have focused on understanding and predicting the challenging thermomechanical behavior of lattice structures [23, 29]. Yang *et al.* [148] investigated the effect of the metal volume fraction on the compressive behavior of NiTi giroid structures. Andani *et al.* [29] designed lattice structures using different unit cells, obtaining low-volume fraction structures that maintain good thermomechanical properties.

Based on these studies, it is clear the new horizon of possibilities enabled by AM in the control and modification of the mechanical and actuation properties of SMA. However, these incipient

studies seems to have taken two different unconnected marked paths in the modification of these properties: either local modification of the processing condition to create graded monolithic materials with differences in the local behavior (see Figure 6.2A) or geometrical modification of the printed geometry through latticing strategies to modify the macroscopic behavior of the structure (see Figure 6.2B). To the known of the authors, the combination of these two approaches has not yet been explored and the paths remain disconnected. There is a clear opportunity to explore the synergetic effect of combining both approaches in the local modulation of the processing parameters in the LPBF SMA lattice structures (see Figure 6.2A+B).

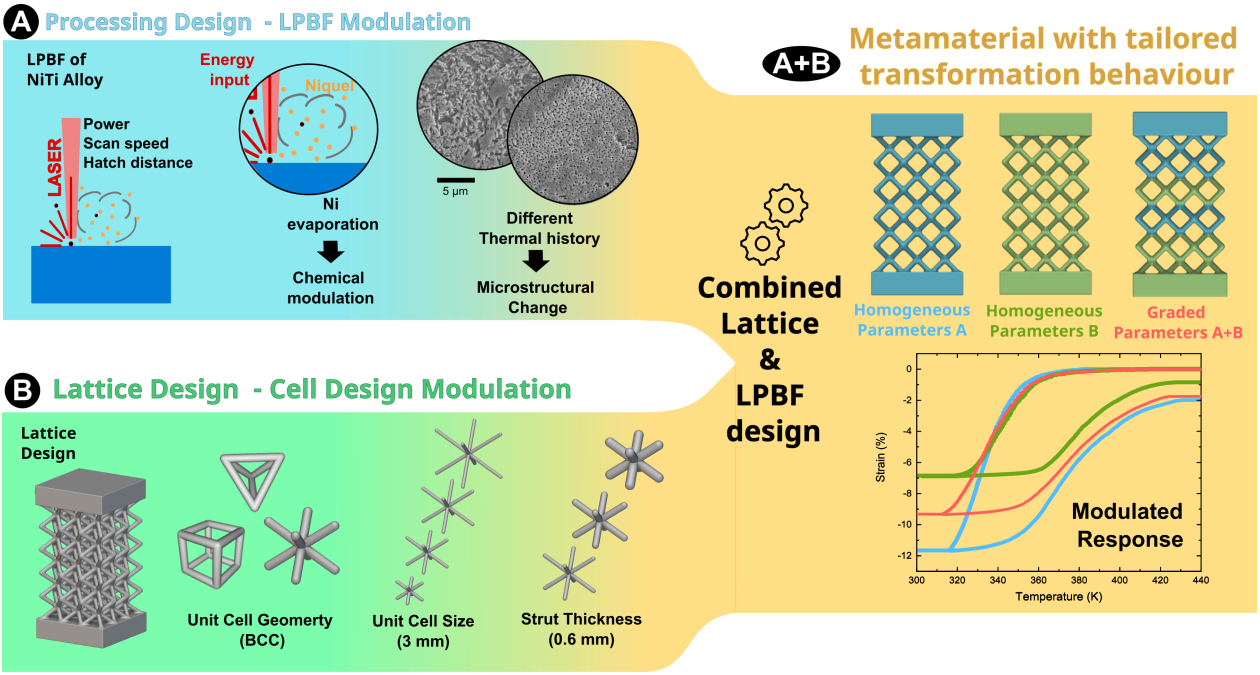


Figure 6.2: Overview of the combined geometrical (A) and processing (B) design framework (A+B) leading to cellular structures with tailored thermomechanical behaviour.

This paper aims at exploring this opportunity and providing novel results to pave the way for a new generation of intelligent structural designs with diverse application potential. To this end, in this study, lattice structures formed by BCC unit cells have been designed with both graded and homogeneous processing conditions by developing and ad-hoc processing code. These samples have been manufactured on a Ni lean NiTi alloy and mechanically tested for the evaluation of their superelastic and thermomechanical properties. Finally, the connection between processing and thermomechanical behavior has been rationalised by a combination of microstructural characterization, computational modeling and geometrical assessment.